Quasi-BIC Resonance Modes in Metasurface: Excitation and Applications at Near-Infrared and Terahertz Frequencies

by

Bhairov Kumar Bhowmik

A thesis submitted
in Partial Fulfillment of the Requirements
for the Degree of

DOCTOR OF PHILOSOPHY.

Department of Physics
Indian Institute of Technology Guwahati
Guwahati 781039, India.

October 2024

Quasi-BIC Resonance Modes in Metasurface : Excitation and Applications at Near-Infrared and Terahertz Frequencies

by

Bhairov Kumar Bhowmik

Roll No. 196121102

A thesis submitted
in Partial Fulfillment of the Requirements
for the Degree of

DOCTOR OF PHILOSOPHY.

Supervisor
Prof. Gagan Kumar

Department of Physics
Indian Institute of Technology Guwahati
Guwahati 781039, India.

October 2024

DECLARATION

The work in this thesis entitled "*Quasi-BIC Resonance Modes in Metasurface: Excitation and Applications at Near-Infrared and Terahertz Frequencies*" has been carried out by me under the supervision of Prof. Gagan Kumar, Department of Physics, Indian Institute of Technology Guwahati. No part of this thesis has been submitted elsewhere for the award of any other degree or qualification. The research works have been carried out in the period from January 2020 to October 2024.

In keeping with the general practice of reporting scientific observations, due acknowledgments have been made wherever the work described is based on the findings of other investigations.

Bhairov Kumar Bhowmik

Bhairov Kumar Bhowmik,
Roll no. 196121102,
Department of Physics, IIT Guwahati,
Guwahati-781039, Assam, India.
DATE: .....

CERTIFICATE

It is certified that the work contained in the thesis entitled "*Quasi-BIC Resonance Modes in Metasurface: Excitation and Applications at Near-Infrared and Terahertz Frequencies*" by Mr. Bhairov Kumar Bhowmik, a student of the Department of Physics, IIT Guwahati was carried out under my supervision and has not been submitted elsewhere for award of any degree.

Prof. Gagan Kumar,
Department of Physics, IIT Guwahati,
Guwahati-781039, Assam, India.
DATE: .....

To my parents

To my well wishers

ACKNOWLEDGMENTS

First and foremost, I would like to express my deepest gratitude to my Ph.D. advisor, Prof. Gagan Kumar, for his unwavering support, guidance, patience, and motivation throughout my Ph.D. journey. It has been a privilege to work under his mentorship, and his encouragement continually pushed me to overcome the limitations I faced during my research. I am grateful for this period in my life, and there are countless lessons I have learned from him that will continue to inspire me.

I would also like to extend my sincere thanks to my doctoral committee, Prof. Ashwini Kumar Sharma, Dr. Uday Narayan Maity, and Dr. Rishikesh Dilip Kulkarni, for their encouragement, insightful comments, and direction, which greatly enhanced my skills and deepened the understanding of my work. I am also grateful to Dr. Debabrata Sikdar from the Department of Electronics and Electrical Engineering, IIT Guwahati, for his valuable guidance and motivation during the first three years of my Ph.D.

I extend my heartfelt thanks to the current Head of the Department, Prof. Bosanta Ranjan Boruah, as well as the former Heads, Prof. Subhradip Ghosh and Prof. Perumal Alagarsamy, along with all the faculty members and staff of the Department of Physics, for providing me with the necessary facilities and support throughout my research work.

I am deeply appreciative of the support and constructive suggestions provided by my senior lab members, Dr. S. Jagan Mohan Rao, Dr. Rakesh Sarkar, Dr. Dhriti Maurya, and Dr. Angana Bhattacharya, during the initial days of my Ph.D. I am especially grateful to Dr. Tanmay Bhowmik for his constant support and friendly guidance throughout my journey.

I would like to express my thanks and gratitude to my friend and colleague Mr. Bhagwat Singh Chouhan, with whom I have spent significant time in the terahertz meta photonics lab. I have learned much from him, and together, we successfully tackled many complex tasks for the lab. I am also thankful to my colleagues, Mr. Chandan Kumar, Mr. Anshul Bhardwaj, Mr. Rohith K.M., Mr. Lavi Kumar Vaswani, Asit Das, Abhijit Dash,

and Harshita, for their support, insightful discussions, and for fostering a friendly and collaborative atmosphere in the lab. It has been a privilege to work closely with Rohith and Lavi in such a productive environment.

I would also like to extend my gratitude to the current and former Heads, faculty members, and staff of the Centre for Nanotechnology, IIT Guwahati, for their support and cooperation. I am thankful to Dr. Kanishka Murmu and Mr. Sunil Gone for providing essential training in electron beam lithography.

I thank to my Ph.D. group-mates for their valuable discussions and for fostering a friendly, collaborative atmosphere throughout this journey. I would also like to extend my heartfelt thanks to the hostel and mess service personnel for their dedicated support and services, which made my stay comfortable and allowed me to focus on my research.

I am especially grateful to my parents, my elder brother, who always encouraged me to pursue my Ph.D. from IIT, and my sister-in-law (Boudi) for their unwavering love, support, and sacrifices throughout this journey. Their encouragement has been a crucial part of my success. Lastly, I want to express my sincere thanks to Nitu for her constant support, encouragement, love and constructive feedback. And a huge thank you to all my friends, well-wishers, relatives, and many more.

.

Abstract

Bound State in the Continuum (BIC) are states that lie in the continuum but remain perfectly localized. Ideal BICs are a mathematical concept with an infinite quality factor (Q factor), which can not be observed in a real scenario. The transformation of BIC into a quasi-BIC mode manifests as a Fano resonance with a finite high Q factor and can be observed experimentally. The excitation of high Q resonance modes is critical for developing advanced photonic devices such as sensors, filters, and nonlinear optical components. Quasi-BIC modes can be excited in numerous ways according to the types of BIC: by continuously tuning system parameters (accidental BIC) or systematically introducing asymmetry in the structure (symmetry-protected BIC). The symmetry-protected BIC mechanism has garnered significant attention due to its simple physical interpretation and precise control over the Q factor of resonance. This thesis primarily focuses on the excitation of symmetry-protected quasi-BIC modes in metasurfaces for terahertz (THz) and near-infrared (NIR) frequencies. In the NIR, specifically within the C-band region (1535 nm to 1565 nm), we explored the application of an ultra-narrowband pass filter. Using the same symmetry-breaking approach, we demonstrated a dual-parametric (temperature and refractive index) sensor with a high Figure of Merit. In both studies, multipolar decomposition theory was employed to analyze the nature of the excited modes. To achieve the ultra-narrow full width at half maximum in filter application and high sensitivity in the sensing applications for the NIR frequency region, we used an all-dielectric metasurface-based design due to its negligible ohmic losses.

Besides these two studies, this thesis also discusses the exploration of quasi-BIC mode in the terahertz region using metallic metasurfaces. In this context, we investigated a selective symmetry-breaking approach in a THz metallic metasurface. This novel method involves strategic symmetry-breaking of a ring-shaped metamolecule system to reduce radiation density, thereby achieving a high Q quasi-BIC resonance. The Q factor and

resonance frequency can be tuned by altering the geometrical degree of asymmetry. Our experimental and theoretical results validate the effectiveness of this approach, demonstrating higher Q factors compared to conventional methods. Next, we explore lattice constant perturbation as an alternative method to excite high Q quasi-BIC modes. Instead of the conventional in-plane symmetry breaking, perturbing the lattice constant causes band folding in the first Brillouin zone, resulting in stable resonance frequencies with tunable quality factors. This method offers greater material flexibility and improved device performance.

In summary, we present a comprehensive study of quasi-BIC resonance modes in metasurfaces and demonstrates its application as filter and sensors in near infrared. Additionally, the thesis also explores innovative approaches for achieving high Q factors in terahertz metasurfaces. The findings pave the way for the development of compact, high-performance photonic devices with applications in filtering, sensing, and nonlinear optics.

List of Publications and Conferences Attended

Journal Publications

1. **Bhairov Kumar Bhowmik**, Tanmay Bhowmik, Pranav Kumar Pandey, Makaraju Srinivasa Raju, Debabrata Sikdar, and Gagan Kumar, "All-dielectric metasurface based ultranarrow bandpass filter in optical C-band," *J. Opt. Soc. Am. B*, vol. 40, pp. 1311–1318, 2023.

2. **Bhairov Kumar Bhowmik**, Tanmay Bhowmik, Pranav Kumar Pandey, Makaraju Srinivasa Raju, Debabrata Sikdar, Gagan Kumar, "All-dielectric asymmetric planar metasurface based dual-parametric sensor," *Optics Communications*, vol. 550, p. 129880, 2024.

3. **Bhairov Kumar Bhowmik**, K M Rohith, Samuel John, Shriganesh Prabhu, and Gagan Kumar, "High-quality factor Quasi-BIC mode via selective symmetry-breaking approach in a terahertz metasurface," *New Journal of Physics*, vol. 26, no. 6, p. 063024, 2024.

4. **Bhairov Kumar Bhowmik**, K M Rohith, and Gagan Kumar, "Excitation of High-Quality Quasi-BIC toroidal Mode in a Lattice perturbed terahertz Metasurface." (accepted)Applied Physics Letter, 2024.DOI:10.1063/5.0228324

Co-author contribution

1. Angana Bhattacharya, Bhagwat Singh Chouhan, Rajan Singh, **Bhairov K Bhowmik**, Gagan Kumar, "Polarization independent lattice-coupled terahertz toroidal excitation," *Journal of Physics D: Applied Physics*, vol. 56, no. 415101, 2023.

2. Tanmay Bhowmik, **Bhairov Kr Bhowmik**, Pranav Kr Pandey, Gagan Kumar, Debabrata Sikdar, “Dual-band electro-optic modulator based on tunable broadband metamaterial absorber,” *Optics & Laser Technology*, vol. 161, p. 109129, 2023.

3. Maidul Islam, **Bhairov Kumar Bhowmik**, KM Dhriti, Devendra Mohan, Amir Ahmad, Gagan Kumar, “Thin film sensing in a planar terahertz meta-waveguide,” *Journal of Optics*, vol. 24, no. 064016, 2022.

4. Maidul Islam, Anshul Bhardwaj, **Bhairov Kumar Bhowmik**, Gagan Kumar, “Terahertz Meta-waveguide Based upon Strongly Near-Field Coupled Split-Ring Resonators,” *Journal of Infrared, Millimeter, and Terahertz Waves*, vol. 44, pp. 740–751, 2023.

5. Angana Bhattacharya, Rakesh Sarkar, Naval K Sharma, **Bhairov K Bhowmik**, Amir Ahmad, Gagan Kumar, “Multiband transparency effect induced by toroidal excitation in a strongly coupled planar terahertz metamaterial,” *Scientific Reports*, vol. 11, no. 19186, 2021.

Conference/Workshop Participation

- **“Frontiers in Terahertz Technology and Applications (FTTA-2021)”**. Presented a poster on “Exploring sensing capabilities in terahertz meta-waveguide-based approach.”(In-person) **Best Poster Award**

- Poster presentation at the **2023 ICTP Winter College on Optics: Terahertz Optics and Photonics. (Best poster award 2nd position)**

- **2022 Workshop on Recent Advances in Photonics (WRAP)**: Online poster presentation, "Dual-Band Electromagnetic Induced Transparency in a Terahertz Metawaveguide Design."

- **Research and Industrial Conclave**2022, organized by IIT Guwahati: Online oral presentation.

- **FiO LS (2022)**: Online poster presentation: "Polarization-insensitive refractive index sensor based on high-Q resonance in all-dielectric metasurface".

- **Photonics 2023**: (In-person) Poster presentation, "Design and Simulation of a Narrow Band-Pass Filter Using a Planar Dielectric Metasurface."
- **ICANN 2024**: In-person poster presentation.

Conference Publications

- B. K. Bhowmik, T. Bhowmik, P. K. Pandey, D. Sikdar, and G. Kumar, "Polarization-insensitive refractive index sensor based on high-Q resonance in all-dielectric metasurface," in *Frontiers in Optics + Laser Science 2022 (FIO, LS)*, Technical Digest Series (Optica Publishing Group, 2022), paper JTu5B.68.
- B. K. Bhowmik, M. Islam and G. Kumar, "Dual-Band Electromagnetic Induced Transparency in a Terahertz Metawaveguide Design," in *2022 Workshop on Recent Advances in Photonics (WRAP)*, Mumbai, India, 2022, pp. 1-2, doi: 10.1109/WRAP54064.2022.9758258.
- 2023 IEEE Guwahati Subsection Conference (GCON): (Oral presentation) "High-Q resonating all-dielectric metamaterial for refractive index sensing,"
- B. K. Bhowmik, T. Bhowmik, P. K. Pandey, M. S. Raju, D. Sikdar and G. Kumar, "High-Q resonating all-dielectric metamaterial for refractive index sensing," in *2023 IEEE Guwahati Subsection Conference (GCON)*, Guwahati, India, 2023, pp. 1-2, doi: 10.1109/GCON58516.2023.10183548.
- T. Bhowmik, B. K. Bhowmik, P. K. Pandey, G. Kumar, and D. Sikdar, "Epsilon-Near-Zero Material based Dual-Polarization On-Chip Electro-Optic Modulator," in *Frontiers in Optics + Laser Science 2023 (FiO, LS)*, Technical Digest Series (Optica Publishing Group, 2023), paper JM7A.66.

List of Figures

- Figure 1.8(a) The fabricated negative refractive index metamaterial. The metamaterial structure is made up of a combination of a split-ring resonator and wire lithographically deposited on the opposite side of a circuit board. The thickness of the structure is 1 cm. (b) Experimental demonstration of the negative refractive index phenomena according to Snell's law. The plot shows detected power as a function of angle from the normal. (c) A schematic representation of the geometry that is used to demonstrate negative index of refraction.
- Figure 1.9 Position of the terahertz region in the electromagnetic spectrum.
- Figure 1.10(a) A closed ring resonator metamaterial unit cell with radius 30 μm, width 6 μm and periodicity 90 μm on the top of a quartz substrate. (b) Simulated transmission spectrum for the closed ring resonator. (c) A circular Split Ring Resonator, with split gap of 6 μm, while all other geometrical parameters are same as the closed ring resonator. (d) The simulated transmission plot for two orthogonal polarizations of incident electromagnetic wave.
- Figure 1.11 The Z component of the electric field distributions and surface current distributions for (a,d) the closed ring resonator at frequency f_A, (b,e) the circular split ring resonator LC resonance mode at frequency f_B, (c,f) the circular split ring resonator second resonance mode at frequency f_C, (g,h) the circular split ring resonator at frequency f_D with the electric field polarized perpendicular to the gap.
- Figure 1.12 Effect of symmetry breaking in the additive Q factor of quasi BIC mode; (a) Q factor dependence on in-plane asymmetry parameter defined by the meta-atom as shown in (b). The change in the Q factor follows an inverse square law of the asymmetry. (b) Different types of asymmetry meta-atom and the definition of asymmetry, α.
- Figure 1.13(a) Schematic model of the symmetric Si nanodisk and two asymmetric Si nanodisks after removing (top) or adding (bottom) a part of the disk from the left edge. The SiO_2 substrate is omitted for simplicity. (b) Evolution of the quasi-BIC mode in the transmission spectra with the asymmetry ΔR.
- Figure 1.14 Exciation of quasi BIC mode as Fano and EIT lineshape by introducing structural asymmetry. (a) A mirror symmetry broken Split Ring Resonator, where asymmetry is introduced by displacing the gap from the center with a distance

"d." A dimensionless parameter "a" is defined to express the asymmetry degree quantitatively $a = \left(\frac{l_1 - l_2}{l_1 + l_2}\right) \times 100\%$, where l_1 and l_2 indicate the total length of the left and right branches of the resonator, respectively. (b) The evolution of the Fano and EIT-like quasi-BIC mode in the transmission spectra at different asymmetry degrees for y- and x-polarizations. (c) Analysis of resonance mechanism by electric dipole moments at y- and x-polarizations. The induced geometrical perturbation causes the leakage of the ideal BIC mode.

- Figure 1.15 A visual representation of the Fano formula, depicting the mixing of a discrete (Lorentzian) state and flat continuum, which results in a Fano line shape.
- Figure 1.16 A pictorial representation of charge and current distributions creating (a) electric dipole, (b) magnetic dipole, (c), (d) polar and axial toroidal dipole moments.
- Figure 1.17 An all dielectric metasurface design optimized for the excitation of toroidal resonance. (a) Top: a visual representation of solenoid electric fields (red arrows) inducing a toroidal magnetic field (blue arrow) in a torus. Bottom: A cuboid resonator and the excitation of toroidal resonance due to head to tail magnetic dipole arrangement. (b) the metasurface array and the constituent "meta atom". (c) SEM images of the fabricated sample.
- Figure 1.18(a) Visual representation of the toroidal excitation in the metasurface geometry, (b) Experimental and simulated transmission for different split gap position "d". (c) the surface current plot and H_z plot at different sharp resonance frequencies corresponding to different split gap positions.
- Figure 1.19(a) Conceptual diagram of BZF-BICs. After introducing periodic perturbation, the unit cell periodicity doubles, and guided modes (GM) are transformed into BZF-BICs. Unlike ordinary BICs, the Q factor of BZF-BICs remains robust against disorder. (b) Schematic of terahertz photonic crystal (THz-PhC) slabs: **i)** unperturbed, **ii)** with gap perturbation where the distance between adjacent air holes changes by ΔL, and **iii)** with radius perturbation where the radius of air holes changes by Δr, both these perturbation leads to doubling of periodicity in the x-direction. (c) Calculated transverse electric (TE) band structures of unperturbed and gap-perturbed PhCs ($\alpha = 0.0167$, $\Delta L = 1$ μm), showing band folding at the Γ point. The original first Brillouin zone (FBZ) reduces by half.

spectrum for the design with asymmetry due to the addition of the notch, for two orthogonal polarizations of the incident electromagnetic wave.

- Figure 3.2 (a) The reflectance (R) and transmittance (T) for the resonator with a single square hole without any notch. Inset: The design. (b) Fitted data for the design with asymmetry using the Fano model, and the normalized field profiles (E_y component) show an anti-phase mode below and above the resonance wavelength. (c) Simulated phase spectra showing a change in phase at the resonance. (d) Simulated normalized electric field profile at the resonance wavelength of 1549.8 nm in the x-y plane.

- Figure 3.3 (a) Contour plot showing the dependence of FWHM and resonance wavelength on the degree of asymmetry. (b) Dependence of the Q factor with the asymmetry parameter of the design. Here, the solid line is a result of fit showing an inverse square variation with the asymmetry parameter, and C(=275.9) is a correction factor. (c) Evolution of the resonance mode with respect to the asymmetry parameter.

- Figure 3.4 Multipolar analysis of the proposed metasurface design. $C_p^{\text{sca}}, C_m^{\text{sca}}, C_{Q^e}^{\text{sca}}, C_{Q^m}^{\text{sca}}, C_{\text{sca}}^{\text{total}}$ represent the scattering cross-sections for the resonator due to the electric dipole, magnetic dipole, electric quadrupole, magnetic quadrupole, and the total cross-section, respectively.

- Figure 3.5 Displacement of the notch along the x-direction from its original position is denoted by the parameter D. (a), (c), and (e) show the simulated reflectance spectrum for $D = 0$ nm, $D = 30$ nm, and $D = 60$ nm, respectively. (b), (d), and (f) show the calculated normalized E_y component of electric field distributions for $D = 0$ nm, $D = 30$ nm, and $D = 60$ nm, respectively. The field profiles are calculated in the x-y plane.

- Figure 3.6 Simulation-based parametric analysis of the proposed design with the contour color plot for varying: (a) the periodicity of the unit cell and (b) the thickness of the GaAs layer. The white dashed line shows the optimized value of the parameter for a resonance at the 1549.8 nm wavelength.

- Figure 4.1 (a) The proposed metasurface design under the excitation of a normally incident TE-polarized electromagnetic wave. (b) The top view of the metasurface

"unit cell" with periodicity $P_x = P_y = 746$ nm, length of the GaAs square block $l = 680$ nm, size of the outer cut $a_1 = 120$ nm, $a_2 = 75$ nm, and thickness of the GaAs block $h = 315$ nm.

- Figure 4.2 (a) The simulated reflectance and transmittance of the design without disturbing the symmetry, (b) the calculated transmittance spectrum after introducing an asymmetry for two orthogonal polarization states of the incident wave.

- Figure 4.3 (a) The transmittance spectrum of the metasurface design showing resonance at a wavelength of 1555.8 nm. The blue dashed curve denotes the fitted curve using the Fano formula. (b) The plot of $|C_1|$ (continuous state) and $|C_2|$ (discrete state). (c) Calculated phase difference $\Delta = \arg(C_2) - \arg(C_1)$ between the continuum and the discrete state. (d) The normalized y-component of the electric field at wavelengths 1555 nm (slightly below the resonance wavelength) and 1556.6 nm (above the resonance wavelength).

- Figure 4.5 (a) Dependence of the Q factor on the degree of asymmetry. The blue line shows an inverse square fitting with the degree of asymmetry (δ), with $R^2 = 0.99006$.(b) The contour plot shows a comprehensive view of the resonance wavelength shift as well as the variation of the full width at half maximum (FWHM) of the resonance mode with the degree of asymmetry.

- Figure 4.6 (a) The transmittance spectrum for the different background media, where n_m, n_w, n_b, n_e, and n_a represent the refractive indices of methanol, water, blood plasma, ethanol, and diluted alcohol, respectively. (b) Linearly fitted plot of the refractive index versus resonance wavelength. The R^2 value of 0.9996 indicates good linearity between the wavelength shift and the change in refractive index.

- Figure 4.7 (a) The transmittance spectrum of the metasurface design at different temperatures, (b) the linearly fitted plot of the temperature versus resonance wavelength, the slope of the graph gives the temperature sensitivity of the design.

- Figure 5.1 (a) Schematic of a metasurface design under the excitation of TE-polarized THz radiation. The inset shows the proposed meta-molecule unit cell, where the periodicity $P = 200\,\mu$m, width $w = 6\,\mu$m, radii $r_1 = 41\,\mu$m, $r_2 = 27\,\mu$m, $r_3 = r_4 = 34\,\mu$m, and the thickness of the ring structures $h = 200$ nm. (b) The

photograph and micrograph image of the fabricated metasurface sample using photolithography.

- Figure 5.2 (a) The arrangement of four ring resonators in a metamolecule unit cell with three approaches: symmetric, uniform symmetry breaking, and selective symmetry breaking. The olive background resonators have a radius of 27 μm, the red background resonators have a radius of 41 μm, and the gray background resonators have a radius of 34 μm. (b) Simulated transmission spectrum of the symmetric meta-molecule system, non-uniformly symmetry-broken structure, and uniformly symmetry-broken structure.

- Figure 5.3 The mode hybridization scheme for a micro ring pair unit cell, where the dark mode manifests as a result of dipole detuning due to the introduction of the structural asymmetry.

- Figure 5.4 The simulated Z-component of the electric field, normalized surface current density profile, and absolute of the normalized electric field profile distributions at the three-resonance dip. The color of the frame is consistent with the font color used to depict the three-resonance dip in figure 5.2.

- Figure 5.5 (a) A schematic description of the decomposition of the sharp resonance mode into an unperturbed dark mode and the radiation continuum. The size of the sign represents the strength of the field. (b) The 1D field plot along the Y-direction at $x = -44\,\mu$m and $X = 44\,\mu$m for the symmetry-perturbed metamolecule system. (c) The 1D field plot along the Y-direction for the symmetric structure, calculated using eigenmode analysis.

- Figure 5.6 (a) The theoretically calculated transmission spectrum for a structural asymmetry $\delta = 26.4\%$. The theoretical matching validates the evidence of the bright-dark coupling mechanism. (b) The broad radiation continuum extracted using the analytical model. (c) The corresponding dark or discrete line shape extracted using the analytical fit.

- Figure 5.7 (a) The simulated transmission contour plot as a function of frequency and degree of asymmetry. (b) The asymmetry versus calculated Q factor of the sharp resonance dip. The solid line represents the fitting with the expression

$Q = A\delta^{-2}$ + Correction term. (c) Evolution of the quasi-BIC in the transmission spectra versus the degree of asymmetry.

- Figure 5.8 The fiber-coupled THz time-domain setup focuses the transmitted THz radiation to a beam spot size of 8 mm using a parabolic mirror with a focal length of 10 cm. The focused THz beam is passed through a metasurface sample area of 1 cm × 1 cm and is then detected by the detector.

- Figure 5.9 Micrograph image and experimentally measured transmission spectrum for (a) symmetric structures, (b) with structural asymmetry $\delta = 20.5\%$, (c) with structural asymmetry $\delta = 29.4\%$, fabricated using photolithography.

- Figure 5.10 The measured near-field scanning microscopy image and simulated $|E_z|$ field distributions of the metasurface with asymmetry $\alpha = 29.4\%$ at frequencies (a) $f = 0.71$ THz and (b) $f = 0.92$ THz. The field distributions are scanned and calculated at 10 μm above the metasurface. The ring resonators are highlighted with black dashed circles.

- Figure 6.1 (a) Schematic representation of the optimized planar terahertz double split ring resonator metasurface design on the quartz substrate. Here, the geometrical parameters are, periodicity $\Lambda_x = 200\mu m$, $\Lambda_y = 100\mu m$, length of the square SRR, $l = 65\mu m$, split gap, $g = 16\mu m$ and S represents the perturbed interspacing between two SRR. (b) The fabricated metasurface sample using photolithography in clean room ambiance.

- Figure 6.2 Simulated transmission spectra for the (a) unperturbed case, the separation between the two adjacent SRR is $S = 38\mu m$, (b) perturbed case, when the interspacing between the two adjacent SRR is changed by $\Delta S = 10\mu m$. The change in separation leads to periodicity doubling, as shown in the inset. The unit cell is shown as a dashed marking for a clear view.

- Figure 6.3 The simulated (a) near-field distributions of the Z component of the magnetic field (the field monitor is exactly top of the resonator), (b) the magnetic field arrow plot in the XZ plane, and (c) surface current profile at the sharp Fano resonance dip of frequency 0.71 THz. (d) Simulated E_Z field distributions at the broad resonance dip of $f = 1.11THz$, the plus and minus signs show the corresponding charge distributions.

- Figure A.6 (a) The dispersion plot for the unperturbed case, when the unit cell consists of a single unit cell, the dotted line shows the position of the new X point that would be as a result of folding, (b) the folded modes under the effect of lattice constant perturbation, the folded modes are shown with dotted lines. The circular mark indicates the mode that becomes a BIC mode under the perturbation effect. (c) The Z component of the folded BIC mode calculated using the eigenmode solver.
- Figure A.7 (a) The simulated surface current profile at the sharp quasi-BIC resonance mode, (b) a pictorial representation of the formation of the toroidal moment because of the head-to-tail magnetic moment.

TABLE OF CONTENTS

CHAPTER 1

INTRODUCTION

"Metamaterials are a testament to human ingenuity, allowing us to mold electromagnetic fields and unlock phenomena once thought impossible."

- Sir John Pendry.

1.1 Bound State in Continuum

1.1.1 Historical overview and theoretical foundation

Bound State in the Continuum(BIC) sets a remarkable example of general phenomena discovered in the context of quantum mechanics, which gets an extension to acoustics, hydrodynamics, and photonics [1]. Figure 1.1 depicts the conceptual origin of BICs in the context of quantum mechanics. In a standard quantum well, the spectrum comprises two types of modes: delocalized or extended states that exist within the continuum and bound states that form a discrete set of modes at different energy levels. In 1929, Von Neuman and Wigner showed that by modulating the potential of the quantum well with unbound oscillations, as shown in Figure 1.1, there are solutions of bound modes that exist in the range of continuous spectrum [2].

Initially, in quantum mechanics, BIC is described as a paradoxical state where energy remains trapped despite being embedded in the continuum. These kinds of exceptional bound states have been studied as "*trapped modes*" in acoustics and hydrodynamics

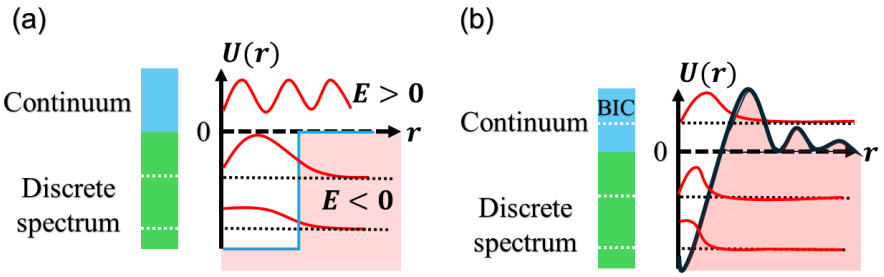

Figure 1.1: (a) The spherical potential well, the states are continuous with $E \geq 0$, and states are discrete or bound states for energy $E \leq 0$, (b) modulation in the potential results in specific solutions: bound state in the continuum.

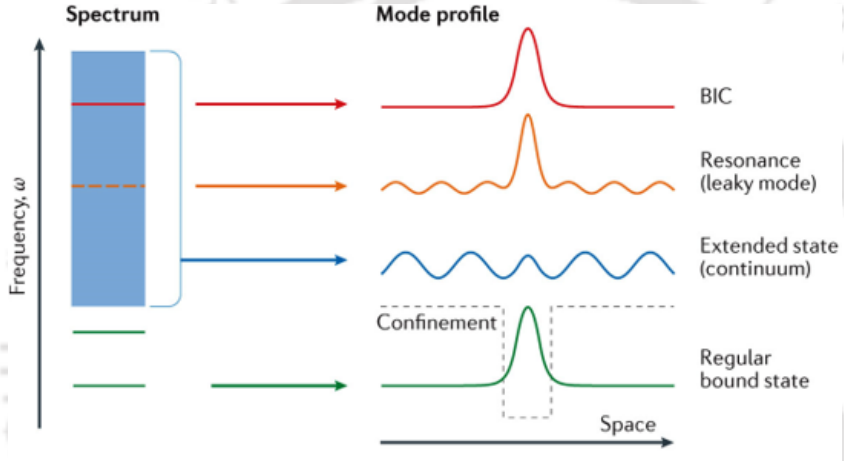

Figure 1.2: A general conceptual representation of bound state, continuum, resonance state, and BIC. Bound States in the Continuum (BICs; red) are unique states that, despite residing within the continuum, remain confined and do not radiate [1] (*Reproduced with permission from* Springer Nature. https://doi.org/10.1038/natrevmats.2016.48) .

for a long time [3]. In 1960, for the first time, L Fonda introduced the term Bound State in Continuum (BIC) for such modes. Later, the theory of BICs was extended for the description of various atomic, molecular, and quantum mechanical systems. Theoretically, ideal BIC possesses infinite lifetimes and zero linewidth, which are very sensitive to any external perturbations [4]. These bound modes become leaky modes under the effect of slight perturbation. These leaky modes are known as quasi-BIC modes, which have a finite lifetime and possess a finite high-quality factor (Q-factor) resonance. Figure 1.2 gives a general picture of the BIC in terms of modes and spatial profile. In an open system, the frequency spectrum typically comprises a continuum of spatially extended states (blue) and discrete levels representing bound states (green) that do not emit outward (shown in Fig.1.2). The spatial localization of these bound states is due to the

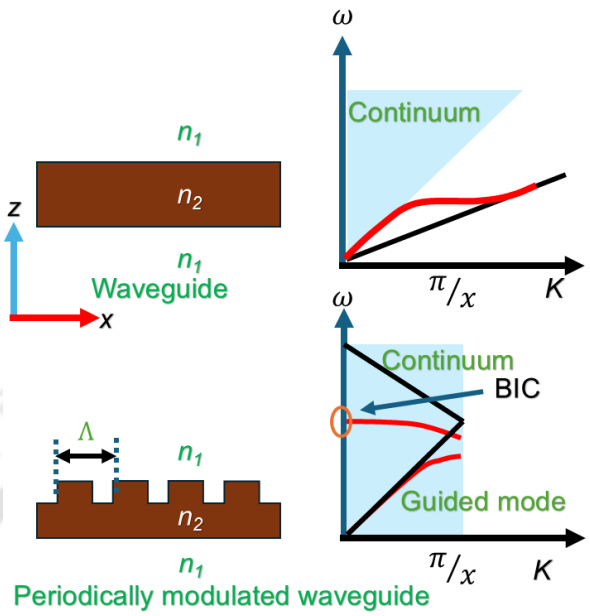

Figure 1.3: A schematic presentation of BIC in the photonic system due to the periodic patterning of the waveguide with an analogy to the potential well modulation in a quantum mechanical system.

constraints imposed by the potential (black dashed line). Generally, states within the continuous spectrum interact with free space and radiate, turning into leaky resonances (orange). However, BICs are states that defy conventional wisdom, residing within the continuum but remaining uncoupled to the free space.

Figure 1.3 shows a schematic illustration of the concept of BIC extended to a photonics system in analogy with the potential modulation in the quantum system. In a regular waveguide, the modes lie below the light line, functioning as guided modes that do not emit into the far field. However, when the waveguide is periodically modulated, the periodicity causes band folding [4]. This band folding enables certain modes to rise above the light line, leading to the emergence of a BIC within the continuum as indicated by the circle in the bottom panel of Figure1.3.

1.1.2 Types of BICs

There are two main approaches to realizing BIC in a photonics system: 1). Symmetry-protected BIC and 2). Accidental BIC. In the first approach, BIC is protected due to the symmetry of the system. In the second approach, accidental decoupling from the radiation continuum occurs due to continuous tuning of some system parameters [5][7].

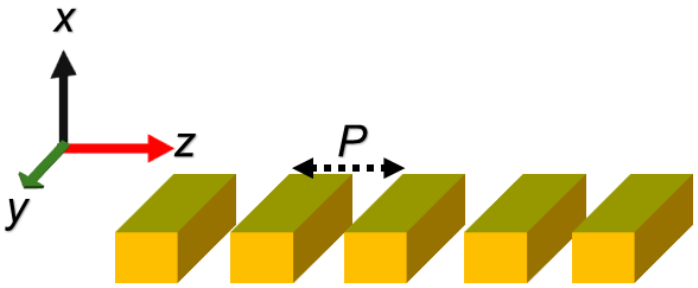

Figure 1.4: A dielectric grating with one dimensional periodicity P.

We explore the formation mechanisms of symmetry-protected and accidental Bound States in the Continuum (BICs) by considering the example of a dielectric grating with periodicity P, as shown in Fig. 1.4. According to Bloch's theorem, the electric field within this periodic structure can be expressed as [2]:

$$E_{\mathbf{k}_b}(x,y,z) = e^{i(k_b z + k_y y)} v_{\mathbf{k}_b}(x,z), \tag{1.1}$$

here $\mathbf{k}_b$ represents the Bloch wave vector, k_y is the component of the wave vector along the y-axis, and $v_{\mathbf{k}_b}(x,z)$ is a periodic function along the z-axis. This function can be decomposed into a Fourier series as follows:

$$v_{\mathbf{k}_b}(x,z) = \sum_l A_l(x) e^{i\left(k_b z + \frac{2\pi l}{P} z\right)}, \tag{1.2}$$

here $l = 0, \pm 1, \pm 2, \ldots$ labels the terms in the series, each corresponding to a distinct diffraction channel. Outside the grating, the expansion coefficients relate to plane waves as:

$$A_l(x) \rightarrow A_l e^{\pm i Q_l x}, \tag{1.3}$$

$$Q_l = \sqrt{\frac{\omega^2}{c^2} - k_y^2 - \left(k_b + \frac{2\pi l}{P}\right)^2}. \tag{1.4}$$

If Q_l is real, the diffraction channel is open, and A_l describes the complex amplitude of the outgoing wave coupled to the l-th diffraction channel. Conversely, if Q_l is imaginary, the diffraction channel is closed, and A_l represents the complex amplitude associated with the near-field. To generate a BIC, it is essential to nullify all coefficients A_l associated with open diffraction channels. For a subwavelength structure where $P < \lambda$,

only one diffraction channel typically remains open, corresponding to $l = 0$. Therefore, to create a BIC, the coefficient $A_0(x)$ must be zero. This coefficient is given by:

$$A_0(x) = \int_{-P/2}^{P/2} v_{\mathbf{k}_b}(x,z) e^{-ik_b z} dz. \tag{1.5}$$

At the center of the $\mathbf{k}$-space ($\mathbf{k}_b = 0$):

$$A_0(x) = \int_{-P/2}^{P/2} v_{\mathbf{k}_b}(x,z) dz = \langle v_{\mathbf{k}_b}(x,z) \rangle_z. \tag{1.6}$$

This equation indicates that the condition for a BIC at the Γ-point is that the z-averaged electric field components must be zero. If the unit cell of the grating is symmetric under in-plane inversion, the modes at the Γ-point can be categorized as either even or odd functions of z. Odd functions naturally have a zero z-averaged value, resulting in a symmetry-protected BIC.

The appearance of accidental BIC can be explained by Friedrich and Wintgen coupling mechanism [7]. The coupling mechanism is schematically illustrated in Fig. 1.5. We will explain the coupling mechanism in the context of a periodic photonic structure. The periodic photonic structure represents an open system. The eigenmode analysis of an open system becomes more complicated than that of a closed system [7]. In a closed system, the mode interaction can be described in a formulation of total Hamiltonian H representing a sum of unperturbed Hamiltonian and the interaction potential V. The interaction results in an intermodel mixing, and, as a result, avoided resonance crossing appears in the spectra, which is a characterizing feature for strong mode coupling [8]. However, in an open system, besides the intermodal coupling, modes are coupled to the continuum and behave as leaky waves. Figure 1.5 illustrates the conceptual picture of mode interaction in open electromagnetic systems. An open system can be considered as a closed resonator containing non-radiating modes $|\psi_a\rangle$ and $|\psi_b\rangle$, which are coupled to the radiation modes outside the resonator, following the Friedrich-Wintgen mechanism (see Figure 1.5 (a)). The modes interact with the radiation continuum(via the interaction potential V) with the adjustment of the system parameter. The frequencies and radiation losses of the modes vary with such parametric adjustment. The radiative loss can be substantially suppressed with continuous variation of the adjustment parameter and hence the interaction potential V. In such cases, a BIC or quasi-BIC appears in the spectra.

This interaction can be described using temporal coupled mode theory. If we approximate the system's response with two resonant modes, we can represent it with a vector

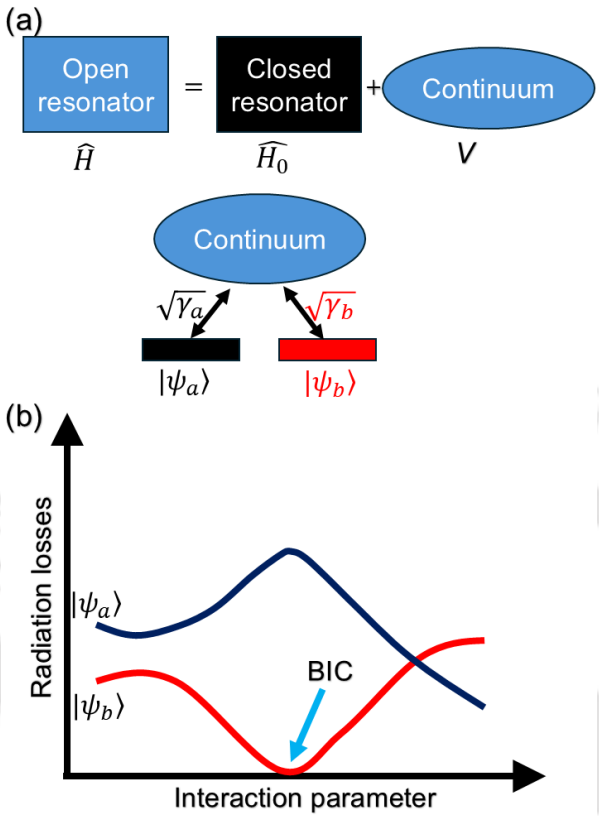

Figure 1.5: (a) A conceptual representation of an open resonator as a closed resonator (unperturbed Hamiltonian H_0 interacting with the continuum via the interaction potential V. (b) The change in radiation loss of the two leaky modes is due to the continuous tuning of system parameters. At a certain point, one of the modes turns into an accidental BIC mode with zero radiation loss.

of complex amplitudes, $\mathbf{a} = [C_a(t), C_b(t)]^T$, for states $|\psi_a\rangle$ and $|\psi_b\rangle$. The time evolution of these complex amplitudes is governed by:

$$\frac{d\mathbf{a}}{dt} = \hat{H}\mathbf{a},$$

where the Hamiltonian $\hat{H}$ includes two parts:

$$\hat{H} = \begin{pmatrix} \omega_a & \kappa \\ \kappa & \omega_b \end{pmatrix} - i \begin{pmatrix} \gamma_a & \gamma_a\gamma_b e^{i\phi} \\ \gamma_a\gamma_b e^{i\phi} & \gamma_b \end{pmatrix}.$$

Here, ω_a and ω_a represent the resonant frequencies, and γ_a and γ_b account for the coupling through the radiation continuum. The phase shift between the modes is given by ϕ. A Bound State in the Continuum (BIC) forms when the radiative losses of one of

the modes vanish after the interaction. In this two-mode approximation, the condition for forming a BIC can be written as :

$$\kappa(\gamma_a - \gamma_b) = e^{i\phi}\sqrt{\gamma_a\gamma_b}(\omega_A - \omega_B),$$

with $\phi = 0$ or π. This condition of BIC can be satisfied accidentally with a continuous variation of system parameters. This type of BICs are known as *accidental BIC* or Friedrich-Wintgen BIC.

1.2 BIC in metasurface

Dielectric photonic crystals (PhCs) have been extensively studied for exploring bound states in the continuum (BICs) due to their ability to support high-quality (Q) factor resonances without intrinsic Ohmic loss [[9]]. This is achieved through the excitation of displacement currents within the dielectric medium, minimizing electromagnetic energy dissipation and allowing for the generation of high-Q resonances [[4]]. PhCs can leverage the symmetry properties of the structure to confine modes and achieve BICs, thereby attaining sharp resonances ideal for applications in lasers [9], sensors, and filters [10][50].

However, the geometric size of the unit cells in conventional PhCs is typically on the order of the resonance wavelength. This larger geometric size results in a relatively large mode volume (V), which in turn limits the confinement of the resonant energy within the resonator cavity. In the context of cavity quantum electrodynamics (CQED), the Purcell factor, which is proportional to the ratio of Q to V (Q/V), is a critical parameter determining the efficiency of spontaneous emission rates [12]. Despite the ability of PhCs to achieve large Q factors, their relatively large mode volumes significantly reduce the Purcell factor, thus hindering the enhancement of spontaneous emission rates in these structures. This limitation poses a challenge for applications in quantum optics, such as single-photon sources and CQED-based devices [13].

Metamaterials have emerged as a promising alternative to address these limitations. Metamaterials consist of sub-wavelength dimensions building blocks. By carefully designing the geometry of these resonators and optimizing their mode properties, the resonant mode volume can be localized to the subwavelength scale [14] [15]. Gupta et al. explored a planar metamaterial design with excellent subwavelength field confinement

and enhancement of $\frac{Q}{V}$ ratio (Purcell factor), with enhanced light-matter interaction [16]. This transition from traditional PhCs to subwavelength metamaterial platforms represents a significant advancement in the design of photonic structures capable of supporting high-Q BICs. By leveraging the deep subwavelength confinement and enhanced $\frac{Q}{V}$ ratios, metamaterials open new avenues for creating the next generation of miniaturized, efficient devices for quantum computing and communication.

1.2.1 Metamaterials and metasurfaces

Material development always plays an important role in the evolution of technologies. Materials with unique properties, which are usually unavailable in natural materials, may lead to a new application or replace the oldest one with a higher degree of efficiency. Almost all electromagnetic devices work based on the interaction between waves and material. The Earth is abundant with natural resources, which humanity has harnessed to achieve the current milestones in science and technology. Despite this progress, sometimes the natural law limits the desirable electromagnetic response of the wave-matter interaction. However, in some cases, the eligible material medium does not exist in nature. This quest has led to the emergence of metamaterials, a novel category of man-made materials. To produce the desired electromagnetic properties of a substance, scientists manipulate the structure of the substance at the molecular level(e.g., Teflon). This kind of material is known as synthetic material. In another approach, the design and arrangements of elements in the subwavelength domain can create an inhomogeneity larger than the molecular scale but smaller than the wavelength of interest. This kind of new material can be described in terms of effective electromagnetic parameters. Such artificial, man-made materials are termed as metamaterials.

The exact definition of metamaterials is still unclear, and there is no unique or universally accepted definition yet. The European Union's Metamorphose Network defines metamaterial as "an arrangement of artificial structural elements designed to achieve advantageous and unusual electromagnetic properties." However, this definition is inadequate to distinguish the metamaterials from other man-made structures like photonic crystals. A most appropriate definition was given in the book[17], "*A metamaterial is an artificially structured material which attains its properties from the unit structure rather than the constituent materials. A metamaterial has an inhomogeneity scale that is much smaller than the wavelength of interest, and its electromagnetic response is*

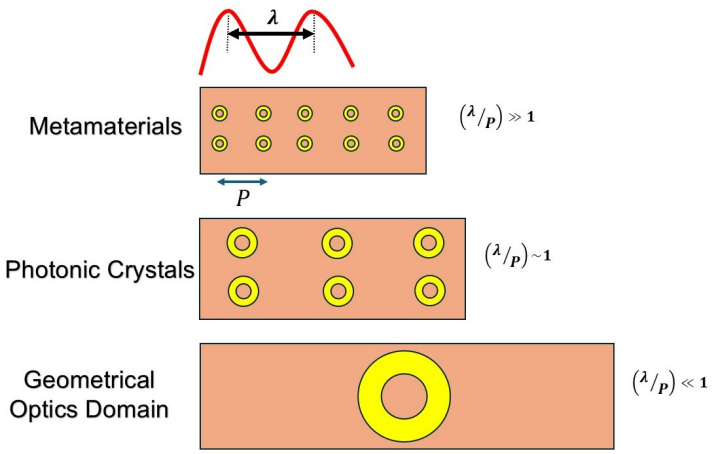

Figure 1.6: Levels of inhomogeneity in Optical materials: Subwavelength structures, such as metamaterials, are made of meta-atoms smaller than the wavelength, resulting in a uniform appearance. At the wavelength scale, diffraction and interference dominate, as seen in photonic crystals. At larger scales, geometrical optics and ray tracing apply.

expressed in terms of homogenized material parameters." The electromagnetic properties of metamaterials can be represented by average homogeneous electric permittivity (ϵ) and magnetic permeability (μ) due to its sub-wavelength inhomogeneity.

The sub-wavelength unit cells of metamaterial are known as "meta-atoms" that are designed to exhibit electromagnetic properties unattainable by natural materials. These meta-atoms form the fundamental components of the metamaterials and are strategically positioned within them. Consequently, metamaterials' optical and physical properties can be tailored by altering the meta-atom's shape, orientation, size, or geometry. From the general aspects of electromagnetics, wavelength determines whether or not a periodic collection of objects or atoms will be considered material. The three different levels of inhomogeneity are illustrated in Fig 1.6. Starting with the smallest dimension, the first level is subwavelength, where metamaterials are situated. The fundamental building block of metamaterials is smaller than the wavelength of interest. The spacing between meta-atoms is in the subwavelength range, giving metamaterials a macroscopically uniform appearance. This characteristic allows us to classify metamaterials as "materials" rather than devices [17]. When a structure has dimensions in the order of wavelength, phenomena such as diffraction and interference become dominant. Examples include X-ray diffraction in crystals, photonic crystals in optics, and phased array radars in microwave frequencies. When the inhomogeneity size is even larger, the structure is typically described using geometrical optics and ray tracing.

The concept of metamaterials does not impose additional restrictions beyond size. Although, in most cases, meta-atoms are arranged periodically, there are examples of randomly arranged metamaterials with remarkable electromagnetic properties.

The groundwork for the research in modern metamaterials started with the publication of widely known research by Victor Veselago in 1968 [18]. In this paper, Veselago predicted the possibility of the existence of materials with both negative permittivity and permeability. The paper also discussed the material parameters required to achieve the negative refractive index. The exploration of negative permittivity and permeability can be described using Maxwell's equations.

$$\nabla \cdot \vec{E} = \frac{\rho}{\varepsilon} \tag{1.7}$$

$$\nabla \times \vec{E} = -\frac{\partial \vec{B}}{\partial t} \tag{1.8}$$

$$\nabla \cdot \vec{B} = 0 \tag{1.9}$$

$$\nabla \times \vec{B} = \mu\vec{J} + \varepsilon\mu\frac{\partial \vec{B}}{\partial t} \tag{1.10}$$

Equations 1.1 and 1.2 can be solved by considering the plane wave electric and magnetic component as,

$$\vec{E} = E_0 \exp(i\vec{k} \cdot \vec{r} - i\omega t)$$
$$\vec{H} = H_0 \exp(i\vec{k} \cdot \vec{r} - i\omega t)$$

The equations (1.8) and (1.10) simplifies to

$$\vec{k} \times \vec{E} = \mu\omega\vec{H}$$
$$\vec{k} \times \vec{H} = -\varepsilon\omega\vec{E}$$

For both μ and ϵ positive, the above equations form a right-handed orthogonal system, and hence, light will refract to the right, obeying Snell's law of refraction. For left-handed propagation to occur while still satisfying Maxwell's equations, the material must have a refractive index $n < 0$, which implies that both the permittivity ϵ and the permeability μ are negative. In such materials, the direction of wave propagation, the electric field, and the magnetic field form a left-handed orthogonal system, which is contrary to the usual right-handed system observed in conventional materials. Figure 1.7 shows the categorization of the material in terms of electric permittivity ϵ and magnetic permeability (μ). Region I comprises materials with both positive permittivity and permeability, depicting

common transparent dielectric materials. The following quadrant, Region II, includes metals, ferroelectric materials, and doped semiconductors characterized by negative permittivity and positive permeability. Region III is the zone predicted by Victor Vesalago; no naturally occurring materials exhibit both negative permittivity and permeability. The final quadrant, Region IV, contains ferrite materials with positive permittivity and negative permeability. Vesalago's theory remained theoretical until 1999 when Sir John Pendry introduced metamaterials as a new category of materials. This breakthrough launched an entirely new field of research that continues to be highly relevant today. The modern era of metamaterial started after the experimental demonstration of the simultaneously negative value of effective permittivity and permeability, first in the microwave region by Smith *et al.* [19], using a composite structure of split ring resonator and thin wire. This work predicted that the structure forms a left-handed medium, and hence, Snell's law will be inverted for this medium. In 2001, Shelby *et al.* experimentally tested the negative refractive index metamaterial [20], as shown in Figure 1.8 (a). Figure 1.8 (b) shows the detected power calculated as a function of the angle of refraction according to Snell's law experiment. Microwave radiation is made to incident on the prism-shaped metamaterial sample, and a refraction opposite to the surface normal is recorded. A wedge-shaped sample made of Teflon material is used as a reference, which shows the refraction of the radiation at an opposite angle to the normal as per its known positive refractive index value. The observation validates the negative refraction of the fabricated metamaterial sample. Although the initial work on metamaterials only focused on the negative index metamaterials. But today's metamaterial-based works are no longer limited to negative refraction. Various artificially made electromagnetic metamaterials show extraordinary properties that are usually not available in natural materials and cannot be achieved by synthesized material.

Metasurfaces are the surface version or two-dimensional equivalent of metamaterial . The research on metasurfaces has gained significant attention in recent years because they offer electromagnetic manipulation, light focusing in a ultra thin sub wavelength features. Metasurfaces are often a useful alternative to metamaterials for many applications. One key advantage of metasurfaces is that they occupy less physical space compared to full three-dimensional metamaterial structures. The sub-wavelength ultra-thin features may open the door for developing miniaturized metasurface-based optical devices. This ultra-thin feature of metasurface enables the creation of highly efficient optical components, such as lenses[22], holograms [23], and beam splitters [24], on a

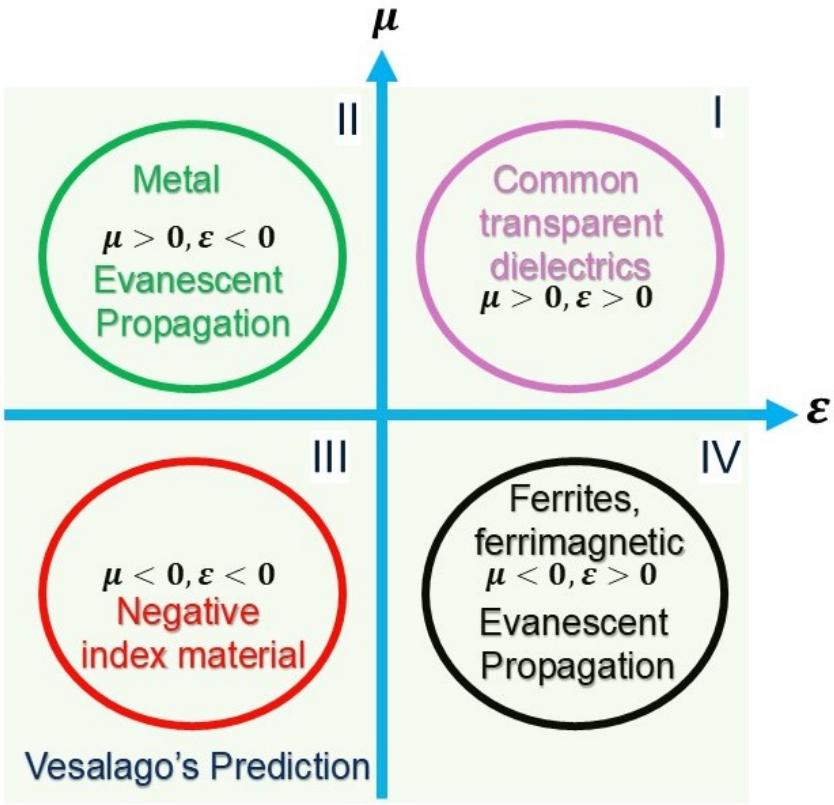

Figure 1.7: Categorization of materials based on their electric permittivity (ϵ) and magnetic permeability (μ). The diagram illustrates four quadrants, with each representing a different type of material. The fourth quadrant, where both μ and ϵ are negative, denotes Veselago's predicted negative refractive index materials.

compact scale. Additionally, metasurfaces tend to show low absorption losses due to their planar structure, making them less lossy than their 3D metamaterial counterparts. These advantages make metasurfaces an attractive option for applications in imaging, sensing, and communication technologies.

1.2.2 Metallic metasurface Vs All-dielectric metasurface

Metallic metasurfaces have been widely used in various applications due to their ability to manipulate electromagnetic waves effectively. However, their intrinsic ohmic losses significantly limit their application, particularly at optical and near IR frequencies. In contrast, all-dielectric metasurfaces offer a promising alternative due to the absence of ohmic losses. These metasurfaces are typically composed of high-refractive-index

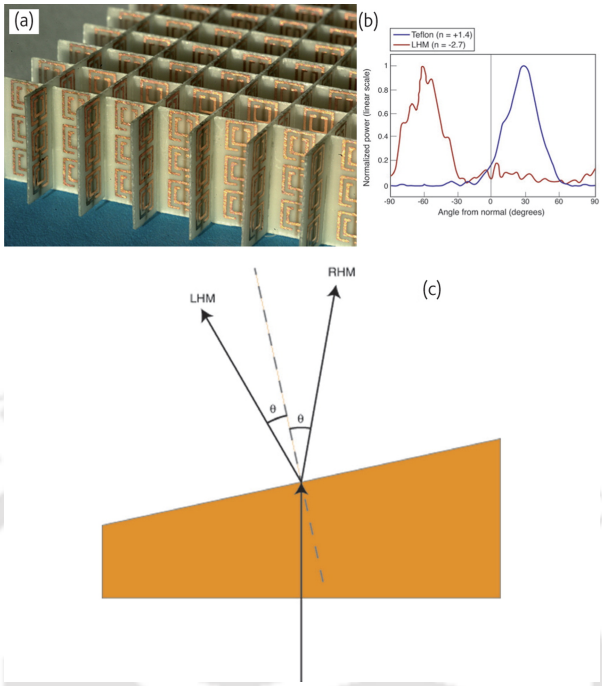

Figure 1.8: (a) The fabricated negative refractive index metamaterial. The metamaterial structure is made up of a combination of a split-ring resonator and wire lithographically deposited on the opposite side of a circuit board. The thickness of the structure is 1 cm. (b) Experimental demonstration of the negative refractive index phenomena according to Snell's law. The plot shows detected power as a function of angle from the normal. (c) A schematic representation of the geometry that is used to demonstrate a negative index of refraction[20].

dielectric materials, which allow them to efficiently manipulate electromagnetic waves without the energy dissipation associated with metals.

All-dielectric metasurfaces can support both electric dipole (ED) and magnetic dipole (MD) resonances through Mie scattering, even in simple structural geometries [21]. While metallic metasurfaces can also exhibit simultaneous electric and magnetic dipole responses, they typically require some specific configurations, such as split-ring resonators (SRRs) or stacked direct, complementary structures. Moreover, dielectric metasurfaces offer lower losses and higher quality factors, making them advantageous for many applications. Even when magnetic resonances are achieved, the ohmic losses in metals still show a significant drawback.

Furthermore, the potential for integration into on-chip photonic systems makes all-dielectric metasurfaces a promising candidate for future nanophotonic-based applications. Their compatibility with existing semiconductor fabrication processes allows for the seamless integration of these metasurfaces into photonic circuits.

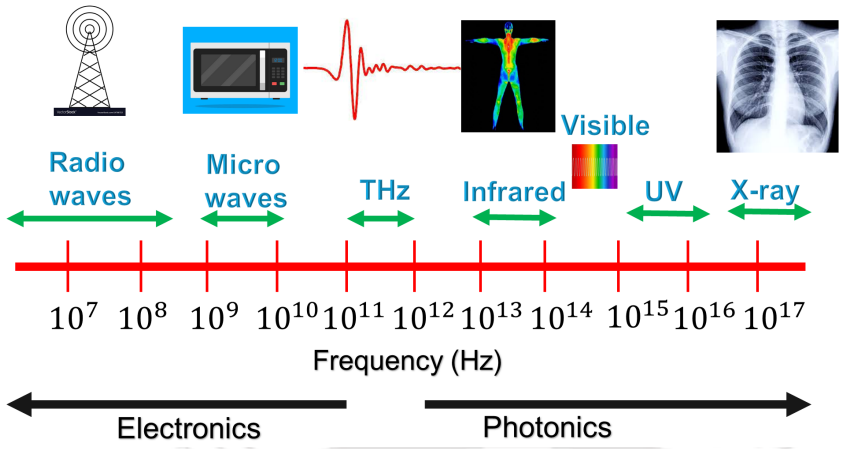

Figure 1.9: Position of the terahertz region in the electromagnetic spectrum.

In this thesis, we investigate metallic metasurfaces in the terahertz region while focusing on all-dielectric metasurfaces in the near-infrared region to minimize ohmic losses and meet the requirements of our targeted applications. The following section provides a comprehensive discussion of the fundamental resonances in terahertz split-ring resonator metasurfaces. We further present a brief discussion of the evolution of quasi-BIC resonances with varying degrees of asymmetry for metasurfaces in both the near-infrared and terahertz regions in section 1.2.4.

1.2.3 Terahertz metasurfaces

The terahertz (THz) frequency range, which covers the frequency range of about 0.1 THz to 10 THz, lies between the infrared and microwave regions of the electromagnetic spectrum [25]. Fig. 1.9 shows the terahertz frequency region in the electromagnetic spectrum. The THz range was largely unexplored for many years, mainly because of the absence of efficient sources and detectors for THz spectroscopy and imaging. Hence, this unexplored region was often called the "THz gap," which created substantial obstacles to the progress of THz science and technology. However, recent breakthroughs have shown significant progress in generating, detecting, and manipulating THz waves. These advancements open the avenue to the creation of new efficient THz-based devices with broader potential applications in areas such as imaging, sensing, and communication [45], [27]. Unlike the microwave or infrared regions, which are typically described by their wavelength (usually in centimeters or nanometers), the THz region is mainly defined by its frequency range. The THz band overlaps with the neighboring spectral

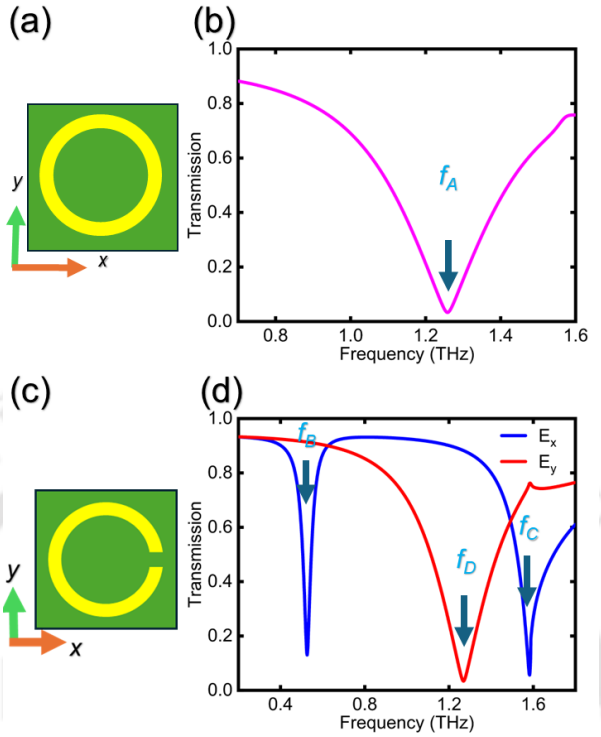

Figure 1.10: (a) A closed ring resonator metamaterial unit cell with radius 30 μm, width 6 μm and periodicity 90 μm on the top of a quartz substrate. (b) Simulated transmission spectrum for the closed ring resonator. (c) A circular Split Ring Resonator, with a split gap of 6 μm, while all other geometrical parameters are the same as the closed ring resonator. (d) The simulated transmission plot for two orthogonal polarizations of incident electromagnetic waves.

bands, such as the millimeter-waveband, the submillimeter-waveband, and the far-IR band. Thus, describing the THz region by frequency rather than wavelength provides a clearer definition with less ambiguity. Additionally, the fundamental resonances (phonons and molecular vibrations) of many materials, are in the terahertz (THz) frequency range. These resonances are more effectively discussed when considered in terms of frequency rather than wavelength. Devices based on metasurfaces that operate in the THz domain hold particular promise for enhancing THz applications due to their unique characteristics, such as subwavelength control of electromagnetic waves, phase manipulation, and high transmission efficiency [45].

1.2.3.1 Different types of resonances in a THz SRR metasurface

In this thesis, we will focus on the resonant behavior of metallic rings and split ring structures in the terahertz frequency region. A simple single-gap SRR comprises a circular or square metallic ring with a split gap. An SRR shows different kinds of

resonance behavior under the different states of incident polarization. For instance, under different polarization states, the SRR can show broad dipole resonances, LC resonance modes, or other complex resonance behaviors. Here, we present a brief discussion starting with the most commonly observed broad dipole resonance. Fig. 1.10 (a)and (c) depicts the unit cell of closed ring metasurface and circular split ring metasurface with periodicity 90 μm, radius 30 μm, width 6 μm and split gap of 6 μm. In the figure, the metasurface is simulated with aluminum $\sigma = 3.56 \times 10^7$ S/m on a quartz substrate $n_{quartz} = 2.09$; simulation methods will be discussed in Chapter 2. A closed ring resonator shows a broad dipole resonance dip (denoted by f_A) under the excitation of normally incident terahertz radiation (as shown in Fig. 1.10 (b)). The ring-type resonator can be modified by introducing a gap. The gap and the metallic arm induce an effective capacitive and inductive effect, respectively, forming an equivalent LC-type resonator. This concept was first introduced in Pendry's foundational work on metamaterials. The LC-type resonator, depicted in Fig. 1.10 (c), includes a circular-shaped design. However, we can have the same electromagnetic resonant response by using a square-shaped resonator. Due to the lack of symmetry about the Y-axis, the structure displays polarization-dependent resonances. This polarization dependence is observed as an order-like behavior between the resonances when subjected to x and y polarizations (as shown in Fig. 1.10 (d)). For convenience of discussion, we have marked the spectral positions of the resonance mode as f_A, f_B, f_C and f_D. For polarization perpendicular to the gap of SRR, a broad resonance dip can be observed at frequency f_D. For y-polarization, where the electric field is parallel to the gap, the broad dipole mode f_D splits into a fundamental LC mode (f_B) and a third-order mode (f_C). The LC resonance exhibits characteristics akin to electronic circuits, where energy is stored in the capacitor and inductor. This resonance is less radiative and narrower compared to the broad dipole resonance (f_A), reflecting the energy retention within the LC circuit. Figure 1.11 presents the Z component of the electric field distributions and surface current distributions of the resonators at different resonance frequencies. Figures 1.11 (a) and (d) show the near field distribution and surface current profile of the broad resonance at f_A corresponding to the closed ring. The charge distributions and parallel surface current closely resemble the dipole nature of the resonance mode. Figures 1.11(b) and (e) present the electric field distributions (normal component) and surface current profile for the split ring resonator metasurface when the polarization is along the gap. The fundamental LC resonance mode f_B is characterized by a single closed loop of surface currents and charge polarity at the split gap (Fig. 1.11

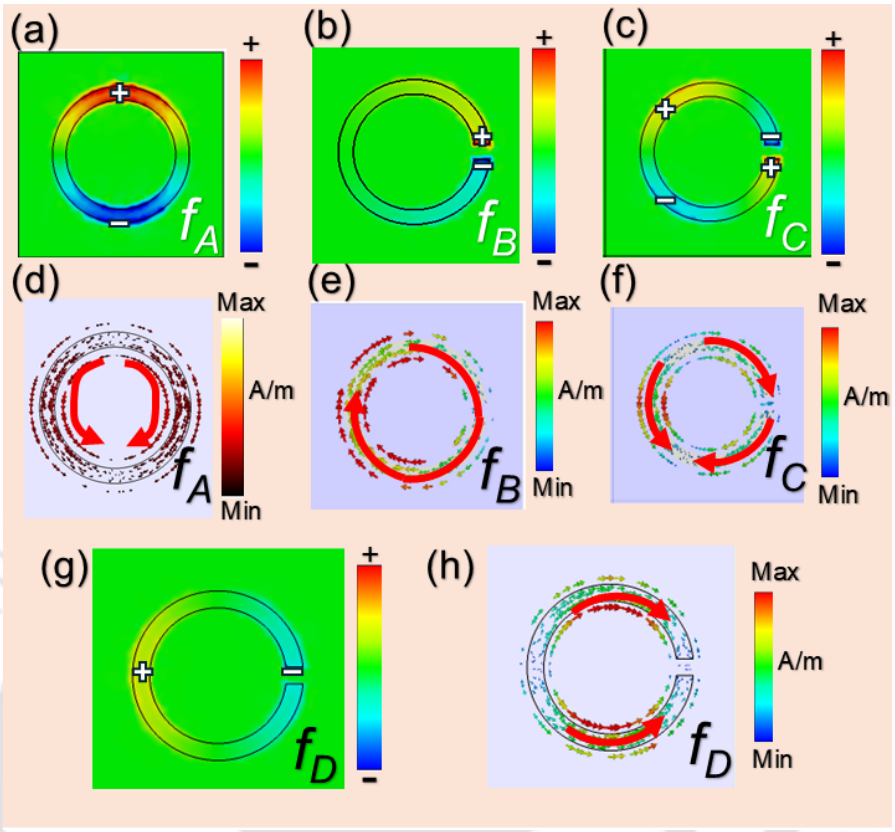

Figure 1.11: The Z component of the electric field distributions and surface current distributions for (a,d) the closed ring resonator at frequency f_A, (b,e) the circular split ring resonator LC resonance mode at frequency f_B, (c,f) the circular split ring resonator second resonance mode at frequency f_C, (g,h) the circular split ring resonator at frequency f_D with the electric field polarized perpendicular to the gap.

(b)). The second order mode at frequency f_C corresponds to three branches of surface currents (as shown in Fig. 1.11 (f)). The charge distribution closely resembles the nature of a quadrupolar mode. The SRR shows a dipole resonance (at frequency f_D)behavior when polarization is perpendicular to the split gap (as shown in Fig. 1.11(g) and (h)).

In contrast, the second-order resonance f_D manifests under X-polarization, where parallel surface currents form a resonance pattern akin to the dipole resonance (as shown in Fig. 1.11(g) and (h)) as described earlier. This intricate behavior demonstrates the impact of polarization on the resonance modes of the LC-type resonator, highlighting its potential for tailored electromagnetic responses in metamaterial applications.

1.2.4 Quasi BIC resonance and their spectral properties

An ideal BIC is a mathematical concept. It is actually the quasi-BIC mode that manifests as a sharp Fano resonance. The BIC mode with infinite Q factor (zero linewidth) transforms into a quasi-BIC mode under the effect of symmetry breaking or continuous parameter tuning. In the symmetry-protected BIC mechanism, the resonance mode evolves with the degree of asymmetry. The excitation of quasi-BIC mode in the metasurface via symmetry breaking effect has been explored in many works [1]. The in-plane symmetry of the metasurface is disturbed by introducing asymmetry in the unit cell. In such cases, the ideal conditions that completely nullify the radiation in the BIC no longer hold. However, the coupling to the radiation continuum remains weak. The extremely weak coupling to the radiation continuum creates a sharp resonance in the spectrum—referred to as a quasi-BIC. The closer the system parameter is tuned to its symmetric configuration, the higher the Q-factor of the quasi-BIC. In the following subsections, we will discuss the spectral characteristics of quasi-BIC mode in the metasurface for near-infrared and terahertz frequency regions.

1.2.4.1 Quasi-BIC Resonance in the Near-Infrared Domain

‘ The transition from ideal Bound States in the Continuum (BICs) to quasi-BICs is crucial for tuning resonant properties and achieving high-Q factors. In the context of symmetry-breaking BIC, many interesting works have been reported. Koshelev *et. al* have shown that the sharp spectral resonances recently observed in different types of meta-atom designs (plasmonic and dielectric) are fundamentally a consequence of the symmetry-protected BIC mechanism [4]. These resonances occur due to the breaking or distortion of symmetry that protects the BIC from radiating. It is also reported that the radiative quality factor follows a general law: proportional to the inverse square of the defined asymmetric parameter

$$Q = \frac{C}{\alpha^2}, \tag{1.11}$$

, where C is a constant depends on the geometry of the system and α is the degree of asymmetry. Figure 1.12 shows the divergence nature of quasi BIC mode's Q factor as the asymmetry decreases for different asymmetric meta-atoms, each defined with a different asymmetry parameter. In context with this reported finding, Li *et. al* proposed a symmetry-protected BIC supported by metasurfaces composed of silicon nanodisks [72]. The in-plane symmetry $(x, y) \leftrightarrow$ (-x,-y) of the metasurface unit cell is broken by adding or

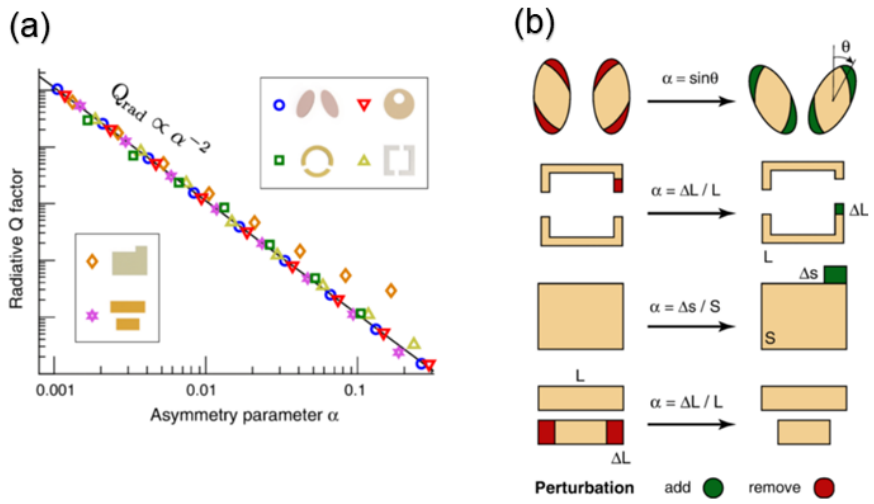

Figure 1.12: Effect of symmetry breaking in the additive Q factor of quasi BIC mode ; (a) Q factor dependence on in-plane asymmetry parameter defined by the meta-atom as shown in (b). The change in the Q factor follows an inverse square law of the asymmetry. (b) Different types of asymmetry meta-atom and the definition of asymmetry, α. © 2018 American Physical Society. Reprinted with permission. `https://doi.org/10.1103/PhysRevLett.121.193903`

.

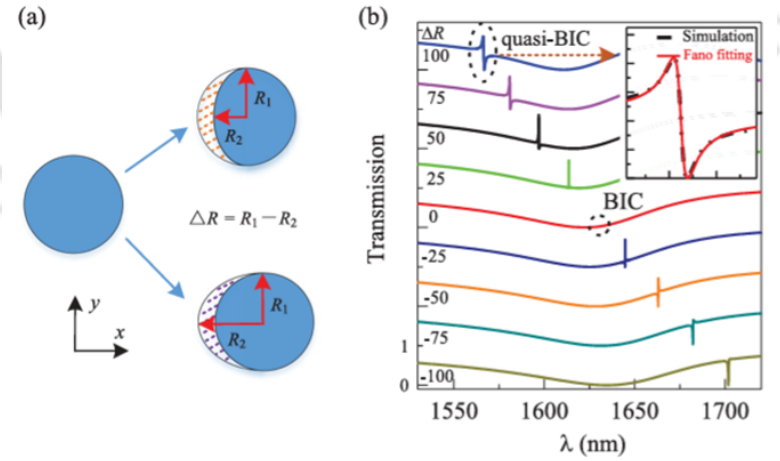

Figure 1.13: (a) Schematic model of the symmetric Si nanodisk and two asymmetric Si nanodisks after removing (top) or adding (bottom) a part of the disk from the left edge. The SiO_2 substrate is omitted for simplicity. (b) Evolution of the quasi-BIC mode in the transmission spectra with the asymmetry ΔR.© 2019 American Physical Society. Reprinted with permission. `https://10.1103/PhysRevA.100.063803`

removing a portion from the nanodisk. Figure 1.13 (a) illustrates the in-plane symmetry-breaking process of the meta atom. The disappearance of the sharp Fano resonance as long as the structure attains the symmetry is a characteristic of the symmetry-protected quasi-BIC mode. Figure 1.13 (b) shows the evolution of the quasi-BIC mode from the BIC mode. The radius of the symmetric nanodisk is marked by $R_1 = 400nm$, and the length from the center to the left edge of the disk after perturbation is marked by R2. The degree of asymmetry is defined as $\Delta R = R_1$-R_2. The difference between R_1 and R_2 perturbs the in-plane symmetry of the structure. As ΔR decreases, corresponding to the removal of a portion from the edge of the nanodisk, the resonance becomes sharper. The sharp resonance mode disappears in the transmittance spectrum as ΔR reaches zero, indicating a symmetric nanodisk. This singularity point (diverging Q factor or negligible linewidth) at approximately 1630 nm of wavelength, when $\Delta R = 0$, signifies the presence of a bound state in the continuum (BIC), with no energy leakage to free space. As ΔR is further decreased, meaning a larger portion is added to the nanodisk, the resonance broadens again. The introduction of asymmetry in the nanodisk leads to the emergence of asymmetric Fano resonances, indicative of quasi-BIC states. The interference between the discrete state or bound state of the metasurface and the continuum results in a sharp asymmetric Fano lineshape resonance [72] [30].

1.2.4.2 Quasi-BIC Resonance in terahertz metasurface

‘

Terahertz metasurfaces that exploit symmetry-protected BIC resonances are designed by breaking the structural symmetry. The intentional geometrical asymmetry enables precise tuning of the frequency and Q factor of the resonance mode. Cong *et al.* explored dual BIC mode excitation in a planar double-split gap split-ring resonator (SRR) metasurface [31], as shown in Fig. 1.14. The SRR metasurface demonstrates the excitation of two distinct quasi-BIC modes: a sharp Fano resonance and an Electromagnetically Induced Transparency (EIT)-like resonance, for incident polarizations along the x- and y-axes, respectively. The transition from BIC to a quasi-BIC mode is explained by the effective electric dipole moment (as shown in Figure 1.14 (c)). For a linearly polarized incident plane wave, coupling occurs only with modes having net electric components along the x- or y-axis. For symmetric SRR, both y-polarization and x polarization of incident wave results in a net zero effective dipole moment. However, the induced asymmetry

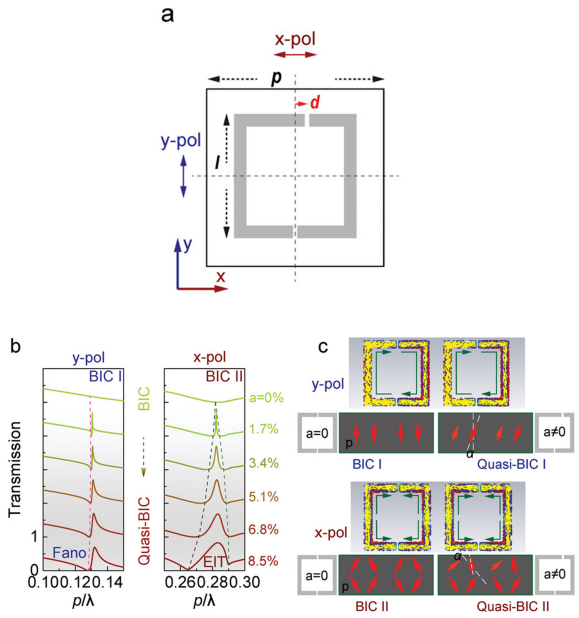

Figure 1.14: Exciation of quasi BIC mode as Fano and EIT lineshape by introducing structural asymmetry. a) A mirror symmetry broken Split Ring Resonator, where asymmetry is introduced by displacing the gap from the center with a distance "d." A dimensionless parameter "a" is defined to express the asymmetry degree quantitatively $a = \left(\frac{l_1 - l_2}{l_1 + l_2}\right) \times 100\%$, where l_1 and l_2 indicate the total length of the left and right branches of the resonator, respectively. b) The evolution of the Fano and EIT-like quasi-BIC mode in the transmission spectra at different asymmetry degrees for y- and x-polarizations. c) Analysis of resonance mechanism by electric dipole moments at y- and x-polarizations. The induced geometrical perturbation causes the leakage of the ideal BIC mode. Adapted with permission from [31] *John Wiley and Sons*, Copyright © 2019 DOI:doi.org/10.1002/adom.201900383.

disturbs the dipole alignment as well as the magnitude, which allows the coupling of the quasi-BIC mode to the free space radiation continuum. In line with this work, Tan *et al.* reported a method to enhance the Q factor of symmetry-protected quasi-BIC resonance mode by coupling with the fundamental lattice mode [116]. The lattice mode is a trapped mode confined to the substrate. Hence, coupling the quasi-BIC resonance mode with the fundamental lattice mode can significantly reduce the radiative loss.

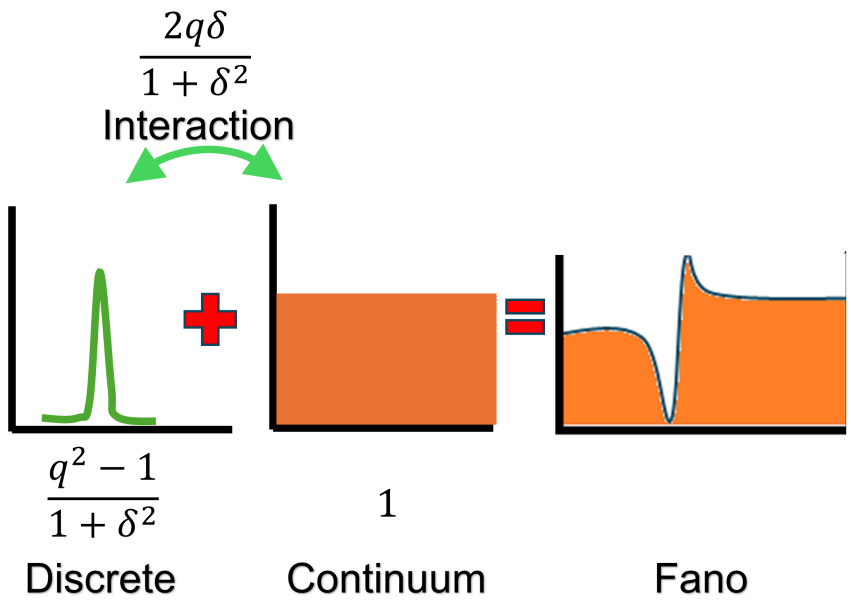

Figure 1.15: A visual representation of the Fano formula, depicting the mixing of a discrete (Lorentzian) state and flat continuum, which results in a Fano line shape.

1.3 Fano resonance and their relation to BIC

1.3.1 Fano Resonance: Concept and Mechanism

In general, Fano resonance arises due to the interference between a discrete state and a continuum of states, resulting in an asymmetric spectral lineshape. In 1961, Ugo Fano discovered the asymmetric Fano lineshape resonance in the context of atomic physics [33]. He explained the asymmetric lineshape observed in the photoionization spectra due to the interference of direct ionization and a resonant excitation path. The hallmark of Fano resonance is its distinctive asymmetric profile, featuring a sharp peak followed by a dip. However, a simple tool to prove the existence of Fano resonance is to fit the observed spectrum with the Fano formula [34]:

$$R(\omega) = A_0 + F_0 \cdot \frac{\left(q + 2\frac{\omega-\omega_0}{\Gamma}\right)^2}{1+\left(2\frac{\omega-\omega_0}{\Gamma}\right)^2}$$

, where A_0 and F_0 are constant terms, q is the Fano asymmetry parameter, ω_0 is the resonance frequency, and Γ represents the linewidth of the resonance frequency. The Fano asymmetry parameter q represents the ratio between resonant and nonresonant states. Fig 1.15 presents a pictorial description of the discrete-continuum interaction involved in the process of generation of Fano resonance. The Fano formula can be decomposed

into the following terms [35]:

$$R(\omega) = A_0 + F_0 \cdot \frac{(q^2-1)}{\delta^2+1} + F_0 \cdot \frac{(1+\delta^2)}{\delta^2+1} + F_0 \cdot \frac{2q\delta}{\delta^2+1}$$

here, $\delta = 2\frac{\omega-\omega_0}{\Gamma}$, the first and third term contributes to the background radiation continuum. The second term represents the discrete Lorentzian line shape, and the last term indicates the mixing between the two states. In the limit where the asymmetry parameter $q \to \infty$, the coupling between the discrete state and the continuum becomes very weak. Under these conditions, the resonance line shape is dominated by the discrete state, leading to a typical Lorentzian profile.

The strengths of the transitions to both the continuum and the discrete state become comparable when the asymmetry parameter $q = 1$. A particularly interesting case occurs when the asymmetry parameter $q = 0$. This indicates a zero coupling to the discrete state, resulting in quasi-Lorentzian anti-resonance in the spectrum.

1.3.2 Interplay between Fano resonance and BIC

The connection between Fano and BIC is that both phenomena are a result of destructive interference coupling. Both originate from interference effects and involve coupling mechanisms, but they differ in their nature, spectral characteristics, and dependence on symmetry. This section explores the concept and mechanisms of Fano resonances, their manifestations in metasurfaces, and their relation to BICs. A Bound State in the Continuum (BIC) can be distinguished by its defining property: when there is zero asymmetry, it exhibits an infinite quality (Q) factor and disappears from the scattering spectrum, indicating no radiation loss. If a Fano resonance shows this characteristic, where it vanishes from the scattering spectrum under perfect symmetry conditions, then it is a symmetry-protected quasi-BIC mode. Strictly speaking, all photonic modes can exhibit a Fano lineshape spectrum due to the interference between different pathways. Therefore, they can all be referred to as Fano resonances. However, only those modes that meet the aforementioned criteria, having an infinite Q factor and no spectral presence in the absence of asymmetry, are true BICs. Fano resonances can occur in a variety of metasurfaces, both symmetric and asymmetric, as long as there is some coupling.

1.4 Motivation

The losses in metasurface directly impact its performance efficiency, and it remains a crucial objective for researchers to explore ways to minimize losses. The inherent nonradiative losses can be minimized by properly choosing the constituents of the meta-atoms. However, the radiative losses persist across the entire electromagnetic spectrum. The excitation of symmetry-protected quasi-BIC mode by introducing structural asymmetry in a metasurface can effectively address these challenges. This kind of trapped resonance mode shows weak coupling to the broad radiation continuum and manifests as a sharp Fano lineshape. In this thesis, we have explored these aspects in metasurfaces operating in the terahertz and near-infrared frequency regions.

1.4.1 Choice of two different frequency ranges

We explored the design and application of metasurface-based devices across two different frequency ranges: the terahertz (THz) and near-infrared (C band) regions. In the near IR region, we have studied the excitation of quasi-BIC mode, its evolution and its application as a narrow band pass filter and sensors. The study of metasurface-based designs in the near-infrared (C band) frequency regions can bring significant scientific and technological advancements based on their unique properties for diverse applications. As mentioned previously, the terahertz frequency region exhibits distinctive properties, such as low ionization and unique spectral responses. Fundamental research and exploration of metasurface-based high Q factor devices in the THz region can enhance the utility of this unexplored frequency range. Hence, both of these frequency ranges offer unique advantages for various technological applications.

The near-infrared (C band), specifically in the wavelength range of 1535 nm to 1565 nm, is critical for applications in telecommunications, sensing, and spectroscopy. This wavelength range is particularly significant in low-loss optical fiber communication. This range of wavelength corresponds to the low attenuation transmission window of optical fibers. As a result, it is the preferred range for high-capacity data transmission in long-haul and metro networks. In this context, the metasurface-based ultra-narrow bandpass filter we designed specifically for the 1535 nm to 1565 nm range plays a crucial role. It allows selective passing of desired wavelengths while blocking unwanted signals. The ultra-narrow bandwidth enhances the selectivity of a particular wavelength and

hence may enhance the performance of the optical communication system. Furthermore, this near-IR wavelength range is essential for various sensing and spectroscopic applications. For example, near-infrared spectroscopy in the C band is widely used to identify and analyze chemical compositions and biological samples, where precise control of the wavelength, enabled by narrow bandpass filters, ensures accurate detection and measurement.

In summary, utilization of both the THz and near-infrared (C band) frequencies allows for a diverse set of applications, ranging from sensing to high-performance communications. High Q terahertz metamaterials enable the manipulation and enhancement of THz signals for material detection and data transmission, while the narrow bandpass filter in the 1535 nm to 1565 nm range optimizes optical communication.

1.4.2 Motivation for Quasi-BIC Excitation in Metasurfaces at THz and NIR Frequencies

Resonances with high-quality factors are important in all branches of physics and engineering, including acoustics, electronics, and photonics. In general, a high Q factor represents the high ability of a physical system to store energy. In photonics, high-Q resonances directly link to the continuous series of advancements in both fundamental research [1] and practical device applications [2]. Devices with high Q factor resonances ensure low radiative losses and increase the sensitivity of the localized field to external perturbation [47]. These are both important features for applications like sensors and narrow-band filtering. A sharp resonance mode (high Q) can detect the minute level shift in its resonance spectra. Further, the enhancement of localized near-field distribution gives a strong light-matter interaction, making such resonances suitable and promising for sensing. A high Q resonance with a very narrow passband and flat sideband is a good candidate for narrowband filtering applications. Metal shows high absorption and significant ohmic losses in the C band wavelength region. The use of an all-dielectric metasurface can overcome these issues. The excitation of high Q quasi BIC mode by breaking the structural symmetry of the metasurface offers precise tunability of the resonance linewidth as well as amplitude. In addition, metasurface-based devices offer less bulky and miniaturized alternatives to traditional bulky optical components [37]. This miniaturization allows for more compact devices, making them ideal for on-chip photonics application. In this context, our first study involves a theoretical demonstration

of an ultra-narrowband pass filter in the optical C-band (1535 nm-1565 nm) exploiting a symmetry-protected quasi-BIC resonance. An ultra-narrow band filter can be useful in applications such as spectral imaging [38], efficient displays [50], etc.

Based on the fundamental concept of high-Q resonance excitation in symmetry-broken meta-atoms, the subsequent work explores an all-dielectric metasurface-based dual parametric (refractive index and temperature) sensor in the near-infrared (IR) region. A sharp resonant response enhances the sensor's sensitivity to minute environmental changes. Such an approach effectively utilizes the low-loss nature of dielectric materials, promising the excitation of high Q quasi-BIC mode. Furthermore, the miniaturized, metasurface-based sensor can push the boundaries of modern sensing technology for use in fields such as biochemical sensing, environmental monitoring, and medical science.

The use of high-Q resonant modes in THz metasurfaces has been widely explored in recent years [98][99]. Zhang *et al* investigated multiple symmetry protected quasi BIC mode in metallic metasurface for terahertz frequencies [100]. Our research builds upon these works by demonstrating a higher Q-factor through selective symmetry breaking, significantly advancing the field's understanding of loss control in THz metamaterials.

We introduces an approach to excite a quasi-bound State in the Continuum (quasi-BIC) mode with a high Q-factor in a THz metasurface by leveraging a selective symmetry-breaking technique. Unlike conventional methods that uniformly disrupt symmetry across all resonators, this approach perturbs only half of the unit cell, effectively reducing radiative losses and achieving Q-factors as high as 107 . This innovative technique may open new avenues for developing advanced THz devices, including sensors and optical filters, with superior performance metrics.

Other than the in-plane structural symmetry breaking approach of metasurface, some earlier works explored the high Q mode excitation through lattice mode coupling with the fundamental LC mode [114] and sharp Fano BIC mode[116]. Wang *et al.* explore the excitation of robust high Q BIC mode by lattice constant perturbation in a dielectric photonic crystal [43]. These studies laid the foundation for lattice-induced BIC excitation in terahertz metasurface. The lattice constant perturbation transforms modes below the light cone into quasi-BIC modes due to the folding of the modes from the band edge (see section 1.5.2 for details).

However, the excitation of stable toroidal quasi-BIC mode via the lattice perturbation-induced band folding mechanism in a simple metallic terahertz metasurface platform remains largely unexplored. *Our work presents a toroidal quasi BIC mode excitation by*

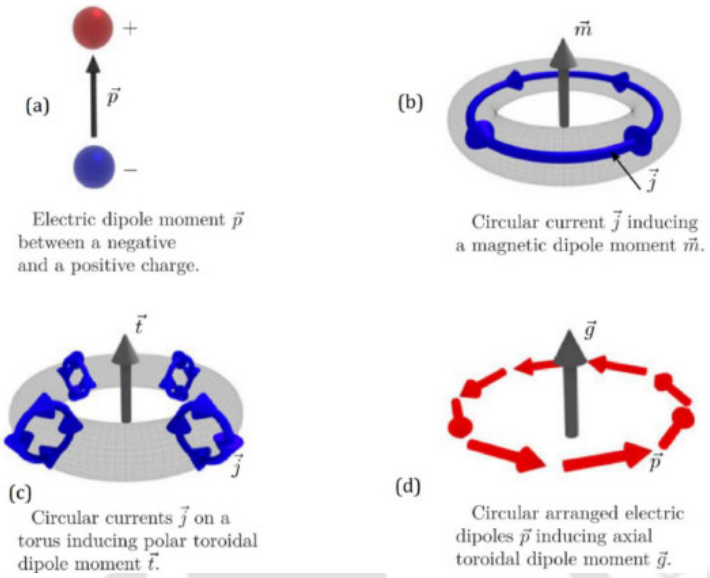

Figure 1.16: A pictorial representation of charge and current distributions creating (a) electric dipole, (b) magnetic dipole, (c) , (d) polar and axial toroidal dipole moments [64]

utilizing band folding mechanisms through lattice perturbation in a simple split ring resonator metasurface. The excited quasi-BIC mode exhibits stable, resonant frequency against perturbation, making it promising for applications such as high-precision optical sensors, terahertz imaging, etc. This innovative technique represents a significant step forward in developing advanced THz devices with stable spectral response.

1.5 Important concept related to the thesis

1.5.1 Toroidal resonance in metasurface

In the earlier theory of electromagnetism electric and magnetic moments were primarily considered as independent member of the multipole expansion. The toridal multipoles were completely missing from the standard multipolar expansion. In 1957, Y. Zel'dovich theoretically studied the violation of parity due to the weak interaction of elementary particles.. He predicted that Dirac particles with spin$-\frac{1}{2}$ must exhibit an "anapole moment," also referred to as a quantum toroidal dipole moment. In the 1970s, Dubovik and colleagues extended this idea to classical electrodynamics, introducing the concept of "polar toroidal moments." The term "toroidal" originates from the current distribution in circular loops, commonly referred to as toroid coils. The toroidal dipole moment is the first member of the toroidal multipole family, and it is further classified as an electric

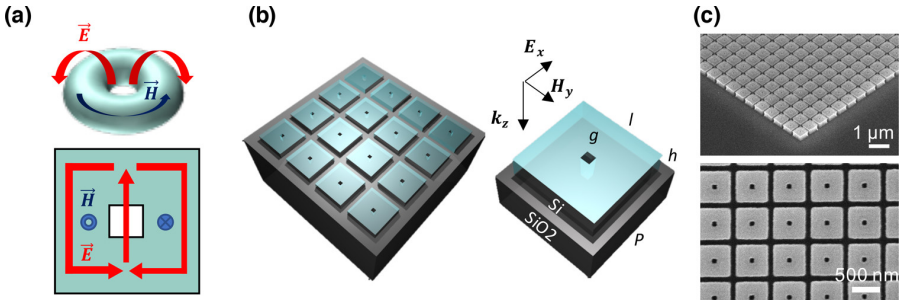

Figure 1.17: An all-dielectric metasurface design optimized for the excitation of toroidal resonance. (a) Top: a visual representation of solenoid electric fields (red arrows) inducing a toroidal magnetic field (blue arrow) in a torus. Bottom: A cuboid resonator and the excitation of toroidal resonance due to head to tail magnetic dipole arrangement. (b) the metasurface array and the constituent "meta atom." (c) SEM images of the fabricated sample. Adapted with permission from [60].

toroidal dipole moment and a magnetic toroidal dipole moment. Figure1.16 depicts a pictorial presentation of electric dipole (Fig 1.16(a)), magnetic dipole (Fig 1.16(b)) and toroidal dipole moments (Fig 1.16(c)) in terms of charge and current distributions. Fig 1.16 (c) shows the current loops formed in the arm of torous, such current loops are termed as "poloidal currents". The resultant magnetic dipoles form a head-to-tail arrangement. Such a head-to-tail arrangement of the magnetic dipole generates a polar toroidal dipole moment along the axis of the torus. Fig 1.16 (d) closed loop head-to-tail circulation of electric dipole moments. The resultant of such circular arranged axial toroidal dipole along the axis of symmetry. The toroidal excitation was explored in several all-dielectric metasurface [60] [74] and metallic SRR-type metasurface designs. The ease of fabrication and simple simulation were the primary reason for shifting the toroidal excitation platform from 3D metamaterial to planar 2D metasurfaces. Figure 1.17 shows a simple hollow cuboid all-dielectric metasurface design supporting a toroidal resonance mode [60]. In the hollow cuboid structure, the solenoidal electric field flows in-plane along the rectangular path with the toroidal magnetic field circulating out-of-plane around the center void, as shown in Fig. 1.17 (a). Sharp toroidal dipolar resonance has also been investigated in planar terahertz SRR metamaterials [62] [63]. Figure 1.18 (a) depicts the metasurface geometry and an artistic presentation of the excited toroidal modes. Figure 1.18 (b) shows the transmission spectrum of the metasurface at different split gap positions. The Q factor, as well as the resonance strength of the sharp toroidal mode, can be optimized by varying the slit gap position 'd'. Figure 1.18(c) shows the simulated surface current and magnetic field (H_z) profile at the sharp resonance frequency for

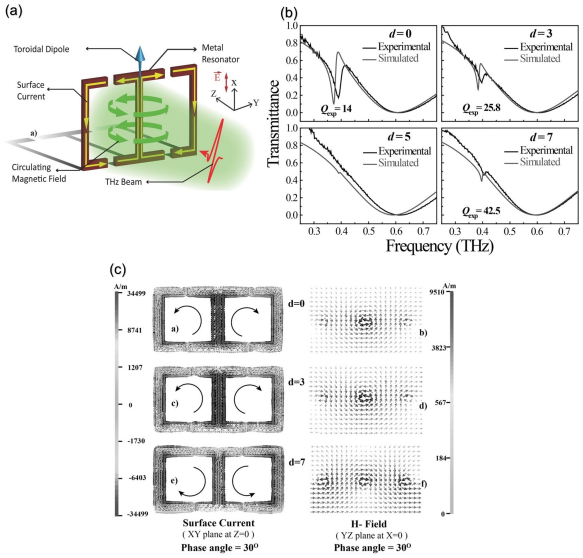

Figure 1.18: (a) Visual representation of the toroidal excitation in the metasurface geometry, (b) Experimental and simulated transmission for different split gap position "d". (c) the surface current plot and H_z plot at different sharp resonance frequencies corresponding to different split gap positions [62].

different values of 'd'. Two co-planar current loops with counter-propagating currents will generate a head-to-tail arrangement of magnetic dipoles, thereby forming a toroidal dipole.

1.5.2 Excitation of BIC using Brillouin zone folding mechanism in photonics

In photonics the fundamental modes supported by a photonic crystal, located below the light cone can be folded into the Γ by perturbing the lattice constant of the photonic crystal. In the work by Wang et al. [43], it is shown doubling the periodicity of a Silicon photonic crystal forms robust BIC modes. The first Brillouin zone is reduced by half due to the doubling of the periodicity. As a result of this, the X point of the unperturbed PhC is folded into Γ point, bringing the guided modes,X into the radiation continuum . This mechanism provides a alternative approach for engineering BICs periodic photonic structures such as photonic crystals and metasurfaces. Figure1.19 illustrate the conceptual idea of band folding mechanism in a photonic crystal as reported in [43]. Figure1.19(b) shows the terahertz photonic crystal slabs, with gap and radius perturbation, which leads to doubling of the periodicity. Figure1.19 (c) depicts the band structure for perturbed and

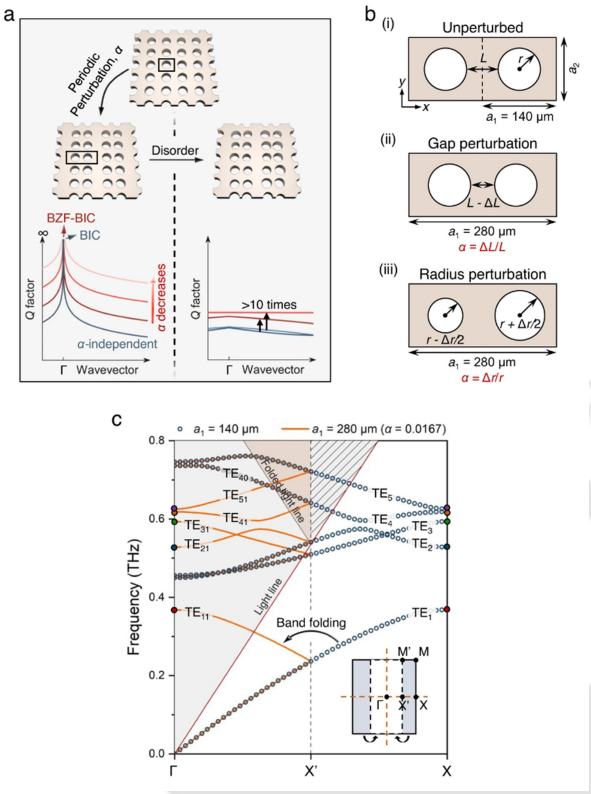

Figure 1.19: (a) Conceptual diagram of BZF-BICs. After introducing periodic perturbation, the unit cell peridocity doubles, and guided modes (GM) are transformed into BZF-BICs. Unlike ordinary BICs, the Q factor of BZF-BICs remains robust against disorder. (b) Schematic of terahertz photonic crystal (THz-PhC) slabs: **i)** unperturbed, **ii)** with gap perturbation where the distance between adjacent air holes changes by ΔL, and **iii)** with radius perturbation where the radius of air holes changes by Δr, both these perturbation leads to doubling of periodicity in the x-direction. (c) Calculated transverse electric (TE) band structures of unperturbed and gap-perturbed PhCs ($\alpha = 0.0167$, $\Delta L = 1$ μm), showing band folding at the Γ point. The original first Brillouin zone (FBZ) reduces by half [43].

unperturbed case. The modes are folded at the edge of the band (at X point).

1.6 Organization of the Thesis

This thesis explores the excitation of quasi-bound states in the continuum (quasi-BIC) resonance modes in terahertz metasurfaces and investigates the application of symmetry-protected quasi-BIC modes in the near-infrared (IR) region as ultra-narrow bandpass filter and dual parametric sensors. The content is organized into seven chapters, each providing a detailed analysis of different aspects of quasi-BIC modes and their practical applications. A summary of each chapter is provided below:

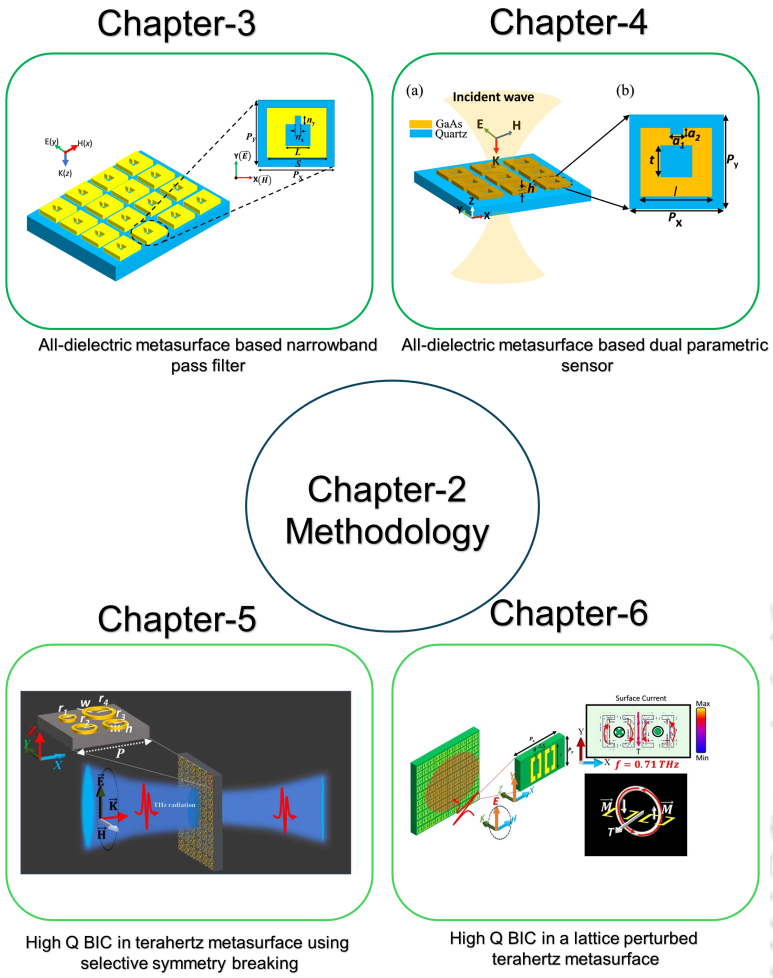

Figure 1.20: Organization of the thesis content.

Chapter 1 presents an overview of the fundamental concept of bound states in the continuum (BIC), an introduction to planar metasurfaces, and the mechanisms for exciting quasi-BIC modes in such structures. It further explores the concept of Fano resonance, its origin, and the connection between Fano resonance and BIC.

Chapter 2 discusses the methodology for the thesis. It deals with the design and optimization of the planar metasurfaces using CST simulation software and the fabrication of the design using photolithography. This chapter ended with a discussion about the characterization method using a terahertz time-domain spectroscope. In Chapter 3, we demonstrated an ultranarrow bandpass filter of pass band less than 3 nm in the optical communication wavelength 1550 nm and studied the physical mechanisms involved using multipolar decomposition and classical Fano theory.

Chapter 4 discusses an all-dielectric metasurface-based refractive index and temperature sensor exploiting the asymmetry-induced sharp Fano resonance mode.

In Chapter 5, we discussed the excitation of high Q quasi-BIC mode by reducing the radiative loss via a selective symmetry-breaking approach. The experimental and theoretical results are supported by an *ab initio* Fano theory.

In Chapter 6, we discuss our investigation of the lattice-induced quasi-BIC mode in a symmetric split ring resonator metasurface by doubling the lattice constant. We have experimentally demonstrated a signature response of the existing quasi-BIC mode. The coupled harmonic oscillator model and *ab initio* Fano theory have been used for an in-depth understanding of the mechanism.

Finally, in Chapter 7, we conclude our thesis with an emphasis on the findings and the future work that could be done based on the findings in this thesis.

CHAPTER 2

METHODOLOGY

This chapter presents an overview of the simulation method used to analyze metasurface, clean room fabrication techniques, and characterization techniques for the terahertz metasurface samples. Section 2.1 gives a detailed explanation of the simulation methods in CST microwave studio suite software. Section 2.2 briefly overviews the processes involved in fabricating the metasurface samples. Section 2.3 describes the terahertz time-domain spectroscopy involved in characterizing the metasurface samples.

2.1 Design through numerical simulation

Design of metamaterial structure is carried out using software based on rigorous Maxwell's equation solver. The finite-difference-time-domain method, Finite Integration Technique (FIT), and the Finite-Element Method (FEM) are some numerical approaches used to solve Maxwell's equations for metamaterial design. We used commercially available CST microwave studio suite simulation software. CST can quickly provide the S-parameter, reflectance, transmittance spectra, and electric and magnetic field distributions of a metamaterial design. The CST simulation software solves Maxwell's equations for a given medium under a defined boundary condition. Time domain solver and frequency domain solver are the two most frequently used solvers for 3D electromagnetic simulation. The time domain solver in CST is based on the Finite Integration Technique (FIT). FIT discretizes the following integral form of Maxwell's equations rather than the

differential one:

$$\int_{\partial A} \mathbf{E} \cdot d\mathbf{s} = -\frac{\partial}{\partial t} \int_A \mathbf{B} \cdot d\mathbf{A}, \quad \int_{\partial A} \mathbf{H} \cdot d\mathbf{s} = \int_A \left(\mathbf{J}_v + \frac{\partial \mathbf{D}}{\partial t} \right) \cdot d\mathbf{A},$$

$$\int_{\partial V} \mathbf{D} \cdot d\mathbf{A} = \int_V \rho \, dV, \quad \int_{\partial V} \mathbf{B} \cdot d\mathbf{A} = 0.$$

On the other hand, the frequency domain solver is based on the finite element method. The time domain solver calculates the field at discrete positions and discrete-time samples. The time domain solver can calculate the broadband frequency response of a device through a single calculation run. Afterward, the frequency response of the design is obtained by using the Fast Fourier Transform. In addition, the time domain solver can provide arbitrary fine resolution of the frequency spectrum without additional effort. Hence, this type of solver is suitable for simulated electrically large structures. For structures with dimensions smaller than the minimum wavelength, the use of a time domain solver is less efficient. For such structures, the frequency domain solver is the most efficient. This type of solver performs simulation at discrete frequencies separated by a specified frequency step. So, the frequency domain solver is suitable for the simulation of narrowband and electrically small structures.

After choosing the solver, the next important step is to generate a fine appropriate meshing. To solve Maxwell's equations, the computational volume is divided into smaller domains known as mesh cells. The sizes and number of the mesh cells determine the accuracy and resolution of the results. Each mesh cell represents a small volume where electric and magnetic fields are calculated; for a frequency domain solver, tetrahedron meshing is used. The time domain solver uses hexahedral meshing. In a time-domain solver, the excitation pulse is a time-domain signal (usually a Gaussian pulse). The signal propagates through the computational volume. So, the faster the signal propagates through the volume, the faster the simulation. The time step determines the speed of the signal, as the fields are advanced in time by one specified time step in every iteration. It seems that for the simulation time to be faster, a larger time step is advantageous (as it will take less run time). However, the maximum time step is constrained by the Courant stability condition [44]:

$$\Delta t_{\max} \leq \left(\frac{1}{u_{\max} \left(\left(\frac{1}{\Delta x}\right)^2 + \left(\frac{1}{\Delta y}\right)^2 + \left(\frac{1}{\Delta z}\right)^2 \right)} \right)^{-1/2}$$

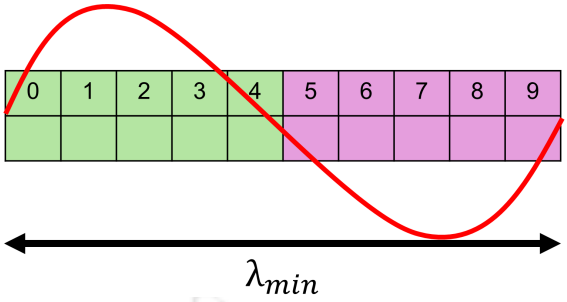

Figure 2.1: To ensure that the simulation is accurate across all frequencies of interest, the mesh needs to be fine enough to accurately represent the shortest wavelength in the simulation (at least 10 meshes cells per wavelength) .

here, $\Delta x, \Delta y, \Delta z$ are the side lengths of a mesh cell, and $u_{\max}$ is the maximum wave phase velocity. For a uniform cuboid mesh cell $\Delta x = \Delta y = \Delta z = \Delta l$ (say), and hence:

$$\Delta t_{\max} \leq \frac{\Delta l}{\sqrt{3}\, u_{\max}}$$

i.e., the shortest edge of the mesh cell determines the maximum allowed time steps. Thus, for smaller mesh cells, the time step will be smaller, and the simulation will take longer. However, to achieve accurate results, the minimum feature size of the model should be finely meshed. Therefore, there is a trade-off between accuracy and simulation time. To maximize the time step, the smallest mesh cell should be as large as possible. However, the size of the mesh cells is constrained by the requirement to accurately represent small features in critical areas of the model where fine sampling of the field is important.

Conversely, larger mesh cells can improve simulation speed by reducing the total number of cells, thereby lowering computational time. However, the size of the mesh cells cannot be increased arbitrarily due to numerical dispersion, where different frequency components propagate at slightly different velocities in the mesh due to space discretization. To minimize this effect and ensure accurate representation across all wavelengths, the shortest wavelength of interest must be sampled at a rate of at least 10 mesh cells per wavelength. This limits the mesh cells' larger size, as it must be small enough to sample the shortest wavelength (as shown in Fig2.1). Therefore, while larger mesh cells can speed up simulations, they are constrained by the need to minimize numerical dispersion and maintain accuracy, achieving a balance between efficiency and precision.

In contrast, when using the frequency domain solver, simulations are carried out at each frequency, separated by a specified frequency step to cover the entire operating

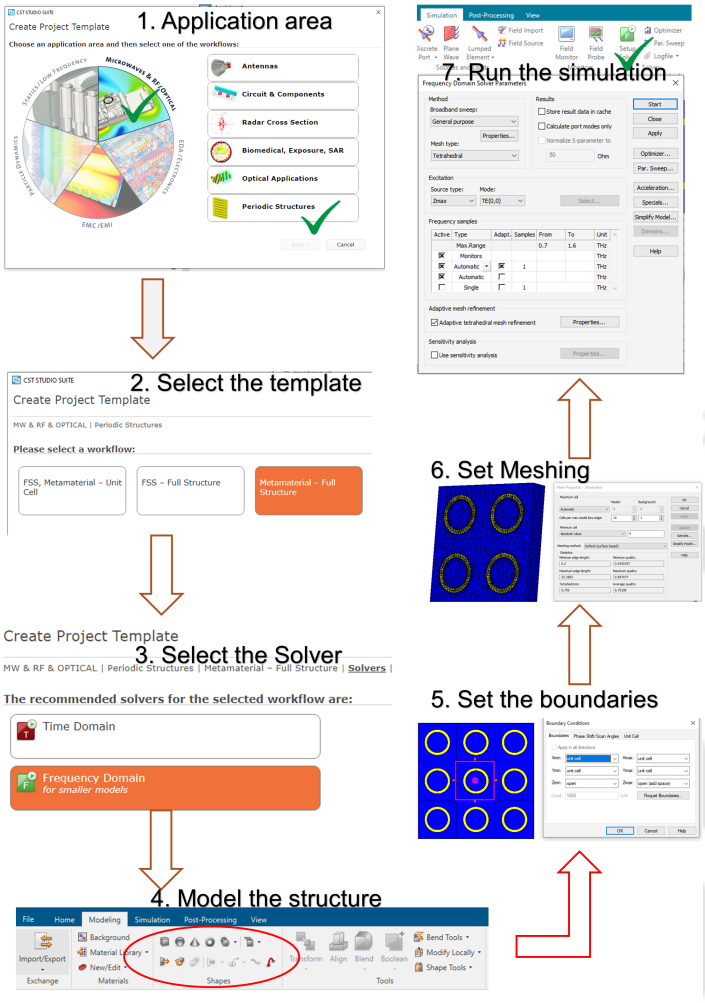

Figure 2.2: Workflow of the metamaterial in CST Studio suite software.

bandwidth. This approach allows for adaptive mesh refinement at each frequency to achieve accuracy. The simulation continues until the S-parameters converge, and a single run can provide results for all ports in one calculation. In the frequency domain solver Maxwell's integral equations are Fourier transformed, and Fourier equivalent of the time derivative operator is used $\frac{\partial}{\partial t} \rightarrow i\omega$

CST provides a CAD environment to design a metamaterial unit cell. After designing the 'unit cell,' the next step is to set the frequency range and appropriate boundary conditions. Figure 2.2 shows the flowchart of the simulation procedure to design metamaterial in CST studio suite software. For a frequency domain solver, boundary conditions are set as unit cells in the XY plane to efficiently model a periodic metamaterial array. In the Z direction, the boundary condition is set as 'Open,' which represents the direction of

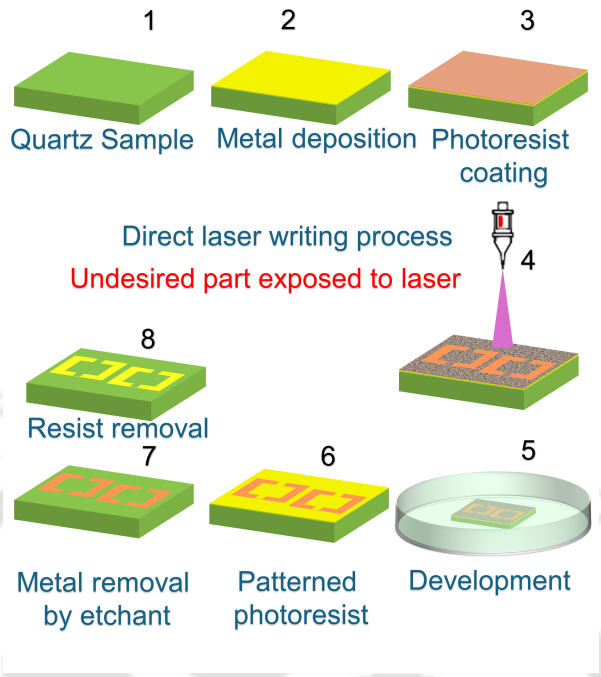

Figure 2.3: Visual representation of the various steps involved in the fabrication of the metasurface sample.

propagation. To minimize the effect of the fringing field in the calculation, it is necessary to apply an 'add space' along Zmax(+Z). In CST, a $\lambda_{central}/4$ gap is added by default for the 'open (add space)' boundary condition.

2.2 Clean room fabrication

The resonant behaviour of the metamaterial is the collective response of the array of unit cells. This section provides a description of the involved photo-lithography process to fabricate the design. Initially, the quartz sample was thoroughly cleaned using acetone, isopropyl alcohol (IPA), and distilled or deionized (DI) water to eliminate any impurities. Subsequently, the sample was dried using N_2 gas and heated at 100 °C for 10 minutes using a hot plate to ensure complete moisture removal. A 200 nm thick layer of aluminum metal was then deposited onto the clean substrate using a thermal evaporator. The thickness of the metal was chosen to be higher than the skin depth of the metal in the terahertz range, so as to avoid partial transmission from the resonators.

To enhance the adhesion of the photoresist to the substrate, a coating of hexamethyldisilazane (HMDS) was applied at a rotational speed of 3500 RPM for 60 seconds,

followed by heating the sample at 150 °C for 30 minutes to facilitate optimal bonding. The pre-coated substrate was further coated with a positive photoresist (S1813) of thickness 1.3 μm, by spinning the sample at 3000 RPM for 60 seconds. Subsequently, the photoresist-coated substrate underwent a 2-minute baking process at 100 °C to promote uniformity and stability.

A complementary pattern has been generated by a direct laser mask writer (Dilase 250). This step determines the area of the metasurface to be selectively masked and the area to be etched out. After development for 50 s, the undesired metallic part was removed from the sample by using aluminum etchant (2- 3 minutes). The photoresist-coated area served as a protective mask for metallic regions intended to be part of the final metasurface structure. Finally, acetone is used to strip away the residual photoresist.

The sample underwent thorough cleaning with acetone and DI water after the fabrication process, followed by drying using N_2 gas. Final drying was achieved by heating the sample for 5 minutes at 100 °C to ensure complete removal of any residual moisture. The fabricated samples consisted of periodic arrays of designed metamaterials prepared on a 1 cm × 1 cm region. Figure 2.3 presents an overview of the various steps involved in the fabrication of the metasurface sample.

2.3 Characterization of the sample

For the characterization of the metasurface samples, we used the terahertz time-domain spectroscopy method. The terahertz time-domain spectroscopy (THz-TDS) provides direct measurement of both the amplitude and phase of the electric field of a terahertz pulse as it passes through a sample. This allows for direct determination of material properties such as complex conductivity, complex refractive index, and complex permittivity. We used a home-built terahertz time-domain setup as well as a fiber-coupled inbuilt commercial terahertz time-domain setup to characterize the samples. Before discussing the working process of terahertz time domain setup, it is important to discuss the generation and detection process of terahertz. Terahertz radiation can be generated and detected through various methods. In this thesis we will mainly focus on the THz-TDS setup using photoconductive antennas and nonlinear crystals for the generation and detection of terahertz pulses.

2.3.1 Generation of terahertz from photo conductive antenna

There exists a large number of THz emitters and detectors. Among these, photoconducitve antennas (PCAs) are popular and widely used in terahertz generation process. This popularity is due to its simplicity, ease of use, reliability, and relatively low cost. A photoconductive antenna comprises of two metal contacts lithographically fabricated on a semiconductor substrate. The two metal electrodes are biased with a DC voltage and an optical fs pulse is made to incident on the gap between the two electrodes. Fig 2.4 shows a schematic of LT GaAs based Bow-tie photoconductive antenna. The radiation is collimated using the Silicon lens. The refractive index of silicon nearly matches with the substrate material and hence it causes minimal reflection loss. The basic principle of terahertz generation using PCA is based on the principle that *an accelerating charge particle generates electromagnetic radiation*. In case of a dipole antenna which is much smaller than the emitted wvalength and having a diameter W_0, the THz field at a distance r and angle α is given by [45]

$$E_{\mathrm{THz}}(t) \propto W_0 \left(\frac{\sin(\alpha)}{r}\right) \frac{d|I_{\mathrm{PC}}(t_r)|}{dt} \tag{2.1}$$

where: $t_r = t - \frac{r}{c}$ is the retarded time, and $I_{\mathrm{PC}}(t)$ is the transient photocurrent. The semiconductor substrate material is undoped and, therefore, has high resistivity. The metal contacts act as a capacitor with stored electrostatic energy

$$W(t) = \frac{1}{2} C U_{\mathrm{DC}}^2(t) \tag{2.2}$$

The ultra-fast fs laser pulse is focused on the gap between the electrodes, as shown in Fig 2.5(a). The photon energy of the pulse must be greater than the energy band gap of the semiconductor.

2.3.2 Terahertz time-domain spectroscopy

A spectroscopic technique refers to the measurement of energy, intensity of photon with respect to its frequency or wavelength when it passes through a sample. The THz time-domain spectroscopy is different from, in general, other spectroscopic techniques like traditional Fourier-transform infrared spectroscopy (FTIR), as it directly measures the electric field rather than the intensity.

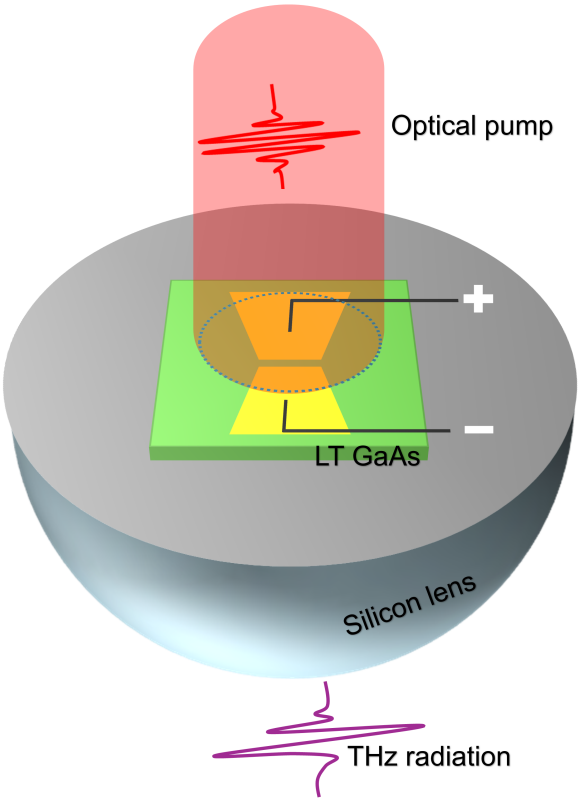

Figure 2.4: A schematic representation of the THz generation from LT GaAs based photoconductive antenna (PCA), the incoming optical pulse excites photo carriers, and the acceleration of the charges generate THz radiation. A hyper-hemispherical Si lens is used to collimate the terahertz radiation.

A typical THz signal has a subpicosecond time duration [48]. The traditional electronics based circuits and detectors does not have enough time resolution to detect such signals as their rise and fall time lies within ns or ps range. So this time domain spectroscopy technique is used to resolve subpicosecond duration signal by splitting a NIR ultrashort fs pulse along two different paths to generate and detect the temporal THz field as discussed below.

In time domain spectroscopy measurement is based on the sampling of the unknown THz field in time domain with a known fs laser pulse. THz TDS uses the convolution of the fs laser pulse with comparatively longer THz pulse. The in general method of convolution, without discussing the mechanism of detection can be described as [48],

$$F(t) \propto I_{\text{opt}}(t) E_{\text{THz}}(t) \tag{2.3}$$

,where F(t) is the signal and $I_{opt}(t)$ is the intensity profile of the laser pulse and E_{THz} (t),

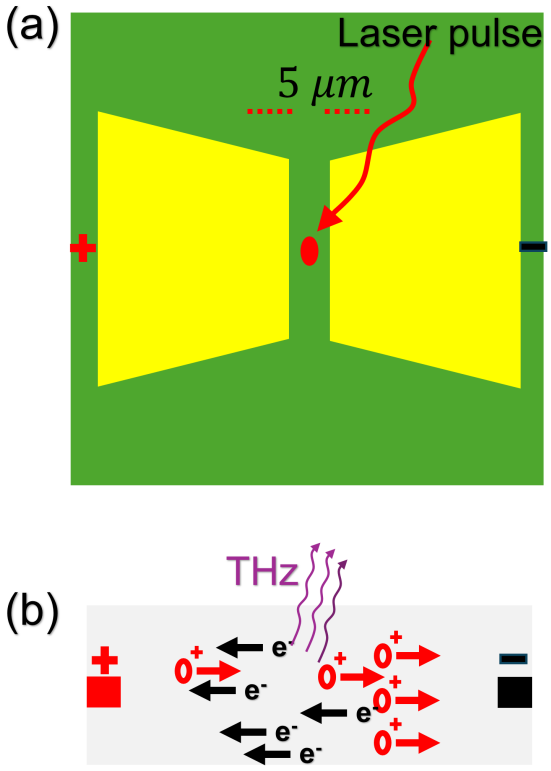

Figure 2.5: (a) Schematic of a PCA, the laser beam is focused on the gap, (b) the laser pulse generates charge carriers and accelerated due to the biasing voltage.

the terahertz elctric field at time 't'. The optical pulse (which is typically much shorter than the THz pulse) serves as a "probe" to sample the THz signal. However, no detector have such fast response time to measure this instantaneous interaction. The resulting signal is expressed as convolution of the two signals, which actually represents how the two pulses (optical and THz) overlap over time,

$$F(t_1) = (I_{\text{opt}} * E_{\text{THz}})(t_1) = \int_{-\infty}^{\infty} I_{\text{opt}}(t_1 - \tau) E_{\text{THz}}(\tau)\, d\tau \tag{2.4}$$

Since the optical pulse is much shorter than the THz pulse, it can be considered as a delta function. This simplifies the convolution to the point where we approximate the measured signal as being proportional to the THz field at each time point.

$$F(t_1) \propto \delta(t) * E_{\text{THz}}(t_1) = E_{\text{THz}}(t_1) \tag{2.5}$$

This implies that the detection process is sensitive only when the two pulses arrive simultaneously and the optical pulse is significantly smaller than the THz pulse. This allows to measure the THz field as a function of time.

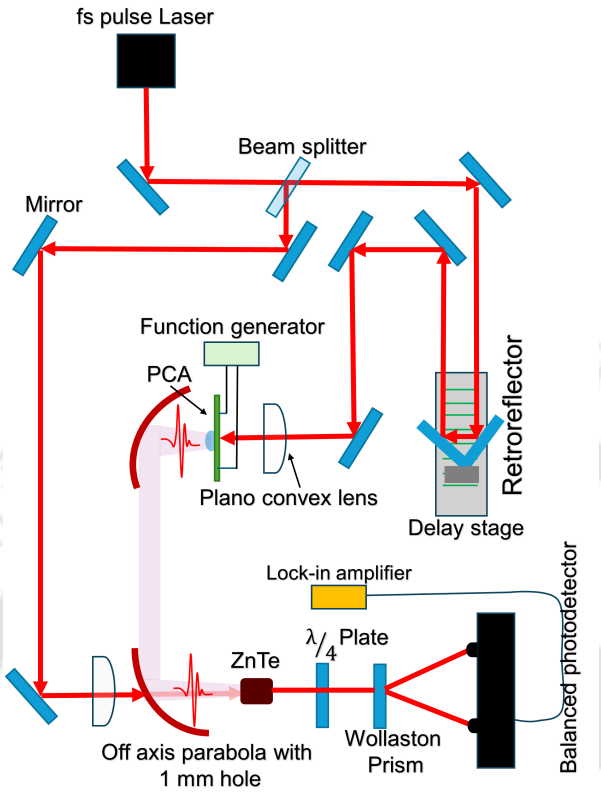

Figure 2.6: The photoconductive antenna based terahertz time domain setup, where a PCA used for the generation of terahertz and ZnTe crystal is used as a terahertz detector.

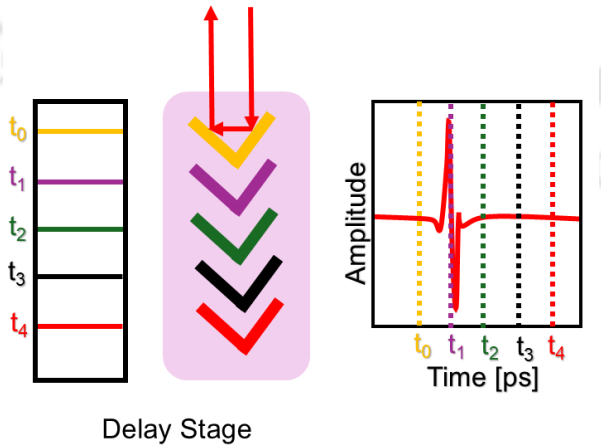

Figure 2.7: A visual illustration of the function of delay stage. the different colour lines correspond to different position of the stage. These positions correspond to different time in the time axis.

The measured signal gives the THz electric field at time t_1; now, to measure the signal all over the time, a mechanical delay line is introduced between the probe (read out pulse) and the THz field (as shown in Fig 2.6). Fig 2.6 depicts a schematic representation of the THz time-domain setup. An ultrafast femtosecond pulse of wavelength 780 nm, with a repetition rate of 100 MHz, is splitted into two parts from the beam splitter. With the help of the mirrors, one part of the beam (pump beam) is guided to the photoconductive antenna (emitter) for terahertz generation, and the second part (probe beam) is guided to the ZnTe crystal (detector) for terahertz detection. The emitter part of the photoconductive antenna consists of two parallel metallic electrodes on a low-temperature GaAs substrate with a small gap of 5 μm. For the generation of the terahertz pulse, a DC voltage of 10 V (peak to peak) is applied across the electrodes using a function generator, and the substrate area between the electrodes is irradiated by an ultrafast optical pulse. The pump beam passes through a mechanical delay stage, which is introduced to sample the THz signal as a function of delay time. Figure 2.7 presents the detailed function of the delay stage movement in sampling the THz electric field. The temporal sampling interval of the detected THz pulse can be calculated by $\Delta t = 2S/c$, where S is the movement of the delay stage in each step, and c is the speed of light ($300\mu m/S$). The precise micro-positioning is achieved through the Lab view program. The speed of the delay line movement defines the sampling speed of the time domain setup. The terahertz detection using ZnTe crystal is based on the electro-optic Pockels effect. Since the probe pulse is much shorter than the generated THz pulse, the optical pulse experiences a consistent electric field when both pulses reach the crystal simultaneously. The static electric field responsible for the field-induced birefringence in the Pockels effect is the THz pulse. By varying the temporal overlapping the probe beam samples different electric fields. After passing through the crystal, the optical beam passes through two elements: a quarter-wave ($\lambda/4$) plate and a Wollaston prism. The $\lambda/4$ plate introduces a phase shift of $\Delta\phi = \pi/2$ between the orthogonal o-ray and e-ray components of the wave, converting linear polarization into elliptical or circular polarization when incident polarization is 45° to the principal axis. It is converted into circularly polarized light due to the 90° phase shift. The Wollaston prism splits the incoming light into two orthogonal linearly polarized beams. In the absence of a THz pulse, there is no electro-optic effect. The linearly polarized optical pulse remains unaffected by the crystal, converting into circular polarization after the $\lambda/4$ plate. The Wollaston prism splits this into two equal-intensity beams, which are sent to the balance photodetectors. In the presence of a THz

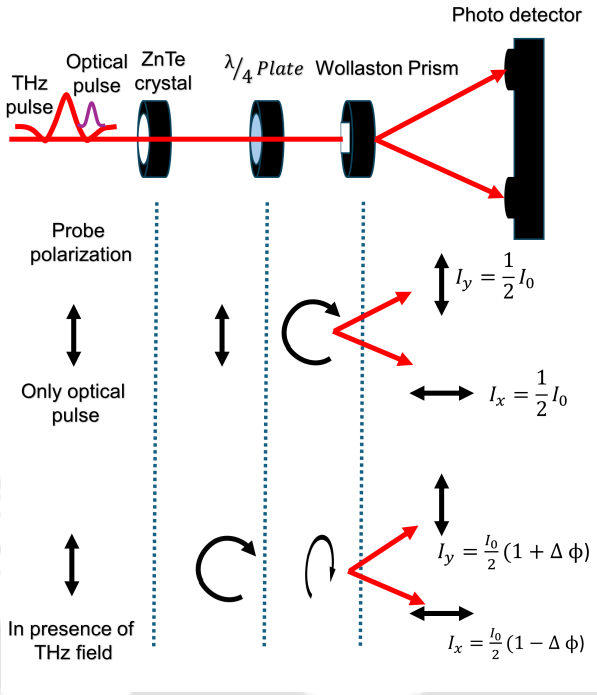

Figure 2.8: Electro-optical detection method using a ZnTe crystal. Dependency of the polarization state of the optical probe beam without and in the presence of THz field.

pulse, the anisotropic birefringence effect in the ZnTe crystal causes the probe pulse to become slightly elliptical after passing through the $\lambda/4$ plate, leading to an imbalance between the two orthogonal beams. The measured signal is the difference in intensities, $I_s = I_y - I_x$, which is proportional to the amplitude of the applied THz field. Figure2.8 shows a pictorial illustration of the detection process using ZnTe crystal. In the presence of the THz field (polarized 45° to X-axis), the refractive index along x and y changes according to the following equations:

$$n_x = n_0 + \frac{1}{2}(n_0)^3 R E_{\mathrm{THz}} \tag{2.6}$$

$$n_y = n_0 - \frac{1}{2}(n_0)^3 R E_{\mathrm{THz}} \tag{2.7}$$

,where n_0 is the refractive index without THz electric field, R is the electro-optic constant and E_{THz} is the electric field of the terahertz radiation. The phase difference experienced by the probe beam due to the Pockel's effect after a propagation length 'd' is given as,

$$\Delta\phi = (n_x - n_y)kd = (n_0)^3 R E_{\mathrm{THz}} \frac{\omega d}{c} \tag{2.8}$$

The change in phase difference is proportional to the THz electric field. The intensity of the two orthogonal polarized beams can be given as,

$$I_x = \frac{I_0}{2}\left(1 - \Delta\phi\right) \tag{2.9}$$

$$I_y = \frac{I_0}{2}\left(1 + \Delta\phi\right) \tag{2.10}$$

, the difference between the intensities of the two orthogonal components is proportional to the THz field amplitude. The photodetector measures this imbalance, and the differential current is amplified and converted into a voltage signal by a preamplifier. Voltage signals are recorded using a Lock-in amplifier to reduce the signal-to-noise ratio.

CHAPTER 3

ALL-DIELECTRIC METASURFACE BASED ULTRA NARROW BAND PASS FILTER USING SYMMETRY BREAKING APPROACH

3.1 Introduction

In the field of optical communication and sensing, there is a growing demand for metasurface based components such as filters, modulators etc, particularly within the C-band wavelength range (1530–1565 nm). Narrow bandpass filters are crucial for various applications such as spectral imaging [49] , efficient displays[50], and light detection and ranging[39],etc. A high reflectance or transmittance and narrow full width at half maximum (FWHM) are the key metrics of an efficient narrow band pass filter. Moreover, a low side band or known as "quiet zone," is essential for ensuring optimal filter performance.

In this chapter, we have demonstrated an all-dielectric metasurface-based ultranarrow bandpass filter operating within the C-band wavelength range (1530–1565 nm). By using a symmetry-breaking approach, we excite quasi-bound states in the continuum (quasi-BICs). We achieve a Full Width at Half Maximum (FWHM) of 0.31 nm at a center wavelength of 1549.8 nm, with a corresponding high Q-factor of approximately 5140. The

Part of the results of this Chapter have been published in the following papers: Bhairov Kumar Bhowmik, Tanmay Bhowmik, Pranav Kumar Pandey, Makaraju Srinivasa Raju, Debabrata Sikdar, and Gagan Kumar, "All-dielectric metasurface based ultranarrow bandpass filter in optical C-band," J. Opt. Soc. Am. B 40, 1311-1318 (2023)

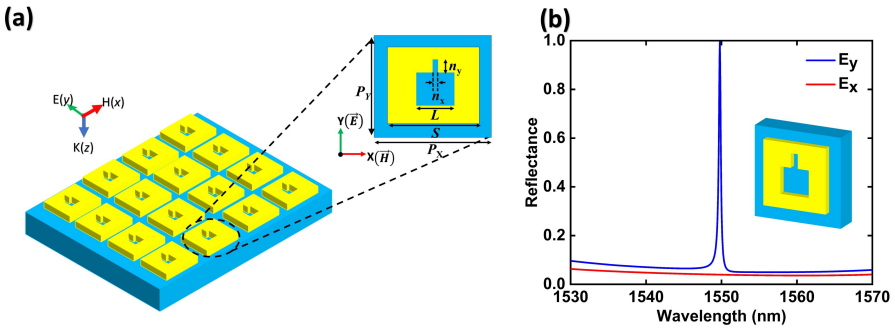

Figure 3.1: (a) Periodic configuration of the metasurface design on a quartz substrate. Inset shows a zoomed-in view of the top surface of a metasurface unit cell. The yellow-colored material layer represents a block of GaAs with periodicity $P_x = P_y = 760$ nm and a thickness $h = 314$ nm. The side length of the GaAs square block is $S = 680$ nm, the larger square air hole has a side length $L = 290$ nm, and the smaller rectangular air hole has a side length $n_x = 40$ nm and width $n_y = 120$ nm. The depth of the holes is equal to the thickness of the GaAs layer. (b) Reflectance spectrum for the design with asymmetry due to the addition of the notch, for two orthogonal polarizations of the incident electromagnetic wave.

sharpness of this Fano resonance arises from the breaking of structural symmetry in the metasurface. The Q factor of the resonance mode shows an inverse square relation with the asymmetry parameter α: $Q = Q_0 \alpha^{-2} + C$

To further understand the behavior of the resonances, we employ multipolar decomposition, revealing that the resonance is dominated by electric quadrupolar modes, which contribute to the narrow line width and high Q-factor. The filtering response shows passive tunability in the entire C band region while the line width remains almost constant. The chapter is organized as follows: Section 3.2 outlines the design and simulation details of the metasurface. Section 3.3 gives an analysis of the metasurface's spectral response, while Section 3.4 discusses the evolution of the BIC to the quasi-BIC mode. Section 3.5 presents an analysis based on the multipolar decomposition theory, and Section 3.6 describes a parametric study. Finally, Section 3.7 concludes the chapter with a summary of the major findings.

3.2 Design and modeling

The schematic of the proposed design is shown in Fig. 3.1(a). The proposed tunable filter consists of a 2D periodic array of gallium arsenide (GaAs) blocks with square air holes placed on top of a quartz substrate. A symmetry-breaking defect (notch) adjacent to the square air hole is introduced, as shown by the zoomed view of a unit cell in the

inset of Fig. 3.1(a). We used CST Studio Suite software, a commercially available finite integration technique-based software, to design and simulate the results. We considered a y-polarized (TE-polarized) incident electromagnetic wave propagating along the z-direction. The boundary conditions are chosen as unit cells in the x and y directions; along the z-axis, perfectly matched layer (PML) boundary conditions are applied. In our simulation, we considered a homogeneous normal background with a permittivity of unity.

3.3 Analysis of the metasurface response

To elucidate the underlying mechanism of the Fano line shape resonance, we present a systematic study of the resonance and its electric field profile. Figure 3.2(a) shows the simulated reflectance spectrum for normal incident excitation with a y-polarized electromagnetic wave on a GaAs block with a square hole, without introducing a symmetry-breaking defect. We observed an almost flat response, with less than 20 % reflectance and more than 80 % transmittance in the entire C band, ensuring a minimal loss in this wavelength region. The design exhibited a sharp, narrow linewidth resonance upon introducing the symmetry-breaking defect.

The reflectance spectrum can be modeled by the following Fano formula [51]:

$$R(\omega) = \left| a_1 + ia_2 + \frac{b}{\omega - \omega_0 + i\gamma} \right|^2 \tag{3.1}$$

where a_1, a_2, and b are real constants, ω_0 is the resonance frequency, and γ is the damping rate.

Figure 3.2(b) shows the Fano line shape fitting of the reflectance spectrum with the simulation-based result for the design incorporating in-plane symmetry breaking. The Q-factor of the resonance was calculated using:

$$Q = \frac{\omega_0}{2\gamma} \tag{3.2}$$

which yields a value of approximately 5140 at the resonance wavelength of 1549.8 nm. To further understand the physical mechanism behind the resonance, we computed the normalized E_y component of the electric field distributions below and above the resonance wavelength, as shown in the inset of Fig. 3.2(b). The positive and negative charge distributions are indicated by the plus and minus signs, respectively. At these

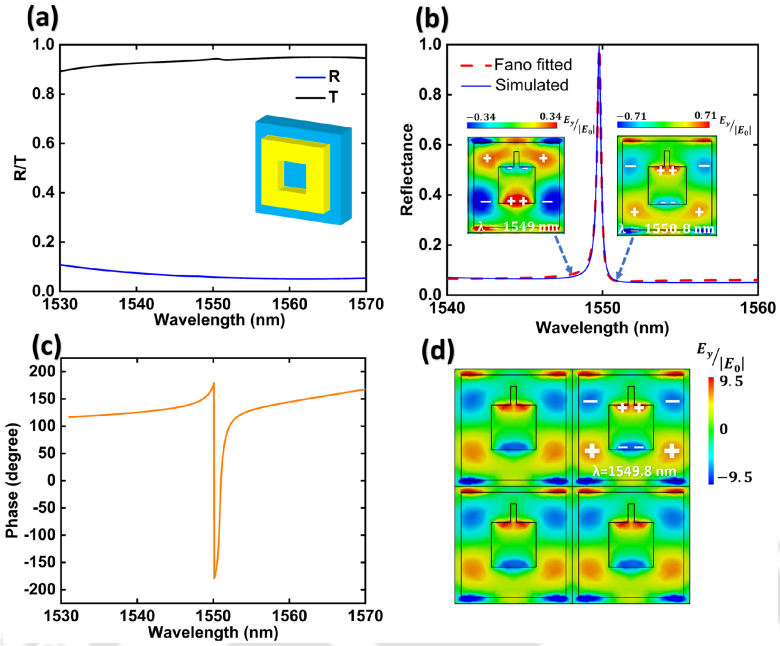

Figure 3.2: (a) The reflectance (R) and transmittance (T) for the resonator with a single square hole without any notch. Inset: The design. (b) Fitted data for the design with asymmetry using the Fano model, and the normalized field profiles (E_y component) show an anti-phase mode below and above the resonance wavelength. (c) Simulated phase spectra showing a change in phase at the resonance. (d) Simulated normalized electric field profile at the resonance wavelength of 1549.8 nm in the x-y plane. The field profile is calculated exactly on top of the substrate, revealing a coupled electric quadrupolar mode at the resonance wavelength.

frequencies, the fields are completely antiphase, resulting in destructive interference of the two modes, which leads to a sharp Fano line shape resonance at 1549.8 nm [52] [53]. Figure 3.2(c) illustrates the simulated phase spectrum for the design. The phase spectrum clearly shows a sharp phase change at the resonance wavelength, as corroborated by the inset in Fig. 3.2(b). Figure 3.2(d) presents the normalized y-component of the electric field distribution relative to the incident electric field ($E_y/|E_0|$) at the resonance wavelength in the xy-plane. The color map represents the strength of the electric field distribution, revealing a coupled quadrupolar mode at the resonance wavelength.

3.4 Evolution of the Quasi BIC mode

As described in the previous section bound states in the continuum (BICs) are localized states that exist within the range of radiation continuum states without coupling to free space [10]. These localized states, characterized by an infinite Q factor, become accessible

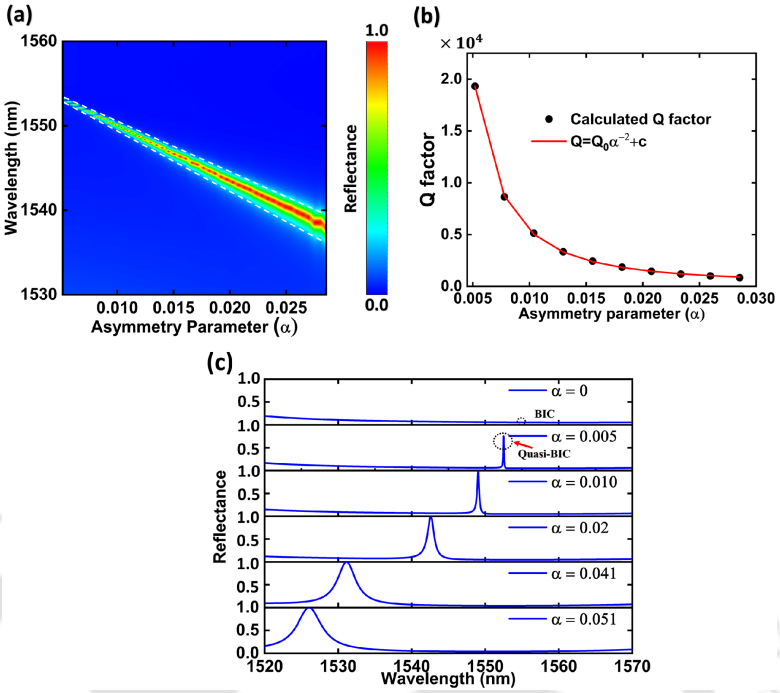

Figure 3.3: (a) Contour plot showing the dependence of FWHM and resonance wavelength on the degree of asymmetry. (b) Dependence of the Q factor with the asymmetry parameter of the design. Here, the solid line is a result of fit showing an inverse square variation with the asymmetry parameter, and C(=275.9) is a correction factor. (c) Evolution of the resonance mode with respect to the asymmetry parameter.

to free space excitation through the transformation of BICs into quasi-BICs. To perform an in-depth analysis of the influence of asymmetry, we define an asymmetry parameter $\alpha = \delta S/S$, where δS is the area of the notch, and S is the total area of the GaAs block. In our study, we varied the width of the notch (n_x) with respect to the center, while keeping the length of the notch (n_y) constant. The contour plot of the resonance effect as a function of the asymmetry parameter is shown in Fig. 3.3(a). As the asymmetry increased, the resonance wavelength shifted towards shorter wavelengths, and the Full Width at Half Maximum (FWHM) broadened. However, the reflectance amplitude remained constant throughout the parametric change. The notch provided an effective means to control the spectral position of the resonance and its FWHM. As reported in[54], the generation and annihilation of BICs can be governed by structural parameters. The Q factor is inversely proportional to the square of the asymmetry parameter [55] [5] . Figure 3.3(b) demonstrates a good fit of the calculated Q factor using the relation:

$$Q = Q_0 \alpha^{-2} + c \tag{3.3}$$

where c is a correction factor and Q_0 is a constant determined by the metasurface geometry. It is evident that smaller asymmetry values lead to higher Q factors for the resonance. Based on the theoretical analysis by Koshelev et al., it is believed that the resonance is governed by a symmetry-protected BIC-like mechanism [4] [72].

Figure 3.3(c) shows the evolution of the resonance mode in the reflectance spectrum with varying asymmetry parameters. As the asymmetry decreased, the resonance became sharper and eventually vanished at $\alpha = 0$. The absence of resonance indicates that no leaky modes coupled to free space, confirming the presence of a BIC-like nature due to symmetry. The sharp Fano mode observed in our analysis can be attributed to the quasi-BIC mode.

3.5 Exploring Mode Characteristics Through Multipolar Decomposition

We used the multipolar decomposition technique to investigate the contribution of the electric quadrupole moment at the resonance wavelength. For the multipolar analysis, we first extracted the electric field and effective refractive index corresponding to the Cartesian position coordinate and frequency of the metasurface using the FDTD simulation technique. The structural current density inside the unit cell can be calculated as [57] [58]

$$\mathbf{J}(\mathbf{r}) = -i\omega\varepsilon_0(n^2 - 1)\mathbf{E}(\mathbf{r}), \tag{3.4}$$

where $\mathbf{r}$ is the position vector and n is the effective refractive index of the resonator. The electric dipole (P_α), magnetic dipole (m_α), electric quadrupole moment ($Q^e_{\alpha\beta}$), and magnetic quadrupole moment ($Q^m_{\alpha\beta}$) can be expressed as[58]:

$$P_\alpha = -\frac{1}{i\omega}\left[\int j_\alpha j_0(k\mathbf{r})d^3\mathbf{r} + \frac{k^2}{2}\int \left(3(\mathbf{r}\cdot j)r_\alpha - r^2 j_\alpha\right)\frac{j_2(k\mathbf{r})}{(k\mathbf{r})^2}d^3\mathbf{r}\right], \tag{3.5}$$

The magnetic dipole moment (m_α), electric quadrupole moment ($Q^e_{\alpha\beta}$), and magnetic quadrupole moment ($Q^m_{\alpha\beta}$) are expressed as[58]:

$$m_\alpha = \frac{3}{2}\left[\int (\mathbf{r}\times\mathbf{J})_\alpha \frac{j_1(k\mathbf{r})}{kr}d^3\mathbf{r}\right], \tag{3.6}$$

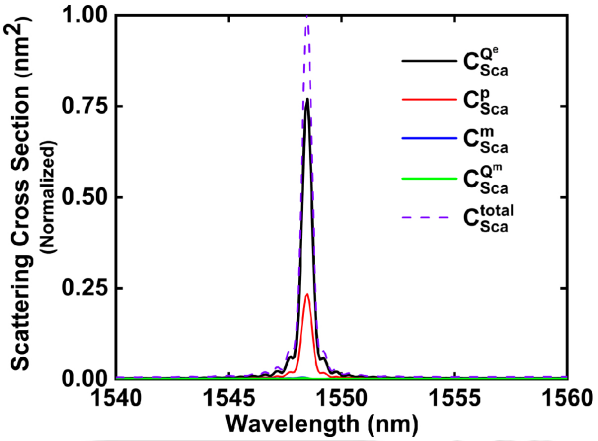

Figure 3.4: Multipolar analysis of the proposed metasurface design. $C_p^{\text{sca}}, C_m^{\text{sca}}, C_{Q^e}^{\text{sca}}, C_{Q^m}^{\text{sca}}, C_{\text{sca}}^{\text{total}}$ represent the scattering cross-sections for the resonator due to the electric dipole, magnetic dipole, electric quadrupole, magnetic quadrupole, and the total cross-section, respectively.

$$Q^e_{\alpha\beta} = -\frac{1}{i\omega}\left[\int \left(3\left(r_\beta J_\alpha + r_\alpha J_\beta\right) - 2(\mathbf{r}\cdot\mathbf{J})\delta_{\alpha\beta}\right)\frac{j_1(kr)}{kr}d^3\mathbf{r} + 2k^2\int\left(5r_\alpha r_\beta(\mathbf{r}\cdot\mathbf{J}) - r^2\left(r_\alpha J_\beta + r_\beta J_\alpha\right) - r^2(\mathbf{r}\cdot\mathbf{J})\delta_{\alpha\beta}\right)\frac{j_3(kr)}{(kr)^3}d^3\mathbf{r}\right] \tag{3.7}$$

$$Q^m_{\alpha\beta} = 15\left[\int\left(r_\alpha(\mathbf{r}\times\mathbf{J})_\beta + r_\beta(\mathbf{r}\times\mathbf{J})_\alpha\right)\frac{j_2(k\mathbf{r})}{(kr)^2}d^3\mathbf{r}\right], \tag{3.8}$$

where $\alpha,\beta = x,y,z$, and $j_n(kr)$ is the spherical Bessel function with $n = 0,1,2$, and k is the magnitude of the wave vector.

The total effective scattering cross-section ($C_{\text{sca}}^{\text{Total}}$) is given by the sum of the contributions from all the multipoles:

$$C_{\text{sca}}^{\text{Total}} = \frac{k^4}{6\pi\varepsilon_0^2|E_0|}\left[6\left(|P|^2 + \left|\frac{m}{c}\right|^2\right) + \frac{1}{120}\left(|Q^e|^2 + \left|\frac{kQ^m}{c}\right|^2\right) + \ldots\right], \tag{3.9}$$

where $|E_0|$ is the amplitude of the incident electric field, c is the speed of light in vacuum, and ε_0 is the permittivity of free space.

For our proposed design, the multipolar analysis is shown in Fig. 3.4 , where the electric quadrupolar mode has a larger contribution at the resonance wavelength of 1549.8 nm.

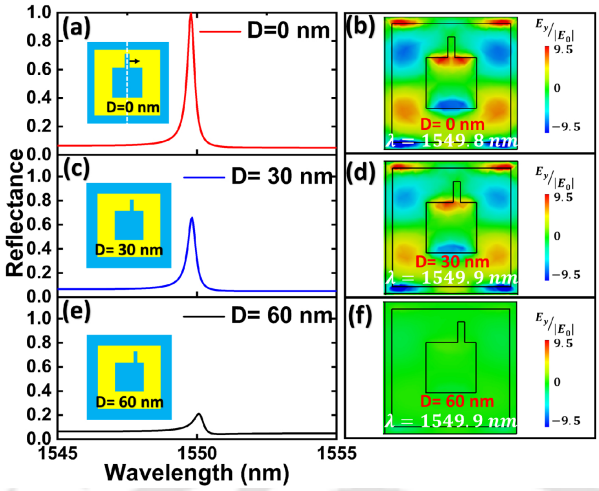

Figure 3.5: Displacement of the notch along the x-direction from its original position is denoted by the parameter D. (a), (c), and (e) show the simulated reflectance spectrum for $D = 0$ nm, $D = 30$ nm, and $D = 60$ nm, respectively. (b), (d), and (f) show the calculated normalized E_y component of electric field distributions for $D = 0$ nm, $D = 30$ nm, and $D = 60$ nm, respectively. The field profiles are calculated in the x-y plane.

3.6 A Study on Parametric Analysis and Passive Tunability

To study the effect of asymmetry on the resonance, we shifted the position of the notch along the x-axis, as shown in the inset of Fig. 3.5(a). The shift is represented by the displacement parameter D. Figures 3.5 (a), 3.5 (b), and 3.5(c) show the spectrum for different values of D from 0 nm (initial position) to 60 nm along the x-axis. The reflectance was sensitive to the displacement parameter D, and this shift attenuated the reflectance.

The normalized electric field profiles, calculated at the resonance wavelength for the three different D values (as shown in Figs. 3.5(b), 3.5(d), and 3.5 (f), indicated that the field strength decreased as the parameter D increased. The resonance weakened with increasing D, resulting in a decrease in reflectance. To examine the tunability of the response in our design with respect to different structural parameters, we first varied the periodicity of the proposed metasurface design from 720 nm to 770 nm. Figure 3.6 (a) shows the simulated contour color plot representation corresponding to the variation in periodicity. The changes in periodicity affected the near-field coupling among the unit cells. Increasing the periodicity without changing other unit cell parameters reduced the packing fraction and the effective refractive index of the metasurface. Consequently, the resonance wavelength shifted to shorter wavelengths.

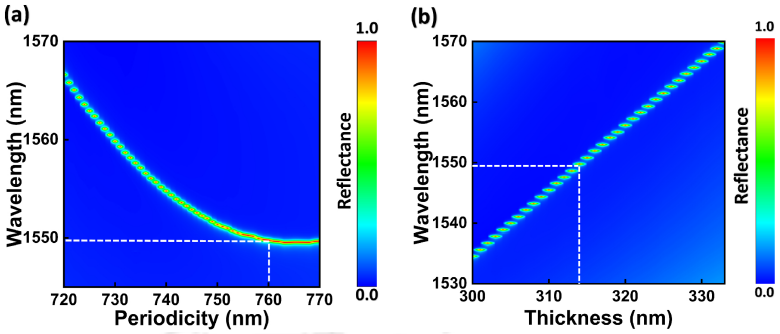

Figure 3.6: Simulation-based parametric analysis of the proposed design with the contour color plot for varying: (a) the periodicity of the unit cell and (b) the thickness of the GaAs layer. The white dashed line shows the optimized value of the parameter for a resonance at the 1549.8 nm wavelength.

Figure 3.6 (b) shows the contour plot for the reflectance spectrum with varying thickness. A red shift in the resonance wavelength was observed as the thickness of the GaAs layer increased, due to the increase in the effective refractive index of the medium [59],[60]. The parametric analysis demonstrated that the resonance wavelength can be tuned within the optical communications band (1530–1565 nm) by varying the geometrical parameters of the structures.

3.7 Summary

This chapter presented the design and analysis of a metasurface-based narrow bandpass filter operating in the optical C-band wavelength region (1530–1565 nm). The filter exhibited an ultra-narrow FWHM of 0.31 nm and a high Q-factor of nearly 5140 at the resonance wavelength of 1549.8 nm. The sharp resonance mode is excited by leveraging the in-plane symmetry-breaking approach. We have presented an analysis based on the Fano formula and near-field distributions. The near-field distribution closely resembles a coupled quadrupolar field distribution. The dependency of the Q factor on the asymmetry and the evolution of the resonance mode with asymmetry shows the quasi-BIC-like behaviour of the resonance. The filter demonstrated nearly 100% reflectance with a flat background spectral response of less than 20%reflectance across the entire C-band. The characteristic of the resonance mode is investigated by using the multipolar decomposition technique, which firmly validates the quadruple nature of the mode. The filter wavelength can be tuned in the entire C band by varying the periodicity and thickness of the GaAs layer. These findings suggest the potential of this metasurface design for

developing narrow-band pass filters and sensors that function within the optical C band region.

CHAPTER 4

HIGH-Q RESONANT ALL-DIELECTRIC METASURFACES FOR REFRACTIVE INDEX AND TEMPERATURE SENSING

4.1 Introduction

The previous chapter discussed a narrow band filtering response achieved in an all-dielectric metasurface via symmetry protected quasi BIC mode. In this chapter we will discuss application of such high Q mode as a refractive index and temperature sensor. The high quality factor resonance in metasurface enhances the trapped electromagnetic field, leading to strong light–matter interaction. High-Q factor resonances with extremely narrow line widths enables measurement of slight spectral shift in the spectrum. The efficiency of a sensor is measured in terms of its sensitivity and Figure of Merit (FoM). Such high Q factor resonance are a good candidate for a sensor with good Figure of Merit (FoM) and Sensitivity (S). Although plasmonic metasurfaces exhibits strong electric field enhancement for various sensing applications, the inherent losses of the metals used in these structures often present limitations. The resonances in the plasmonic metasurfaces are broad in nature due to the ohmic losses. Minor spectral shift caused by surrounding ambiance can not be detected in a broad resonant spectra. Such metasurface design possesses a low FoM (values below 100) in sensing application [65][66]. These limitation

Part of the results of this Chapter have been published in the following papers: Bhowmik, B. K., Bhowmik, T., Pandey, P. K., Raju, M. S., Sikdar, D., and Kumar, G. "All-dielectric asymmetric planar metasurface based dual-parametric sensor." *Optics Communications*, vol. 550, 2024, p. 129880.

hihghlights the use of all-dielectric metasurface as an efficient substitute to the metallic counterpart. In this context, Yu et al. investigated an all-dielectric nanohole cuboid array metasurface exploiting symmetry-protected BIC approach [67]. The sensing performance of the design shows a sensitivity of 300 nm/refractive index unit (RIU) and an FoM 440 RIU^{-1}. In a similar study Liu *et al*. investigated an all-dielectric silicon split ring metasurface to achieve a high-performance refractive index sensor [68]. The maximum FoM achieved for the design is 56.5 RIU^{-1}. Li et al. investigated the sensing performance of an all-dielectric metasurface by utilizing sharp multiple Fano resonances[69]. All this existing study shows that the FoM and Q factor of a metasurface-based sensor can be further enhanced by utilizing the nonradiative nature of the sharp Fano resonance [70] [71] [72]. By breaking the in-plane symmetry with a removed rectangular portion from the metasurface design, turns the BIC into a quasi-BIC mode having a finite and tunable Q factor. The finite Q-BIC mode manifests in the transmission spectrum as sharp Fano lineshape resonance. In recent studies, a very limited number of works have addressed the simultaneous sensing of both temperature and refractive index [73][74]. Although various existing techniques—such as Fiber Bragg Gratings [75], photonic crystals [76], and bottle resonators [77] have been employed to demonstrate dual-parameter sensing, these methods often face challenges related to size, sensitivity, and integration capabilities. There is a significant room to further investigate designs which shows a better dual parametric sensing performance. In this work, we have excited a sharp resonance mode with a very high Q factor of 2.8×10^4 exploiting the symmetry breaking approach. The resonance wavelength shows high sensitivity to the refractive index of the background material. In addition to this, the temperature dependency of the resonance wavelength is studied by incorporating the thermo-optic effect in to the constituents of the metasurface. By leveraging these two features this chapter discusses the dual parametric sensing application using a GaAs based all-dielectric metasurface design. The design shows a very high Q resonant response under the in plane symmetry breaking effect.

The chapter is organized as follows. Section 4.2 gives the structural and modeling details of the metasurface design. Sections 4.3-4.5 present the analysis of the resonant behaviour using the classical Fano formula, near-field distributions, and the multipolar decomposition theory. The last sections demonstrate the performance of the design as a refractive index and temperature sensor.

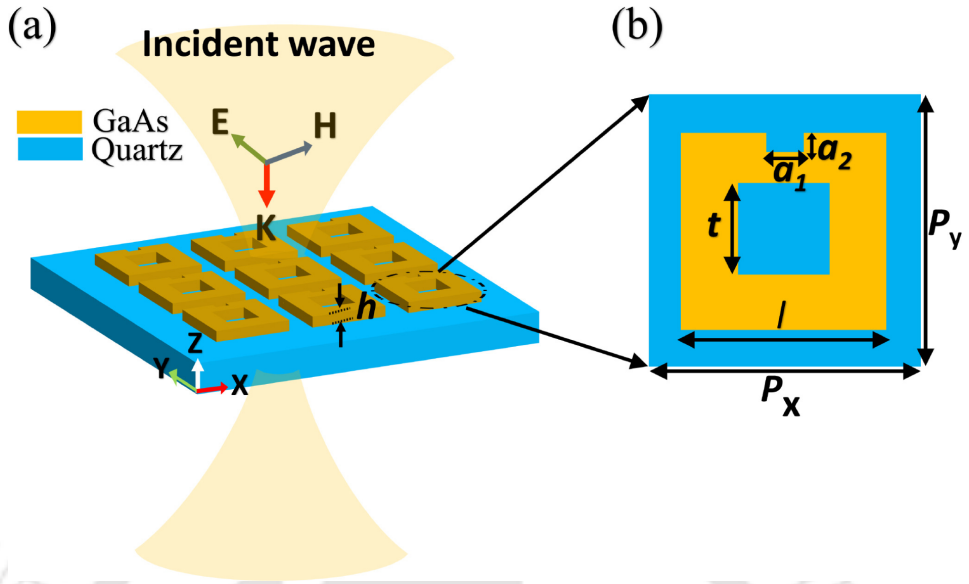

Figure 4.1: (a) The proposed metasurface design under the excitation of a normally incident TE-polarized electromagnetic wave. (b) The top view of the metasurface "unit cell" with periodicity $P_x = P_y = 746$ nm, length of the GaAs square block $l = 680$ nm, size of the outer cut $a_1 = 120$ nm, $a_2 = 75$ nm, and thickness of the GaAs block $h = 315$ nm.

4.2 The geometry of the metasurface

The periodic array of the all-dielectric metasurface is shown in Fig. 4.1(a). The metasurface unit cell has a periodicity $P_x = P_y = 746$ nm. A square air hole of side length $t = 290$ nm has been etched into a GaAs block of thickness h= 315 nm and length l= 680 nm, which is placed on top of a Quartz substrate. To disrupt the design's in-plane symmetry, an outside cut of size n_x= 120 nm and n_y= 75 nm is introduced, as shown in Fig. 4.1(b). Considering the typical technological limitations imposed by electron beam lithography, all geometrical parameters of the design are optimized. We have used commercially available CST microwave studio suite software for designing, optimizing, and interpreting the results. The metasurface is numerically simulated using a frequency domain solver. The boundary conditions are set as unit cell along X- and Y-directions, as they most closely resemble the metasurface. For the source/probe position, the boundary condition is chosen as "open (add space)" and "open". A tetrahedral meshing is used with a very fine mesh size. The metasurface design is excited with a normally incident, y-polarized (TE polarized) electromagnetic wave propagating along the – Z-direction.

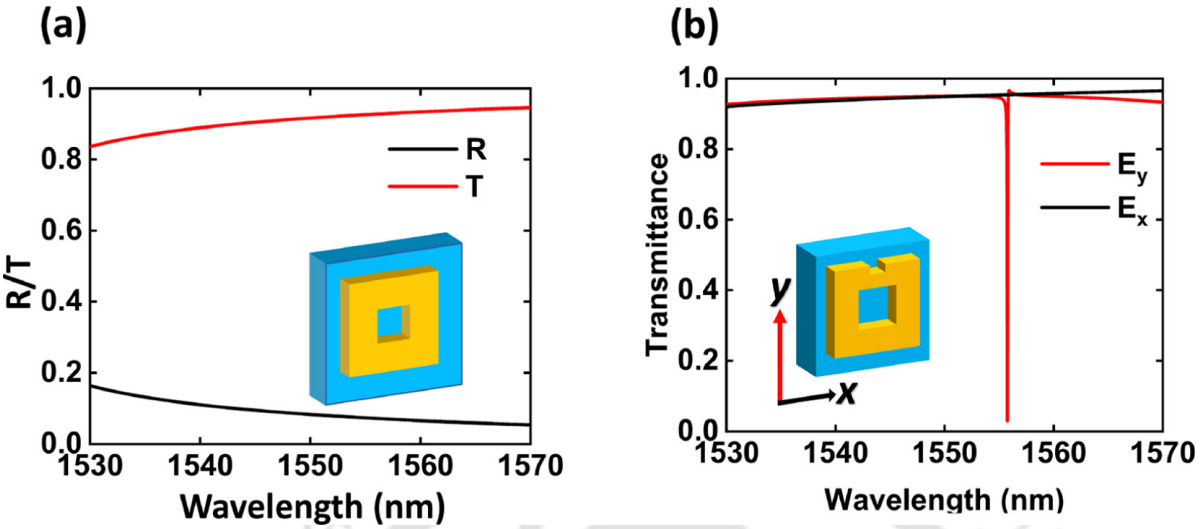

Figure 4.2: (a) The simulated reflectance and transmittance of the design without disturbing the symmetry, (b) the calculated transmittance spectrum after introducing an asymmetry for two orthogonal polarization states of the incident wave.

4.3 Analysis of the transmission spectrum and near field distributions

Fig.4.2(a) shows the simulated reflectance and transmittance spectrum for the hollow GaAs nanocuboid metasurface without any asymmetry. In the 1530–1570 nm wavelength region, nearly flat reflectance and transmittance spectra are achieved. A sharp resonance is excited at a wavelength of 1555.8 nm by slightly disrupting the nanocuboid's in-plane symmetry by making an outside cut from the mid-edge of the cuboid, as shown in Fig. 4.2(b). The design exhibits a sharp resonance for polarization along the Y-axis in the transmittance mode, while the resonance completely disappears for the orthogonal polarization condition (along the X-axis). For the remainder of the work, we have considered only the y-polarized electromagnetic wave to excite the metasurface. The Fano nature of the asymmetric resonance lineshape can be validated by comparing the simulated spectrum with the expected lineshape from the Fano formula . The resonance spectrum can be fitted using the Fano formula [51]:

$$T_{Fano}(\omega) = \left| a_1 + ia_2 + \frac{b}{\omega - \omega_0 + i\gamma} \right|^2 \tag{4.1}$$

where a_1, a_2, and b are real constants, ω_0 is the resonance frequency, and γ is the damping rate. The parameters are obtained by fitting the curve to the simulated transmittance

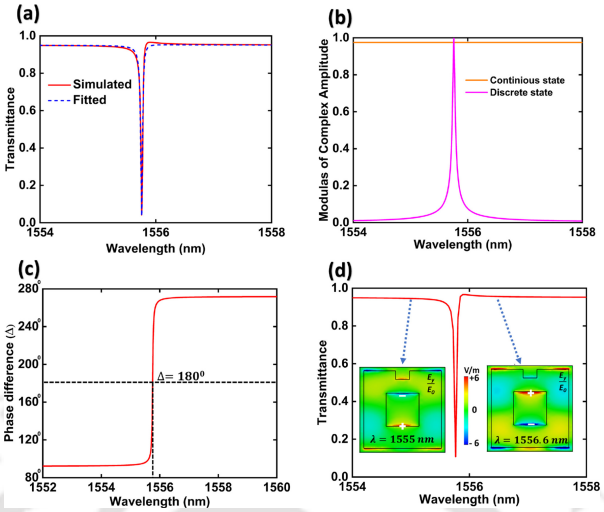

Figure 4.3: (a) The transmittance spectrum of the metasurface design showing resonance at a wavelength of 1555.8 nm. The blue dashed curve denotes the fitted curve using the Fano formula. (b) The plot of $|C_1|$ (continuous state) and $|C_2|$ (discrete state). (c) Calculated phase difference $\Delta = \arg(C_2) - \arg(C_1)$ between the continuum and the discrete state. (d) The normalized y-component of the electric field at wavelengths 1555 nm (slightly below the resonance wavelength) and 1556.6 nm (above the resonance wavelength).

spectrum. Fig. 4.3(a) displays the fitted transmittance spectrum. The good match between the simulated and fitted curves confirms the Fano nature of the resonance. The Q factor of the resonance can be extracted using the expression $Q = \frac{\omega_0}{2\gamma}$. The blue dashed line in Fig. 4.3(a) indicates a Fano-fitted spectrum with a Q factor of approximately 2.8×10^4. The Fano resonance originates from the destructive interference between the discrete state and the continuum. From the fitted parameters, the complex amplitudes of the continuum and discrete states can be extracted as [78] [79]:

$$C_1 = a_1 + ia_2, \tag{4.2}$$

$$C_2 = \frac{b}{\omega - \omega_0 + i\gamma}, \tag{4.3}$$

where C_1 denotes the complex amplitude of the continuous state, and C_2 denotes the complex amplitude of the discrete state. Fig.4.3(b) shows the modulus of the calculated continuous and discrete amplitude spectra using the Fano formula. Fig.4.3(c) shows the phase difference between the continuous and discrete states, which can be calculated as:

$$\Delta = \arg(C_2) - \arg(C_1). \tag{4.4}$$

The plot shows a phase difference of 180° exactly at the resonance wavelength. This destructive interference between the continuous and discrete states leads to the sharp

Fano resonance mode. Fig.4.3(d) displays the simulated normalized y-component electric field distributions below and above the resonance wavelength. The field distributions are antisymmetric, providing strong supporting evidence for the calculated phase spectrum.

4.4 Multi polar decomposition of the resonant metasurface

To further investigate the nature of the excited resonance mode, we employed a multipolar decomposition technique for the metasurface unit cell [58]. The induced current density, $J(r,\omega)$, in the metasurface unit cell can be calculated from the simulated electric field distribution $E(r)$ and the effective refractive index distribution $n(r)$ [58]:

$$J(r) = -i\omega\epsilon_0(n^2-1)E(r), \tag{4.5}$$

where ϵ_0 is the permittivity of free space. The electric dipole (P), magnetic dipole (m), electric quadrupole (Q_e), and magnetic quadrupole (Q_m) can be expressed as:

$$P_\alpha = -\frac{1}{i\omega}\left[\int j_\alpha j_0(kr)d^3r + \frac{k^2}{2}\int \left(3(r\cdot J)r_\alpha - r^2 j_\alpha\right)\frac{j_2(kr)}{(kr)^2}d^3r\right], \tag{4.6}$$

$$\alpha = \frac{3}{2}\left[\int (r\times J)_\alpha \frac{j_1(kr)}{kr}d^3r\right], \tag{4.7}$$

$$\begin{aligned} Q^e_{\alpha\beta} = -\frac{1}{i\omega}\Bigg[&\int \left(3\left(r_\beta J_\alpha + r_\alpha J_\beta\right) - 2(\mathbf{r}\cdot\mathbf{J})\delta_{\alpha\beta}\right)\frac{j_1(kr)}{kr}d^3\mathbf{r} \\ &+ 2k^2\int \left(5r_\alpha r_\beta(\mathbf{r}\cdot\mathbf{J}) - r^2\left(r_\alpha J_\beta + r_\beta J_\alpha\right) - r^2(\mathbf{r}\cdot\mathbf{J})\delta_{\alpha\beta}\right)\frac{j_3(kr)}{(kr)^3}d^3\mathbf{r}\Bigg] \end{aligned} \tag{4.8}$$

$$Q^m_{\alpha\beta} = 15\left[\int r_\alpha(r\times J)_\beta + r_\beta(r\times J)_\alpha\frac{j_2(kr)}{(kr)^2}d^3r\right], \tag{4.9}$$

where $\alpha,\beta = x,y,z$; c is the speed of light in a vacuum, k is the magnitude of the propagation vector, and $j_q(kr)$ is the spherical Bessel function. The total scattering cross-section can be expressed as the sum of the aforementioned multipole components [58]:

$$C^{\text{total}}_{\text{sca}} = \frac{k^4}{6\pi\epsilon_0^2|E_0|}\left[\sum(|P|^2 + \left|\frac{m}{c}\right|^2)\right] + \frac{1}{120}\sum\left(|Q^e|^2 + \left|\frac{kQ^m}{c}\right|^2 + \ldots\right), \tag{4.10}$$

where E_0 is the amplitude of the incident electric field. We employed the FDTD simulation technique to export the electric field and refractive index distribution of the unit cell.

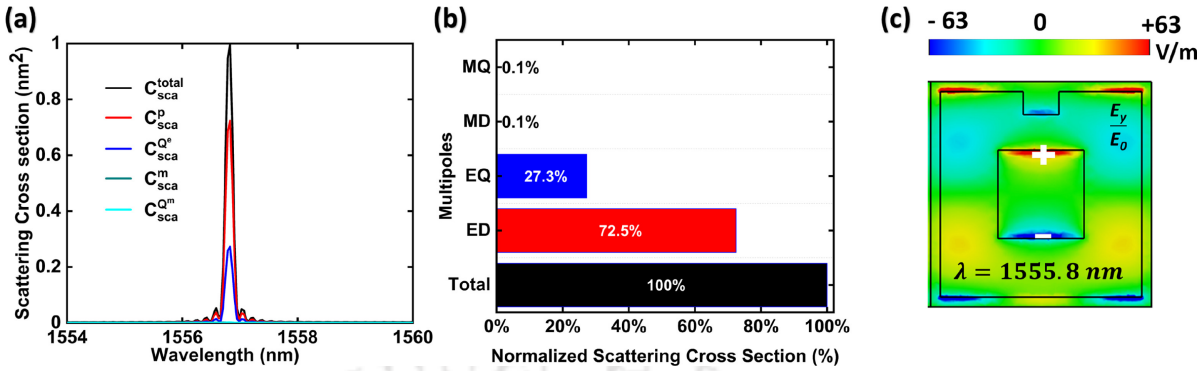

Figure 4.4: (a) Multipolar analysis of the proposed metasurface design to determine the contribution of different multipole moments. C_{sca}^{p}, C_{sca}^{m}, $C_{\text{sca}}^{Q_e}$, $C_{\text{sca}}^{Q_m}$, and $C_{\text{sca}}^{\text{total}}$ represent the scattering cross-section for the resonator due to electric dipole, magnetic dipole, electric quadrupole, magnetic quadrupole, and the total scattering cross-section, respectively. (b) The normalized multipole distributions at the resonance wavelength. ED, EQ, MD, and MQ represent the electric dipole, electric quadrupole, magnetic dipole, and magnetic quadrupole, respectively. (c) The normalized E_y component of the electric field distribution is simulated at the resonance wavelength.

The current density and other multipolar components are calculated using the MATLAB code introduced in[58].

The calculated multipolar decomposition is shown in Fig.4.4(a). As illustrated in Fig.4.4(b), the electric dipole component is the strongest contributing factor at the resonance wavelength, and the electric quadrupole moment also contributes. The resonance wavelength is 1556.8 nm. There is a slight difference between the resonance wavelength from the multipolar analysis and that calculated using CST. This discrepancy arises from the differences in the calculation methods of CST and FDTD. The simulated normalized E_y component of the electric field distribution (as shown in Fig.4.4(c)) at the resonance wavelength of 1555.8 nm also indicates the excitation of dipole modes at the resonance wavelength. The electric dipole nature results from structural asymmetry, leading to uneven charge distribution in the metasurface unit cell. The influence of the asymmetry on the resonance wavelength and quality factor will be studied in the next section.

4.5 Relationship of the Q factor with asymmetry: the inverse quadratic dependency

Next, we studied the effect of asymmetry on the Q-factor of the resonance and developed a relationship between the observed Fano resonance with the asymmetry parameter. We

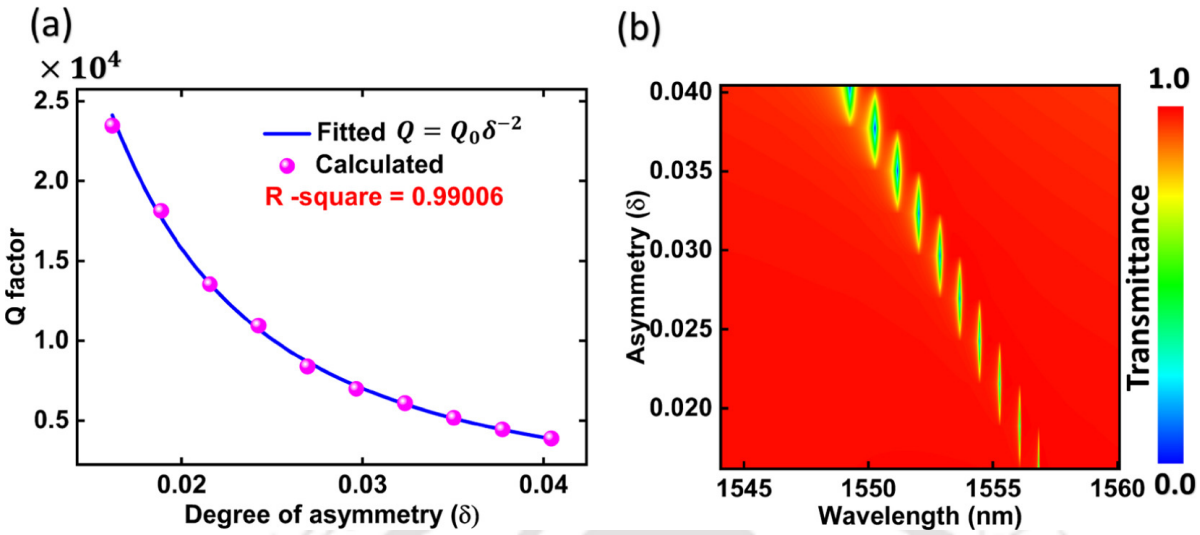

Figure 4.5: (a) Dependence of the Q factor on the degree of asymmetry. The blue line shows an inverse square fitting with the degree of asymmetry (δ), with $R^2 = 0.99006$.(b) The contour plot shows a comprehensive view of the resonance wavelength shift as well as the variation of the full width at half maximum (FWHM) of the resonance mode with the degree of asymmetry.

defined the asymmetry parameter as

$$\delta = \frac{\Delta S}{S}$$

where S is the total area of the GaAs block of a unit cell and ΔS is the area of the symmetry broken part. The Q factor of the resonance mode gradually increases as the degree of asymmetry decreases, and at $\delta = 0$, the Q factor tends to have an infinitely large value. Fig.4.5 (a) shows the effect of asymmetry on the Q factor of the resonance. The plot of the Q factor versus the degree of asymmetry shows a good fitting with the relation:

$$Q = Q_0 \delta^{-2}$$

where Q_0 is a constant depending on the geometry of the structure. This relation suggests that the Q factor of the resonance mode can be controlled by changing the asymmetry of the metasurface. The position of resonance wavelength blue shifts as the asymmetry increases (as shown in Fig. 4.5(b)). The introduction of asymmetry reduces the fraction of high refractive index material on the metasurface; hence, the effective refractive index of the metasurface decreases. As a result, the resonance wavelength's position shifts to the lower wavelength.

However, the Q factor of the resonance mode in a periodic metasurface is limited by the number of unit cells or periods. The minimum number of unit cells (U_n) required to

sustain a sharp, high-quality factor resonance of value Q is

$$U_n > \frac{Q}{\pi}$$

[80][81]. So, in practical situations, the maximum value of the quality factor is limited by the finite array size of the metasurface. Furthermore, the total Q factor Q_{tot} can be defined as

$$\frac{1}{Q_{\text{tot}}} = \frac{1}{Q_{\text{rad}}} + \frac{1}{Q_{\text{nr}}}$$

, where Q_{rad} and Q_{nr} indicate the radiative Q-factor and non-radiative Q-factor, respectively[82]. The Q_{nr} covers the dissipative losses, losses due to surface roughness, and deviation due to fabricated errors. The finite value of Q_{nr} makes the Q_{tot} of the Fano resonance finite.

4.6 Application as sensor

The high Q factor and local field enhancement are significant for sensing applications. The high Q factor resonance mode shows the capability to detect minor spectral shifts caused by weak refractive index variation of the ambient medium or temperature of the surroundings. The Q factor at the resonance wavelength 1555.8 nm reaches 2.8×10^4.

Additionally, a high spectral contrast ratio is desirable for sensing applications because it enhances the sensitivity and precision of the sensor. In practical terms, a high spectral contrast ratio enables a larger signal-to-noise ratio (SNR) and makes the resonant feature stand out more prominently against any background noise or fluctuations. The spectral contrast (S.C.) of the Fano resonance can be defined as [83]:

$$S.C. = \frac{(T_{\text{peak}} - T_{\text{dip}})}{(T_{\text{peak}} + T_{\text{dip}})} \times 100\%$$

The spectral contrast (S.C.) reaches 90% for the proposed design. Such an ultra-high Q factor resonance and a high spectral contrast make the metasurface design promising for sensing-based applications. The spectral shift can be caused by both the variation of the background refractive index as well as the temperature of the surrounding environment.

The following equation describes the dependence of the resonance shift on the variation of the refractive index and temperature [84]:

$$\Delta\lambda = \frac{\partial\lambda}{\partial n}\Delta n + \frac{\partial\lambda}{\partial T}\Delta T + \left(\frac{\partial\lambda}{\partial n} \times \frac{\partial n}{\partial T}\right)\Delta T$$

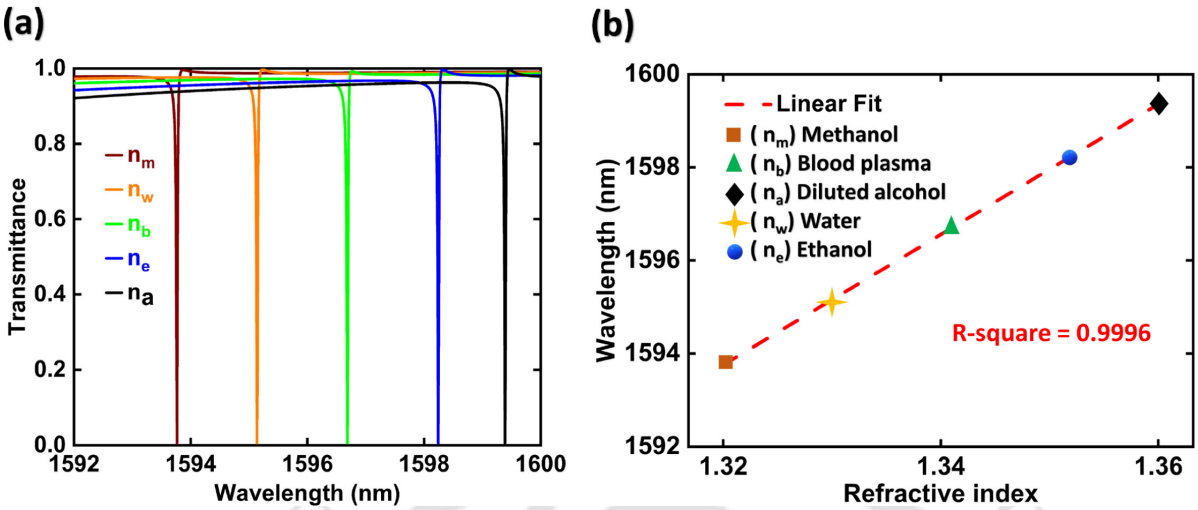

Figure 4.6: The transmittance spectrum for the different background media, where n_m, n_w, n_b, n_e, and n_a represent the refractive indices of methanol, water, blood plasma, ethanol, and diluted alcohol, respectively. (b) Linearly fitted plot of the refractive index versus resonance wavelength. The R^2 value of 0.9996 indicates good linearity between the wavelength shift and the change in refractive index.

Here, T is the temperature, and n is the refractive index of the background medium. The first two terms of the equation refer to the independent variation of refractive index and temperature, while the third term refers to the thermo-optic effect of the ambient medium.

Assuming the proposed design works in the linear range, the general form of the equation can be formulated as follows:

$$S_n(\Delta n + \Delta T \frac{dn}{dT}) + S_T \Delta T = \Delta\lambda$$

where S_n and S_T are the refractive index (RI) and temperature sensitivity coefficients. The coefficients of sensitivity can be calculated from the RI and temperature versus spectral shift plot.

4.7 Refractive index sensing

First, we investigated the influence of the background medium on the resonance wavelength. To demonstrate the refractive index sensing response of the design, we considered methanol (RI = 1.319) [86], water (RI = 1.33)[87], blood plasma (RI = 1.341) [60], ethanol (RI = 1.352) [88], and diluted alcohol (RI = 1.36) [89]solution as the surrounding medium. The transmittance spectrum of the proposed design is calculated for each case. Fig.4.6(a)

shows the transmittance spectrum corresponding to the changes in the background refractive index. The resonance wavelength shows a red shift as the refractive index of the surrounding medium increases. At the same time, the Q factor and spectral contrast of the resonance remain the same over the changes in the background refractive index.

Thanks to the sharp, high-Q nature of the Fano resonance, even a minor spectral shift is visible despite a very small change in the refractive index. The slope of the linearly fitted resonance wavelength versus refractive index data (as shown in Fig.4.6(b)) leads to a sensitivity of 140 nm RIU^{-1}. A quantitative statement about the performance of a refractive index-based sensor can be made by calculating the figure of merit (FoM). The FoM is defined as the ratio of sensitivity to the line width of the resonance [68],

$$\text{FoM} = \frac{S}{\Delta\lambda},$$

where S is the sensitivity and $\Delta\lambda$ is the line width of the resonance.

The linewidth of the Fano resonance can be calculated as the full width between the peak and the dip of the resonance[24], which is calculated to be 0.026 nm. The sharp resonance feature of the proposed metasurface design leads to an FoM value of 5384 RIU^{-1}. This value is much larger than plasmonic metamaterial-based sensors reported in [92][93]. Further, we have shown a comparison of the FoM of the metasurface-based sensor reported in the literature with the proposed design. As shown in Table 1, it can be seen that our proposed all-dielectric metasurface-based design shows a significant improvement in enhancing the FoM of metasurface-based sensors.

4.8 Temperature sensing

Next, for the study of temperature sensing, the refractive index of the background material is set to 1. The thermal expansion coefficients of the materials can be neglected due to the smaller size of the structure. Incorporating the thermo-optical coefficients into the simulation, the temperature is varied from 20°C to 80°C. At room temperature, the thermo-optic coefficients for GaAs and quartz are $2.67 \times 10^{-4}/K$ [95] and $-7.94 \times 10^{-6}/K$ [96], respectively.

Fig.4.7(a) shows the transmission spectrum of the metasurface design at different temperatures. Fig. 4.7(b) shows the linearly fitted plot of temperature versus the resonance wavelength. The sensitivity of the temperature sensing can be calculated as:

$$S_T = \frac{\Delta\lambda}{\Delta T}\,\text{pm/°C} = 72\,\text{pm/°C}.$$

Table 4.1: Comparison of FoM parameter of the metasurface-based sensor.

Type	**Wavelength range**	**Reported FoM**	**Year**
All-dielectric semicircle disk metasurface [90]	Near IR	2970 RIU^{-1}	2023
Silicon split-ring metasurface [79]	1100 nm–1200 nm	130 RIU^{-1}	2023
Hollow cylindrical tetrameric clusters [91]	Near IR	483 RIU^{-1}	2022
Plasmonic metasurface [92]	Visible	109 RIU^{-1}	2022
Nanoring array cavity metasurface [93]	Near IR	119 RIU^{-1}	2021
All-dielectric nanohole cuboid array metasurface [67]	Near IR	400 RIU^{-1}	2021
All-dielectric Si split ring-based metasurface [68]	Near IR	56.5 RIU^{-1}	2018
This Work	Near IR	**5384 RIU^{-1}**	**2023**

Table 4.2: Performance comparison of the metasurface-based design with other temperature sensors.

Year	**Structure type**	**Sensitivity**	**Wavelength range**
2023 [74]	Silicon disks with tilted split gap	54 pm/°C	2200 nm–3000 nm
2017 [73]	Array of silicon nanoblocks	58.94 pm/°C (design-1), 46.05 pm/°C (design-2)	1300 nm–1700 nm
2017 [76]	Photonic crystal	30.1 pm/°C	Near IR
2016 [84]	Fiber sensor	59 pm/°C	1540 nm–1600 nm
2021 [94]	Sm^{3+}:ZnO micro-spheres	0.04 pm/°C	Visible range
This work	All-dielectric asymmetric metasurface	**72 pm/°C**	**Near IR**

The FoM of the design will be small for temperature sensing as the wavelength shift is in the 'pm' scale. However, it is found that our design shows good temperature sensitivity, and hence the design can be used as a dual parametric sensor (for RI and temperature). Table 2 shows a performance comparison of some reported literature on temperature sensing.

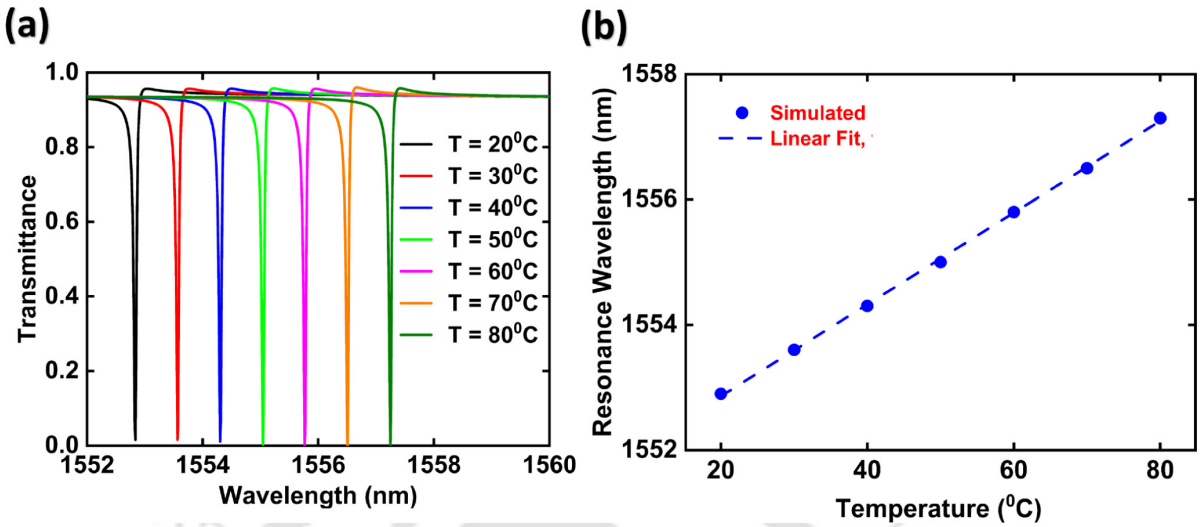

Figure 4.7: (a) The transmittance spectrum of the metasurface design at different temperatures, (b) the linearly fitted plot of the temperature versus resonance wavelength, the slope of the graph gives the temperature sensitivity of the design.

4.9 Summary

This chapter thoroughly discusses a dual parametric sensing mechanism using an asymmetric all-dielectric metasurface. The metasurface's resonant response fitted well with the classical Fano formula, confirming the Fano nature of the observed resonance. This resonance exhibited a high Q factor of 2.8×10^4, making it suitable for highly sensitive detection applications.

The resonance wavelength of the metasurface shows dependency on the refrcative index of the background material. By simulating different surrounding material (methanol, water, blood plasma, ethanol, and diluted alcohol) we observed a clear red shift in the resonance wavelength as the refractive index increased. This shift, combined with the stable Q factor and high spectral contrast, shows a good efficiency of the metasurface as a refractive index sensor. The calculated sensitivity was 140 nm/RIU, and the Figure of Merit (FoM) reached a very high value 5384 RIU^{-1}.

Next, the temperature sensing is investigated by incorporating thermo-optic coefficients of the constituent materials of the metasurface and varying the temperature from 20°C to 80°C. The simulation results indicated a linear relationship between the resonance wavelength and temperature, with a sensitivity of 72 pm/°C. This metasurface based design has the potential to replace sensor devices based on a plasmonic approach owing to high-quality modes. The use of such metasurface design with a high Q Fano

resonance can be a powerful tool for developing advanced sensors with applications in biomedical sensing, environmental monitoring, and other fields where high precision and sensitivity are essential.

CHAPTER 5

EXCITATION OF QUASI BIC MODE VIA SLECTIVE SYMMETRY BREAKING IN TERAHERTZ METASURFACE

5.1 Introduction

In the previous chapters, we explored the application of high-Q Bound States in the Continuum (BIC) modes, specifically as narrow bandpass filters and dual parametric sensors in near IR wavelength. These studies emphasized the potential of sharp quasi BIC (which manifests as Fano lineshape in the spectrum) in enhancing performance for optical filtering and sensing applications.

This chapter extends the concept of BICs to the terahertz metasurface domain. Here, we theoretically and experimentally investigate quasi-BIC modes' excitation and Q-factor enhancement in a metallic terahertz metamolecule system. Metallic structures are often favored for their ease of fabrication, and they offer an additional advantage over all-dielectric counterparts by potentially reducing common fabrication errors, such as etching inaccuracies. In the THz frequency range, Drude metals exhibit high conductivity and hence lower non-radiative losses compared to optical communication wavelength (near infrared range) [97]. So, handling the radiative losses is the primary challenge in this frequency region. In this context, Hansen et al. reported the excitation of trapped

Part of the results of this Chapter have been published in the following papers:Bhowmik, Bhairov Kumar, et al. "High-quality factor Quasi-BIC mode via selective symmetry-breaking approach in a terahertz metasurface." New J. Phys. 26 063024.

mode resonances in metallic THz metasurfaces [98], where the in-phase oscillations of anti-symmetric currents led to a Q factor of 27.5. Similarly, Chen *et al.* studied a nested square split-ring resonator metamaterial for efficient sensing application and achieved a maximum Q factor 30.5 in the THz range [99]. Gupta *et. al* investigated a terahertz metasurface design supporting toroidal resonance and achieved a maximum Q factor of 42.5 [62]. Zhang *et al.* further advanced this field by theoretically and experimentally demonstrating multiple bound states in the continuum (BIC) in a split-ring resonator using a symmetry-breaking approach [100]. Despite these advancements, the relatively low Q factors and structural complexity of existing designs indicate significant opportunities for further improvement. The standard approach for exciting symmetry-protected quasi-BIC modes typically involves uniformly perturbing the structural symmetry of a unit cell [2, 16], which causes all the resonators to contribute to far-field radiation. In contrast, this work introduces a selective, or non-uniform, symmetry-breaking scheme in a simple ring-shaped metamolecule system. This selective symmetry-breaking technique effectively reduces the radiation density and shows a significant improvement in controlling radiative losses and enhancing the Q factor. The chapter is divided into sections as below:

Section 5.2 discusses the simulation procedure and optimized structural layout of the metasurface. Section 5.3 explains the process involved in the sample fabrication. Section 5.4 discusses the metasurface response under the nonuniform symmetry-breaking effect. Section 5.5 presents a theoretical investigation of the bright-dark coupling mechanism in the proposed metamolecule system. Sections 5.6 and 5.7 discuss the results of sample characterization using terahertz time-domain setup and the near-field scanning terahertz microscopy setup. Finally, section 5.8 summarizes the key findings of the chapter.

5.2 Simulation and optimization

We have designed a meta-molecule system comprising four resonators or meta-atoms made of aluminum rings positioned on top of a quartz substrate, collectively referred to as a meta-molecule system. Figure 5.1 illustrates the schematic of the proposed meta-molecule system, including a detailed view of a unit cell (as shown in the inset). The optimized geometrical parameters of the meta-molecule system are periodicity (P) = $200\mu m$, width (w) = $6\mu m$, and oOuter ring radius: $r_1 = 27\,\mu$m, $r_2 = r_3 = 34\,\mu$m, and $r_4 = 41\,\mu$m. .

Finite element solver-based CST Microwave Studio suite software was used to design and optimize the proposed metasurface design. The boundary conditions were set as unit cell along the X and Y directions, and Open (add space), Open along $Z_{\max}$ and $Z_{\min}$, respectively. The transmission spectrum was simulated under the excitation of a TE-polarized (Y-polarized) normally incident electromagnetic plane wave.

5.3 Sample fabrication

Following theoretical optimization, the proposed design was fabricated in a clean room environment. A quartz wafer was used as the substrate material for the proposed meta-molecule system. The thickness of the one-sided polished quartz wafer was $500\mu m$. A thin film of aluminum, with a thickness of 200 nm, was deposited on the quartz substrate using thermal evaporation.

The wafer was then spin-coated with hexamethyldisilazane (HMDS) and S1813 positive photoresist, followed by complementary patterning using a direct laser mask writer. This step defined the areas to be etched out and those to be masked, based on our intended metasurface design. The HMDS acted as an adhesive layer for the positive photoresist (For the details of the clean room photolithography process see section 2.2).

After a 50-second development process, the sample was etched using an aluminum etchant to remove the undesired metallic parts, while the photoresist served as a protective mask for regions that were to remain part of the final metasurface structure. Finally, acetone was used to strip away the residual photoresist.

5.4 High-Q Fano Resonance Analysis Driven by Non-Uniform Symmetry Breaking

We have strategically broken the structural mirror symmetry of the metamolecule system to reduce the radiation density of the system. The proposed design shows a high-Q Fano-like resonance under the non-uniform mirror symmetry breaking of the metamolecule (as shown in Figure5.2(b)). Figure 5.2(a) shows the different schemes of symmetry breaking applied in the design to strategically enhance the Q factor by reducing radiation loss. To minimize inter-unit cell near-field interactions and study the resonance behavior primarily due to symmetry-protected BIC, we arranged the four-ring resonators

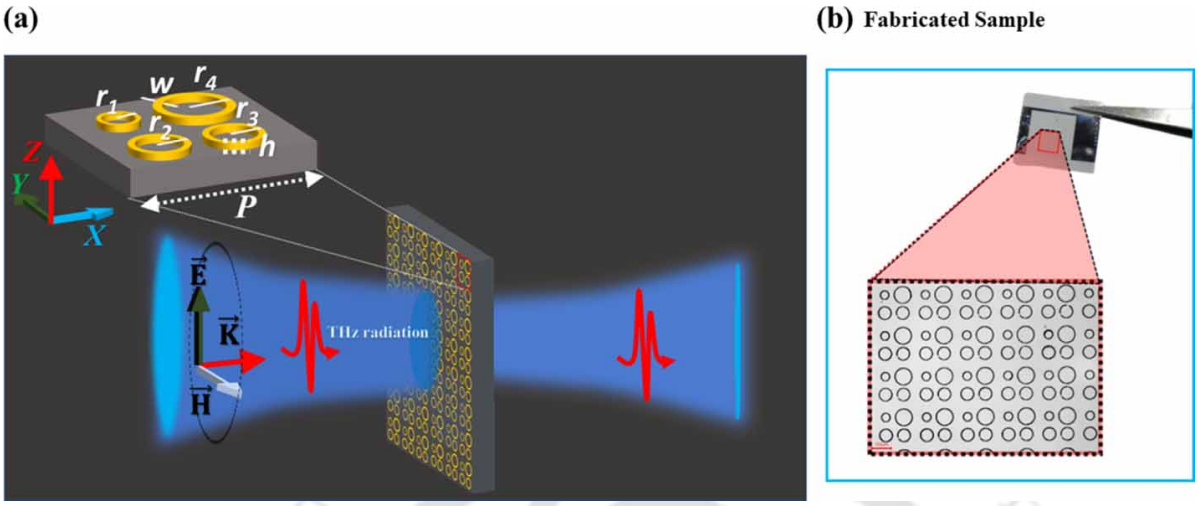

Figure 5.1: (a) Schematic of a metasurface design under the excitation of TE-polarized THz radiation. The inset shows the proposed meta-molecule unit cell, where the periodicity $P = 200\,\mu$m, width $w = 6\,\mu$m, radii $r_1 = 41\,\mu$m, $r_2 = 27\,\mu$m, $r_3 = r_4 = 34\,\mu$m, and the thickness of the ring structures $h = 200\,$nm.(b) The photograph and micrograph image of the fabricated metasurface sample using photolithography.

with a center offset of $6\mu m$. Figure 5.2(b) shows the simulated transmission spectrum corresponding to a symmetric structure, a uniform symmetry-broken structure, and a non-uniform (or selectively symmetry-broken) structure. The symmetric metasurface design exhibits a broad resonance dip at a frequency of 1.1 THz. According to previously reported studies, such metallic designs typically show a polarization-independent broad dipole resonance [101]. An additional Fano line-shape resonance appears in the spectrum as we introduce a uniform mirror symmetry-breaking effect in the system. However, a more strategic approach can be adopted to further enhance the Q factor by breaking the symmetry in a non-uniform or selective way. A significant enhancement in the Q factor, from 25.8 to 107, is observed under the non-uniform symmetry-breaking effect. The sharp spectral dip arises in a narrow frequency window alongside an additional resonance dip. The sharp resonance dip (marked as A for discussion) appears to be spectrally squeezed into a narrow frequency range. The resonance dips are marked as A, B, and C in different colors for clarity. The first resonance dip exhibits a significantly narrower linewidth compared to the second. Under the symmetry-breaking effect, the uncoupled dark resonance interacts with the broad radiation continuum and manifests as a Fano line-shape resonance embedded within the continuum [4][101][103].

The broad dipolar resonance splits as soon as the mirror symmetry of the structure is broken, and a Fano-like resonance evolves in the background of the broad resonance. To

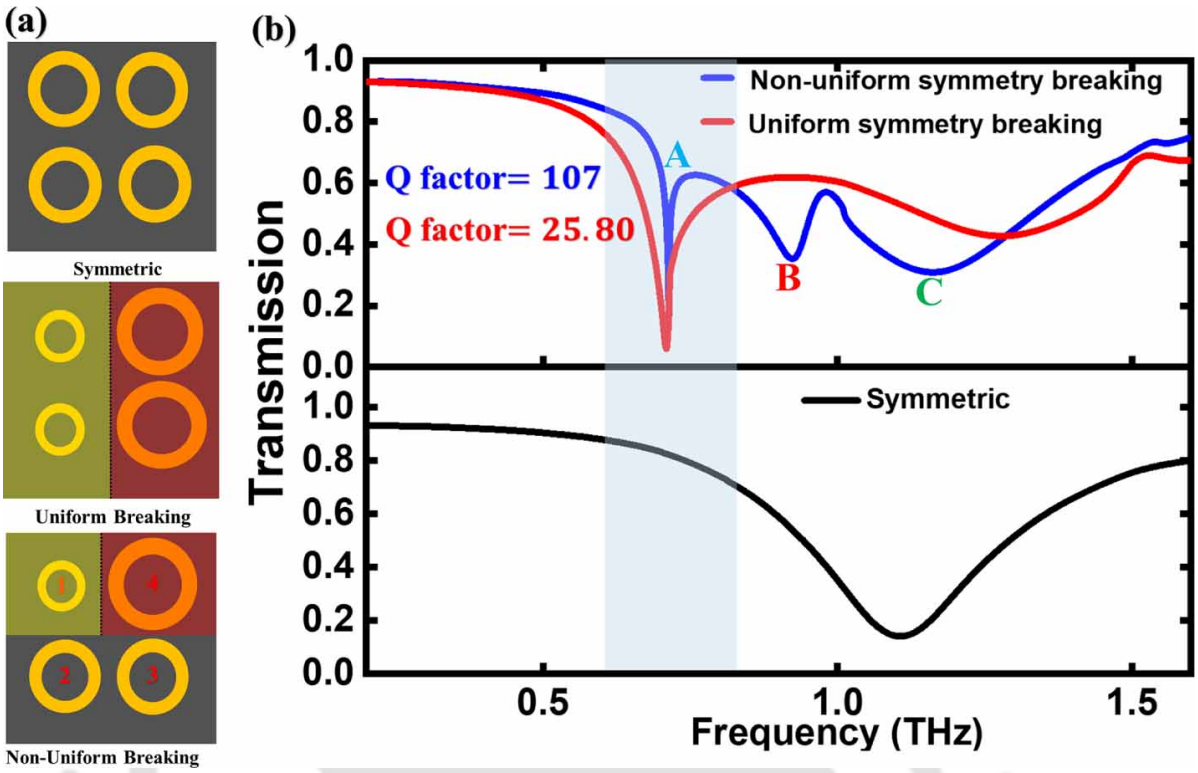

Figure 5.2: (a) The arrangement of four ring resonators in a metamolecule unit cell with three approaches: symmetric, uniform symmetry breaking, and selective symmetry breaking. The olive background resonators have a radius of $27\mu m$, the red background resonators have a radius of $41\mu m$, and the gray background resonators have a radius of $34\mu m$. (b) Simulated transmission spectrum of the symmetric meta-molecule system, non-uniformly symmetry-broken structure, and uniformly symmetry-broken structure.

better understand the splitting of the broad dipole mode, a plasmonic mode hybridization scheme is presented in Figure 5.3. In a coupled ring system, both symmetric and anti-symmetric modes are observed as a result of hybridization [104] [105]. Since the rings are smaller than the wavelength of the excitation, they can be treated as electric dipoles. Four different eigenmodes are possible, as shown in Figure 5.3 (for both transverse and longitudinal polarization of the incident electric field). Two of them are in-phase oscillations of the electric dipoles in both rings, referred to as symmetric or bright eigenmodes, as they radiate into the far field. The remaining two modes, characterized by out-of-phase oscillations, are known as dark modes, which cannot directly couple to the radiation continuum. However, as the structural symmetry is broken, the dark modes couple to the continuum with a reduced dipole moment, manifesting as sharp Fano line-shape resonances.

The coupling between two resonators depends on their spatial and respective spectral

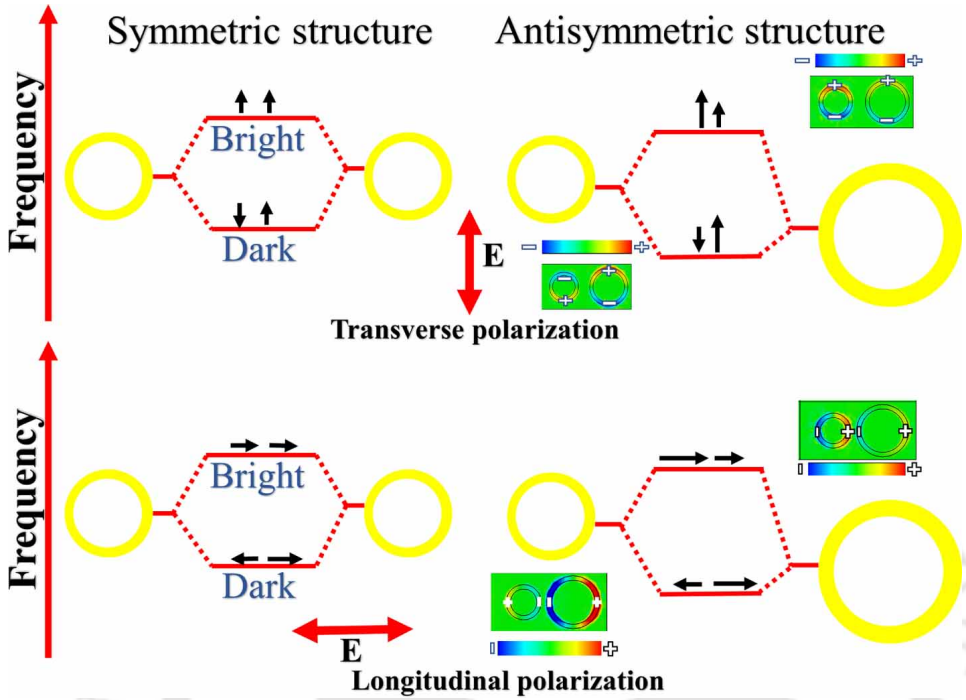

Figure 5.3: The mode hybridization scheme for a micro ring pair unit cell, where the dark mode manifests as a result of dipole detuning due to the introduction of the structural asymmetry.

positions [106][107]. To further understand the coupling mechanism, we simulated the near-field distributions of the electric field, as shown in Figure 5.4. The field profiles at the three resonance dips are depicted using different color frames, matching the distinguishing colors for the three dips marked as A, B, and C in Figure 5.2(b). Figure 4 shows that at two resonance dips, A and B, the dipole modes in each pair of resonators are antisymmetric. Longitudinally aligned pairs (with an axis parallel to the polarization) couple more effectively due to their spectral proximity and small gaps.

This effect arises because the dipole mode resonance of a circular ring resonator depends on its radius and width [108]. If the resonance wavelengths of the three-ring resonators with radii of 41 μm, 34μm, and 27 μm are denoted by λ_{41}, λ_{34}, and λ_{27}, then $\lambda_{41} \geq \lambda_{34} \geq \lambda_{27}$. Thus, resonators with radii of 41 μm and 34μm, and those with 27 μm and 34 μm will couple due to their spectral overlap. The Z-component of the electric field corresponding to resonance dips A and B (as shown in Figure 5.4) consists of combinations of symmetric and antisymmetric modes for each longitudinal pair. At resonance dip A, rings 3 and 4 oscillate in-phase, creating a sharp linewidth resonance due to the reduction of the net dipole moment by ring 2. In contrast, at dip B, rings 2 and 4 oscillate strongly in-phase, while rings 1 and 3 show weaker antiphase oscillations.

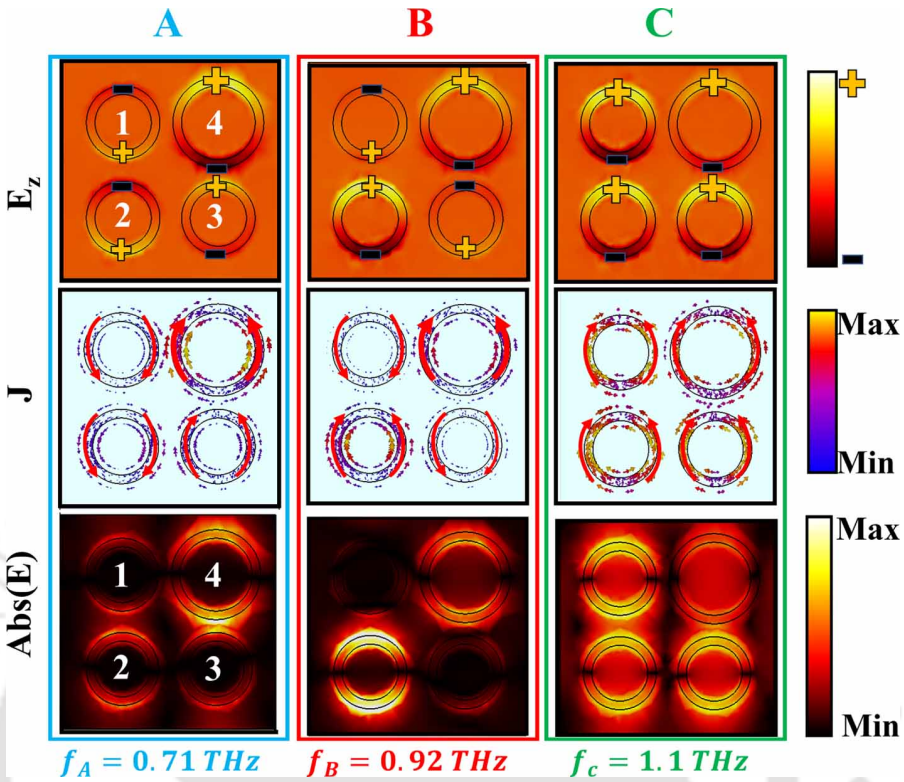

Figure 5.4: The simulated Z-component of the electric field, normalized surface current density profile, and absolute of the normalized electric field profile distributions at the three-resonance dip. The color of the frame is consistent with the font color used to depict the three-resonance dip in figure 5.2.

This is also evident from the absolute field profile for dip B, which results in a larger net dipole moment, leading to a broader Fano resonance. For resonance dip C, the E_z component shows uniform oscillation across the rings, producing a significant net dipole moment.

At resonance dip A, rings 3 and 4 behave as bright resonators, and their coupling with oppositely oscillating dark resonators generates Fano dip A. Similarly, at resonance dip B, the diagonal pair of rings 2 and 4 oscillates strongly in-phase and acts as bright resonators. Their coupling with indirectly excited dark resonators produces Fano dip B. The relationship between the sharp resonance dip and the dark resonance mode is depicted in Figure 5.5(a).

The resonant state $|\psi_1\rangle$ can be viewed as an interaction between the unperturbed or bound state and the broad radiation continuum [30]. The perturbation induces a frequency shift and dipole detuning, resulting in a sharp Fano resonance with a finite Q factor [72]. The green arrow in Figure 5.5(a) indicates the direction of the net dipole

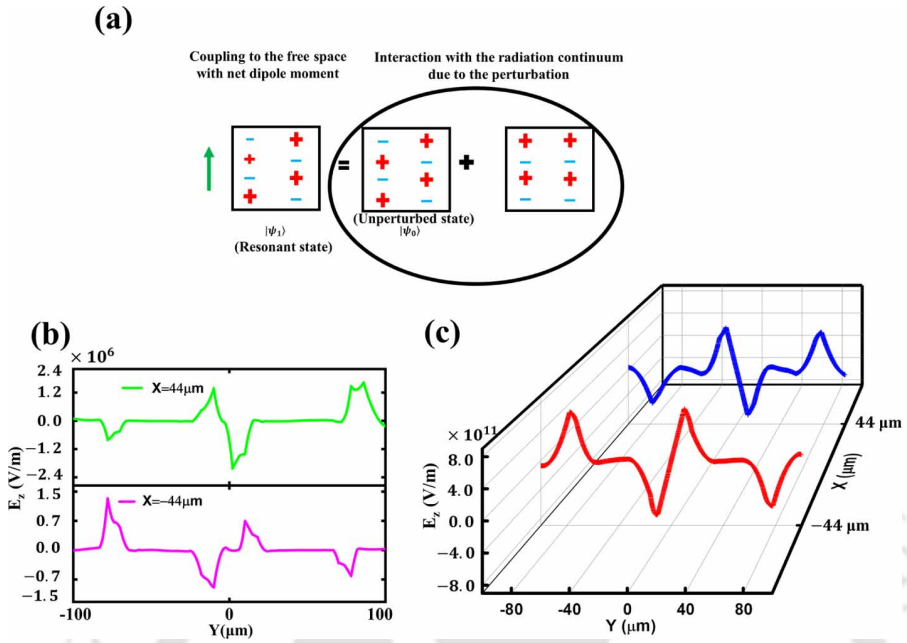

Figure 5.5: (a) A schematic description of the decomposition of the sharp resonance mode into an unperturbed dark mode and the radiation continuum. The size of the sign represents the strength of the field. (b) The 1D field plot along the Y-direction at $x = -44\,\mu$m and $X = 44\,\mu$m for the symmetry-perturbed metamolecule system. (c) The 1D field plot along the Y-direction for the symmetric structure, calculated using eigenmode analysis.

moment. Figures5.5(b) and 5.5(c) provide quantitative evidence of the dipole detuning in the metamolecule system, validating the asymmetric field strength under the perturbation effect and the symmetric field strength with zero dipole moment for the unperturbed system.

The field strength for the unperturbed mode corresponding to the Γ-point ($K_x = K_y = 0$) is calculated using eigenmode analysis in CST Microwave Studio suite simulation.

5.5 Theoretical investigation of bright-dark mode coupling in the proposed System

We have used the analytical formula based on Gallinet and Martin's *ab initio* theory [109], which provides a quantitative approach for a deeper understanding of the resonance behavior in metamaterials. This theory reveals the roles played by the electromagnetic modes and material losses in forming Fano resonance in metallic subwavelength structures. The theory is based on the interference between a radiative broad resonance

mode (continuum) and a non-radiative asymmetric mode (dark mode).In metamaterial the resonance mode which are excited directly under the excitation of electromagnetic radiation are known as bright mode. The dark modes are the modes which can not be excited directly or shows very weak coupling to the radiation continuum. According to *ab initio* theory, the resonance magnitude of the system can be expressed as the product of the symmetric (bright) and antisymmetric (dark) resonance modes, respectively [109]:

$$T(\omega) = 1 - \prod_{i,j=1}^{2} \sigma_d^i(\omega)\sigma_b^j(\omega) \tag{5.1}$$

where the superscript $i(j) = 1,2$ indicates the $i_{th}(j_{th})$ dark(bright) mode. The dark and bright resonance profile can be expressed as,

$$\sigma_d^i(\omega) = \frac{\left(\frac{\left(\omega^2-\omega_{id}^2\right)}{2\gamma_{id}\omega_{id}} + q_i\right)^2 + b_i}{\left(\frac{\left(\omega^2-\omega_{id}^2\right)}{2\gamma_{id}\omega_{id}}\right)^2 + 1} \tag{5.2}$$

$$\sigma_b^j(\omega) = \frac{K_j^2}{\left(\frac{\left(\omega^2-\omega_{jb}^2\right)}{2\gamma_{jb}\omega_{jb}}\right)^2 + 1} \tag{5.3}$$

where ω is the frequency, $\omega_d(\omega_b)$ is the central resonance frequency of the dark (bright) modes, $\gamma_d(\gamma_b)$ is the linewidth of the dark (bright) mode spectrum, K is the relative amplitude of the resonance, q is the asymmetric parameter, and b is the modulation damping parameter corresponding to the intrinsic losses. The parameters q and b shape the Fano resonance line shape. By using these analytical functions and considering bright-dark interaction, the complete transmission spectrum for the proposed system can be obtained. The excellent agreement between the numerically simulated and theoretically calculated transmission spectrum is shown in Figure 5.6(a). The parameters of the analytical expression are obtained by fitting with the spectrum obtained using numerical simulation. The values of the extracted fit parameters are reported in Table 5.1.

Table 5.1: Extracted parameters from the analytical fitting.

$\mathbf{K}_1$	$\mathbf{K}_2$	$\mathbf{q}_1$	$\mathbf{q}_2$	γ_{1d}	γ_{2d}	γ_{1b}	γ_{2b}	$\mathbf{b}_1$	$\mathbf{b}_2$	ω_{1d}	ω_{2d}
2.51	0.69	- 0.0045	- 0.128	0.0124 THz	0.056 THz	0.47 THz	0.41 THz	1.68	0.934	0.70 THz	0.95 THz

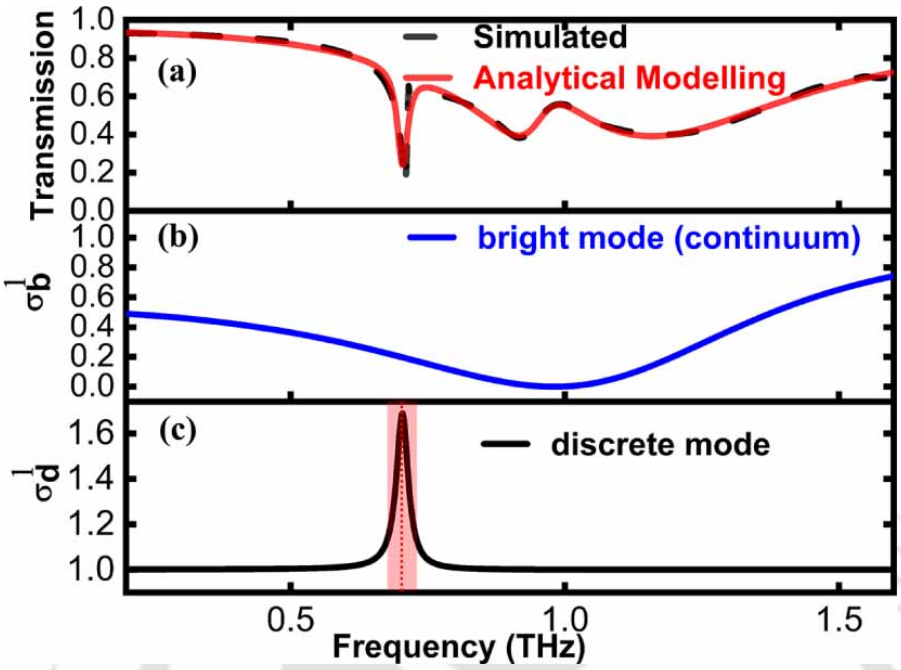

Figure 5.6: (a) The theoretically calculated transmission spectrum for a structural asymmetry $\delta = 26.4\%$. The theoretical matching validates the evidence of the bright-dark coupling mechanism. (b) The broad radiation continuum extracted using the analytical model. (c) The corresponding dark or discrete line shape extracted using the analytical fit.

The contributing bright mode, which is decomposed from the analytical modeling, is shown in Figure 5.6(b), and Figure 5.6(c) shows the corresponding discrete line shape. Equation (5.1) provides the collective influence of all the radiative continuum and the discrete dark resonance mode, yielding the complete transmission profile.

5.5.1 The Influence of Geometrical Perturbation and BIC Characteristics

To investigate the asymmetry dependence of the transmission spectrum, we have simulated the meta-molecule system for different degrees of asymmetry. The degree of asymmetry in the meta-molecule system is defined as:

$$\delta = \frac{r_1 - r_2}{r_1 + r_2} \times 100\%$$

Figure 5.7(a) depicts the transmission plot under different degrees of geometrical perturbation. It is evident from Figure 5.7(a) that the resonance mode ceases to couple with the radiation continuum as we decrease the asymmetry. This can be understood as

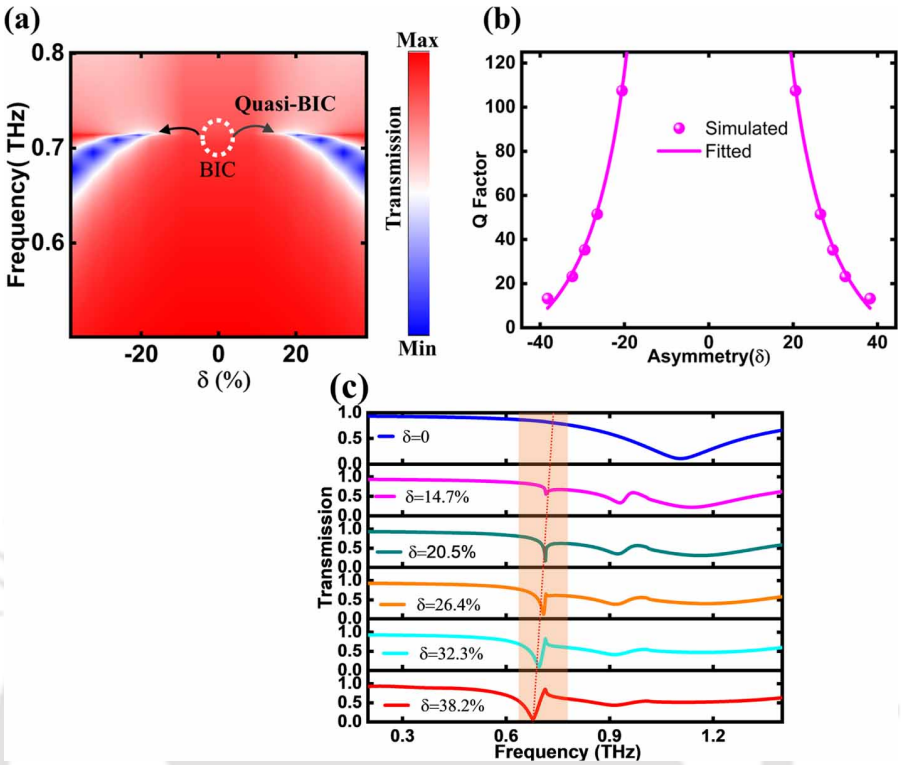

Figure 5.7: (a) The simulated transmission contour plot as a function of frequency and degree of asymmetry. (b) The asymmetry versus calculated Q factor of the sharp resonance dip. The solid line represents the fitting with the expression $Q = A\delta^{-2} +$ Correction term. (c) Evolution of the quasi-BIC in the transmission spectra versus the degree of asymmetry.

an ideal BIC mode that cannot be accessed due to its infinite Q factor or zero linewidth. This BIC mode transforms into a quasi-BIC mode under the influence of geometrical perturbation and manifests as a high-Q Fano resonance.

The Q factor of the resonance mode can be calculated by extracting the overall damping rate from the Fano fitting [72]:

$$T_{\text{Fano}} = \left| c_1 + jc_2 + \frac{\alpha}{(\omega - \omega_0 + j\gamma)} \right|^2$$

where c_1, c_2, and α are real-value constants, γ is the overall damping rate, and ω_0 is the resonance frequency. The radiative Q factor, $Q = \frac{\omega_0}{2\gamma}$, is plotted against the respective degree of asymmetry as shown in Figure 5.7(b). The Q factor of the resonance mode shows a fitting of $\frac{5.9\times10^4}{\delta^2}$ with a correction term of −33.97.

The inverse square dependence of the Q factor demonstrates the existence of the structural symmetry-protected BIC in the meta-molecule system [100][72]. The calculated transmission against varying degrees of asymmetry is shown in Figure 5.7(c) (see

the Appendix A.1). The resonance becomes sharper as we reduce the asymmetry and finally disappears from the spectrum for a perfectly symmetric structure. The BIC mode is characterized by the fact that for zero asymmetry, it has an infinite Q factor and hence cannot be detected in the spectrum. The presented approach is based on the solid foundation established by previous works reported in this field. To convey the improvement in the Q factor observed in the current study, we have presented a comparison in Table 5.2, which shows an enhancement in the excitation of the Q factor compared to earlier studies.

Table 5.2: Comparison with already reported works

Reported Works	Reported Q factor	Frequency range	Year
[110]	24 (simulation)	THz	2024
[100]	24 (simulation), 21 (experimental)	THz	2022
[99]	30.5 (simulation)	THz	2020
[98]	27.5 (simulation)	THz	2011
This work	107 (simulation)	THz	2024

5.6 Sample characterization in terahertz time domain spectroscopy

Metasurfaces were fabricated for three degrees of asymmetries δ = 0, 20.5%, 29.4%. The transmission amplitude of the proposed metasurface is measured using an in-built fiber-coupled terahertz time-domain spectroscopy setup (THz-TDS) in a dry environment with humidity less than 14%. Figure 5.8 presents the schematic of the fiber-coupled in-built THz time-domain spectroscopy setup. The characterization setup consists of a photoconductive-based THz transmitter and a THz receiver with a pair of identical gold-coated parabolic mirrors. The metasurface sample is placed in the focal plane of the parabolic mirrors to ensure minimal spatial dispersion of the incidence [**?**]. An array size of approximately 1 cm × 1 cm is fabricated to assure excitation homogeneity. The transmitted time-domain signal is transformed to the frequency domain through Fourier transformation and normalized with an identical bare quartz substrate as a reference, $T(\omega) = \frac{E_s(\omega)}{E_r(\omega)}$, where $E_s(\omega)$ and $E_r(\omega)$ are the Fourier-transformed frequency domain transmission spectra of the sample and the bare quartz substrate, respectively.

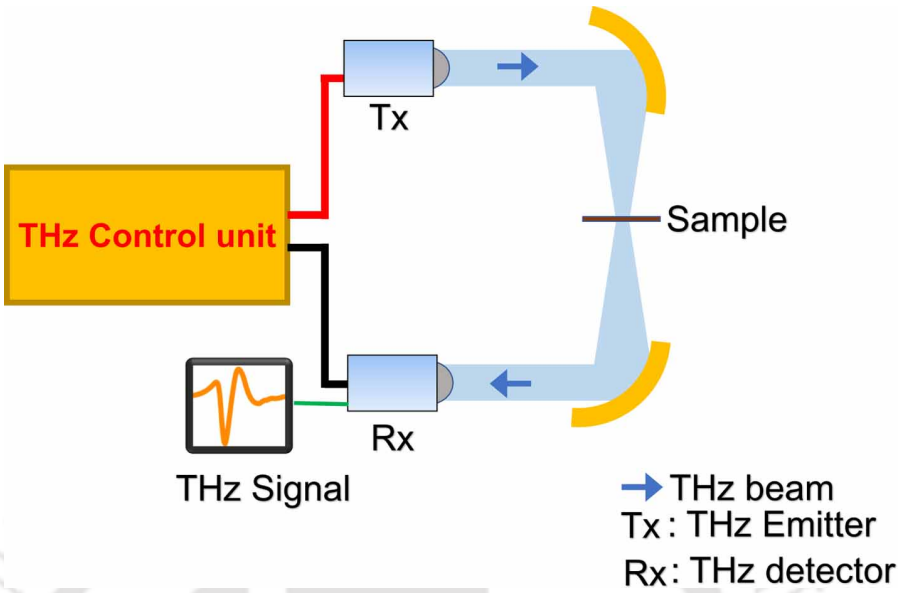

Figure 5.8: The fiber-coupled THz time-domain setup focuses the transmitted THz radiation to a beam spot size of 8 mm using a parabolic mirror with a focal length of 10 cm. The focused THz beam is passed through a metasurface sample area of 1 cm × 1 cm and is then detected by the detector.

The transmission spectra were measured for three samples with different degrees of asymmetries. The results show a signature of the quasi-BIC resonant response and demonstrate good agreement between the resonance frequencies of the simulated and experimental results. Figure 5.9(a) presents the transmission spectrum obtained from the symmetrical metasurface configuration, revealing a distinct resonance dip at 1.1 THz, matching the simulation predictions. However, the discrepancies in the observed linewidth and amplitude compared to simulations are likely due to edge scattering losses and inevitable fabrication inaccuracies. Figures 5.9(b) and 5.9(c) illustrate the measured transmission spectra corresponding to structural asymmetries $\delta = 20.5\%$ and $\delta = 29.4\%$. The results show a clear signature of the quasi-BIC resonance mode at 0.7 THz as the asymmetry is introduced. Since the results correspond to an asymmetry degree of 29.4%, showing a prominent dip, we have calculated the experimental and simulated Q factors for this asymmetry for comparison (see appendix A.1 for details). The experimentally determined Q factor is 5.96, whereas the simulated Q factor is 33.7. This mismatch between the simulation and experimental result is mainly due to the experimental setup's minimum resolution limit, which is insufficient to resolve a resonance with ultra-narrow linewidth.

Moreover, the quartz substrate with a thickness of 500 μm is used as mechanical

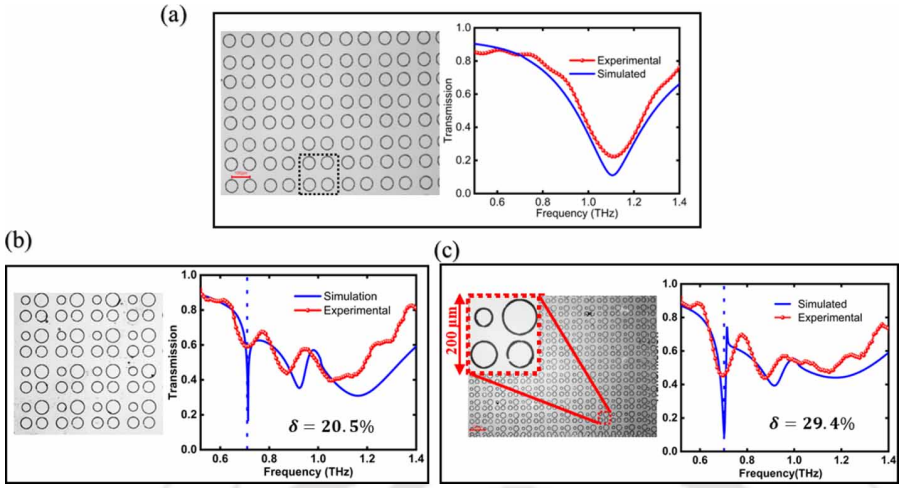

Figure 5.9: Micrograph image and experimentally measured transmission spectrum for (a) symmetric structures, (b) with structural asymmetry $\delta = 20.5\%$, (c) with structural asymmetry $\delta = 29.4\%$, fabricated using photolithography.

support for the metasurface design, producing an etalon effect due to the reflection from the incident surface. The presence of the etalon pulses creates a noisy oscillation in the time-domain transmission spectrum. The sharp resonance dip somewhat loses its existence as a cumulative effect of the limited resolving power and the etalon effect. To avoid this etalon effect, the data have been truncated before the emergence of etalon noises. However, a finite amount of information is lost due to this effect, which causes an observable mismatch between the simulation and experimental results.

5.7 Analysis of the field distribution by using near-field scanning terahertz microscopy

We further experimentally investigated the near-field distribution of the electric field associated with the resonance mode of the fabricated metasurface sample.The near field measurement is performed using a near-field scanning terahertz microscopy (NSTM) setup. Figures 5.10(a) and 5.10(b) show the normalized $|E_z|$ electric field distribution mapped over an area of 400 μm × 400 μm, with the measurements on the left panel and simulated results on the right panel. The simulated near-field distributions are accurately reproduced in the experimental $|E_z|$ field distribution associated with the quasi-BIC mode at a frequency of 0.71 THz.

The working principle of the NSTM setup is similar to that of a conventional THz-

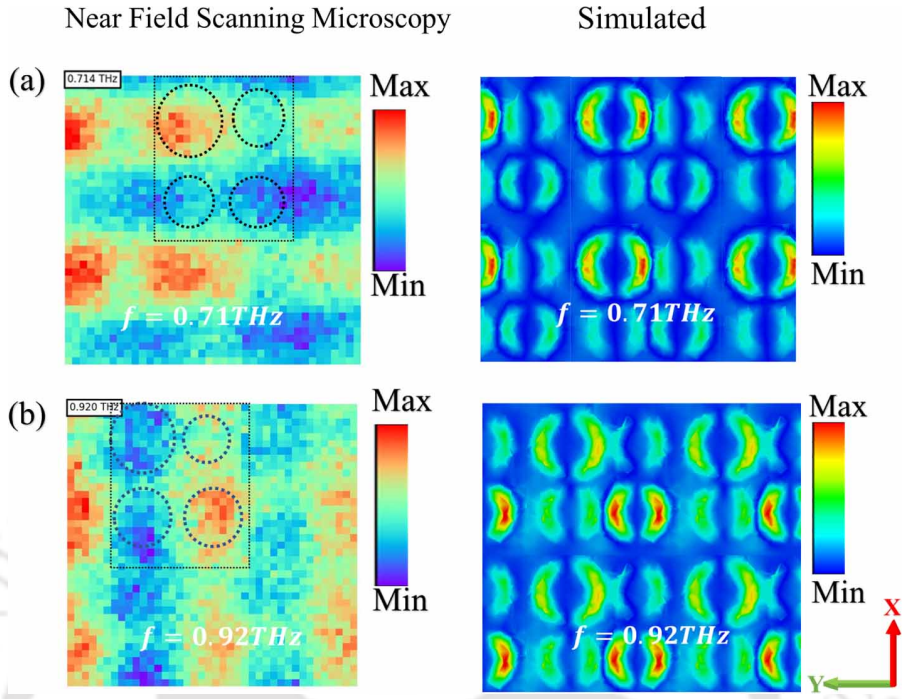

Figure 5.10: The measured near-field scanning microscopy image and simulated $|E_z|$ field distributions of the metasurface with asymmetry $\alpha = 29.4\%$ at frequencies (a) $f = 0.71$THz and (b) $f = 0.92$THz. The field distributions are scanned and calculated at 10 μm above the metasurface. The ring resonators are highlighted with black dashed circles.

TDS system (For details, see figure A3 in the appendix A.2). A 35 fs optical pulse, with an 800 nm central wavelength, from a Spectra-Physics MaiTai laser is split to generate a single-cycle THz pulse using a photoconductive antenna (BATOP GmbH), and the THz pulse is detected using a polarization-sensitive, micro-structured photoconductive antenna-based THz microprobe (Protemics GmbH). The generated terahertz beam is focused on the tip using off-axis parabolic mirrors. The sample is mounted on an XYZ motorized stage to construct the spatial profile.

The transient THz electric field mapping in the temporal domain is performed using a delay line. The current induced in the microprobe due to the THz electric field is amplified (using a trans-impedance amplifier) and detected using the standard lock-in measurement technique (SR865). The THz microprobe was placed 10 μm ($< \frac{\lambda}{10}$) above the metasurface for this measurement. An area of 400 μm $\times$ 400 μm was scanned around a meta-molecule with a step of 10 μm. The measured spatio-temporal THz electric field distribution is then Fourier transformed to the frequency domain to obtain the electric field profile at different frequencies.

Due to the spatial resolution limitation of the microprobe, the measured field profiles

appear convoluted compared to the profiles obtained in the simulation.

5.8 Summary

We have reported a robust high-quality quasi-Bound State in the Continuum (quasi-BIC) mode with a ring-shaped metamolecule system operating in the terahertz (THz) frequency range. By innovatively breaking the structural symmetry of the metamolecule system in a non-uniform or selective manner, we effectively reduced the radiation density, resulting in a high-Q quasi-BIC resonance that surpasses the Q factors achieved by conventional uniform symmetry-breaking approaches.

Our strategy involves selectively perturbing only half of the resonators within the metamolecule, which minimizes radiative losses more effectively than uniformly breaking the symmetry of all resonators. This selective symmetry-breaking leads to a significant enhancement in the Q factor from 25.8 to 107, as demonstrated by both simulation and experimental results. The Q factor and the resonance frequency can be tuned by adjusting the geometrical degree of asymmetry, providing a versatile platform for manipulating resonant properties in metamaterials.

The terahertz time-domain spectroscopy (THz-TDS) and near-field scanning terahertz microscopy (NSTM) results, validate the theoretical predictions and numerical simulations. The measured transmission spectra exhibit good agreement with the resonance frequencies of the simulated transmissions. The experimentally determined Q factor of the metasurface with an asymmetry of 29.4% is found to be 5.96, whereas the simulated Q factor is 33.7. This discrepancy arises due to the resolution limit and data truncation during analysis. Additionally, the NSTM results show a strong correlation with the simulated near-field distributions at the quasi-BIC mode, providing firm support for the observation of the quasi-BIC mode. The excellent agreement between the analytical modeling based on Gallinet and Martin's *ab initio* theory and the simulation results further validates the bright-dark coupling mechanism responsible for the Fano resonance observed in the system. This method shows a higher Q factors than the conventional symmetry breaking approach. This kind of simple, yet effective method can open new avenues for the exciting field of applications like sensing and nonlinearity in the THz frequency range.

CHAPTER 6

EXCITATION OF QUASI-BIC MODE IN A LATTICE PERTURBED THZ SPLIT RING RESONATOR METAUSRFACE

6.1 Introduction

In continuation with the selective symmetry-breaking approach discussed in the previous chapter, here we have explored an alternative way other than the mirror symmetry-breaking approach. This chapter presents a theoretical demonstration and experimental validation of quasi-BIC excitation in the metallic split-ring resonator (SRR) metasurfaces by perturbing the lattice constant.

Split ring resonators (SRRs) have been extensively studied owing to their unique ability to support magnetic resonances and their utility in analyte sensing. Earlier studies reported sharp Fano resonance modes in SRR metamaterials by exploiting mirror symmetry-breaking effects [112]. For instance, Singh *et al.* numerically and experimentally investigated the excitation sharp Fano resonances with high Q factor and its tunability by varying the degree of asymmetry in asymmetric split ring resonator [113]. The excitation of quasi-BIC resonance modes by structural symmetry breaking

Part of the results of this Chapter have been published in the following papers: Bhairov Kumar Bhowmik, K M Rohith, and Gagan Kumar, "Excitation of High-Quality Quasi-BIC toroidal Mode in a Lattice perturbed terahertz Metasurface." (accepted)Applied Physics Letter, 2024.DOI:10.1063/5.0228324

in metasurface unit cell designs has been a key idea due to its simplicity and the tunability of the Q-factor via structural asymmetry [4]. Some recent studies have explored alternative methods to achieve coupling-assisted high-Q resonances. In this context, Xu *et.al* investigated excitation of sharp high Q mode by direct coupling between intrinsic radiative modes and lattice modes of SRR [114]. In line with this, a significant enhancement of Q-factor have been reported by coupling the fundamental lattice mode of a metasurface array with a symmetry-protected BIC-assisted Fano resonance [116]. Additionally, manipulating periodicity in supercells and using mirrored asymmetric resonators have been demonstrated to significantly enhance Q-factors by supporting subradiant LC modes[117].

Wang *et al*. recently demonstrated the excitation of quasi-BIC modes in all-dielectric metasurface arrays by leveraging band folding induced through perturbations in the lattice constant[43]. This recent advancement suggests the potential to excite quasi-BIC resonance modes in the metallic split-ring resonator (SRR) metasurfaces at terahertz frequencies. Despite the recent progress, the research work that explores such a mechanism using simple SRR structures in the terahertz domain is very limited. We explored the lattice perturbed effect in the split ring resonator metasurface by addressing this gap. By strategically perturbing the inter-spacing between adjacent SRR pairs, we effectively double the lattice constant of the unit cell, leading to Brillouin zone folding along the X-direction. This perturbation induces the emergence of BIC modes at the Γ point. The near-field distributions and the surface current profile of the resonance mode depict the toroidal nature of the excited mode.

The chapter is organized as follows: Section 6.2 outlines the simulation optimization and fabrication of the metasurface. Section 6.3 discusses the transmission response and the toroidal nature of the resonance mode. In Section 6.4, the quasi-BIC characteristic of the resonance mode is described. Section 6.5 explains the role of the coupling mechanism in the excitation of the BIC mode. Section 6.6 presents the evolution of the BIC into a quasi-BIC mode, along with the experimental characterization of the metasurface sample. Finally, Section 6.7 gives a summary of the major findings from the chapter.

6.2 Design and fabrication of the metasurface

As shown in Fig 6.1, the proposed metasurface unit cell consists of a pair of two adjacent split ring resonators on the top of a quartz substrate. Figure 6.1 shows the schematic of

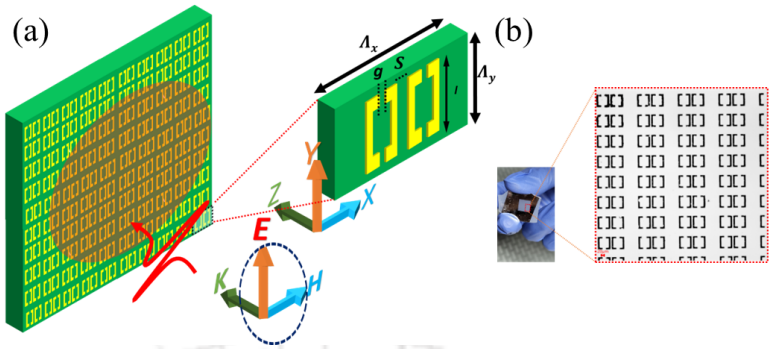

Figure 6.1: (a) Schematic representation of the optimized planar terahertz double split ring resonator metasurface design on the quartz substrate. Here, the geometrical parameters are, periodicity $\Lambda_x = 200\mu m$, $\Lambda_y = 100\mu m$, length of the square SRR, $l = 65\mu m$, split gap, $g = 16\mu m$ and S represents the perturbed interspacing between two SRR. (b) The fabricated metasurface sample using photolithography in clean room ambiance.

the metasurface with the optimized geometrical parameters: periodicity. $\Lambda_x = 200\mu m$, $\Lambda_y = 100\mu m$, length $l = 62\mu m$, split gap $g = 16\mu m$ and a perturbed separation $\Delta S = S_0 - S = 10\mu m$. Here, S_0 is the separation between two adjacent SRR for unperturbed case (**See appendix A.4**). The gap between the two adjacent SRRs for the unperturbed case is $S = S_0 = 38\mu m$. In such cases, the unit cell (meta-atom) represents a single SRR. The perturbation of the interspacing distance disrupts the lattice constant of the metasurface along the X direction, leading to the doubling of the structure's lattice constant, as shown in the inset of Fig.6.2(b). Accordingly, the corresponding first Brillouin Zone is folded in $\Gamma - X$ direction as shown in **appendix Fig A.6**. The folding of the band due to the lattice perturbation induces the emergence of BIC mode at Γ point (See supplementary information for details). Finite Integration Technique based on commercially available CST microwave studio suite software is used to simulate the metasurface's transmission and near-field distributions. Boundary conditions are chosen as unit cell in the X, Y directions, and it is kept as open in the Z direction. An add-space is introduced along the source port to prevent unnecessary reflections into the simulation domain.

6.3 Transmission of the metasurface and analysis of the toroidal behaviour

Figure 6.2 presents the simulated transmission spectra demonstrating the effects of geometrical perturbations on a metasurface composed of SRRs. Figure 6.2 (a) illustrates

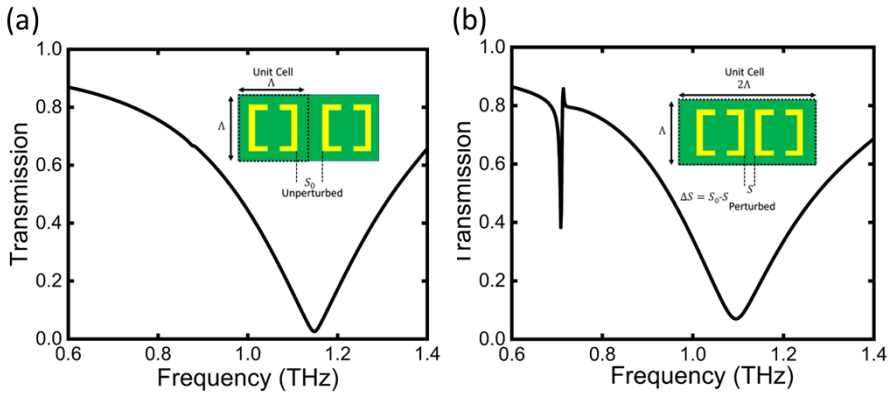

Figure 6.2: Simulated transmission spectra for the(a) unperturbed case, the separation between the two adjacent SRR is $S = 38\mu m$, (b) perturbed case, when the interspacing between the two adjacent SRR is changed by $\Delta S = 10\mu m$. The change in separation leads to periodicity doubling, as shown in the inset. The unit cell is shown as a dashed marking for a clear view.

the transmission spectrum for the unperturbed case, where the separation between two adjacent SRRs is set at $38\mu m$. Figure 6.2(b) shows the transmission spectrum for the perturbed case, where the gap between two adjacent split-ring resonators (SRRs) decreased by $28\mu m$, resulting in a new gap of $10\mu m$. A broad resonance dip appears in the transmission spectrum without any perturbation effect, but an additional asymmetric sharp resonance mode at frequency 0.71 THz appears in the spectrum as the gap perturbation ΔS is introduced in the structure. To get an in-depth idea of the type of electromagnetic mode at the resonance frequency, we have simulated the near-field distributions of the magnetic field and electric field at the resonance frequency.

Fig 6.3(a) presents the Z component of the magnetic field at the sharp resonance frequency; the field is calculated exactly at the top of the resonator. The positive and negative value of the H_z component at the interior of the two adjacent SRR indicates that the field is inward in one SRR and it is outward in another SRR. The arrow plot of the magnetic field (as shown in Fig 6.3(b)) is calculated on XZ plane at y=0. The arrow plot clearly shows that the magnetic field direction is outward in the right SRR, and it is inward in the left adjacent SRR. This indicates a pair of anti-aligned magnetic dipoles. To further see the evidence of this effect, we have calculated the surface current distribution of the planar metasurface design (as shown in Fig 6.3(c)). In Fig 6.3(c) the surface currents are distributed with opposite flowing directions in the two adjacent SRR. This is consistent with the Hz component of Fig 6.3(a) induced by the surface current. The magnetic field generates a closed loop in the middle of the two adjacent SRRs and thus

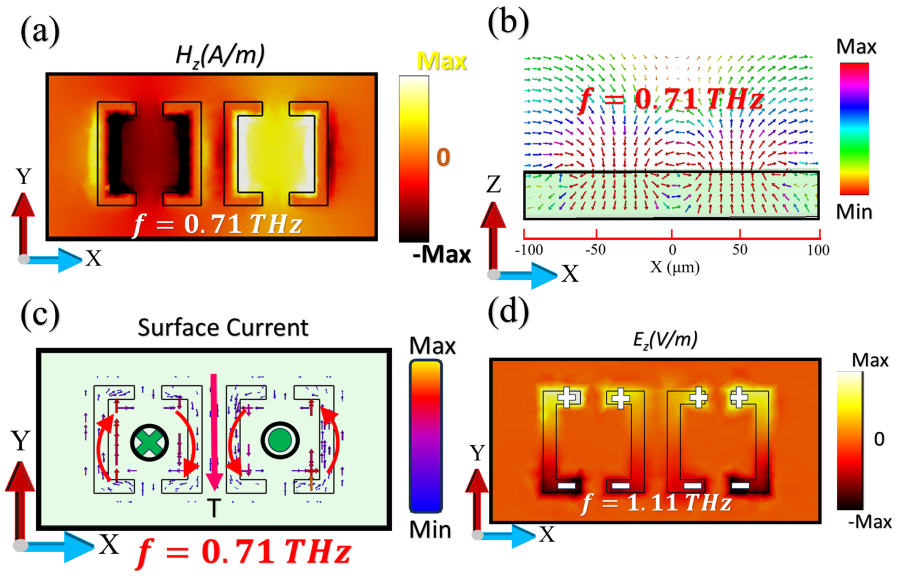

Figure 6.3: The simulated (a) near field distributions of the Z component of the magnetic field (the field monitor is exactly top of the resonator), (b) the magnetic field arrow plot in the XZ plane, and (c) surface current profile at the sharp Fano resonance dip of frequency 0.71 THz. (d) Simulated E_Z field distributions at the broad resonance dip of $f = 1.11THz$, the plus and minus signs show the corresponding charge distributions.

creates a toroidal dipole along the -Y direction (**see appendixA.7**). To reveal the nature of the broad resonance dip, we have simulated the electric field distributions at frequency 1.11 THz. The field profile indicates the excitation of two parallel electric dipoles at the resonance dip (as shown in Fig 6.3(d)). The sharp quasi-BIC Fano resonance appears in the spectrum due to the destructive interference between the broad radiative dipole and dark toroidal mode.

6.4 Quasi BIC characteristic

We performed an eigenmode analysis of the proposed metasurface to get a deeper insight into the resonance mode's BIC nature. The quality factor of the mode (as shown in Fig 6.4) shows a diverging nature as we deviate from the Γ point (K=0) in the first reduced Brillouin zone. Since the quasi-BIC mode is excited as a result of the doubling lattice constant, we examine the fundamental lattice mode of the metasurfaces to get an insightful understanding. The lattice mode frequency given by [116],

$$f_{L(1,0)} = \frac{C}{n_s P}\sqrt{i^2 + j^2} = \frac{C}{n_s P}$$

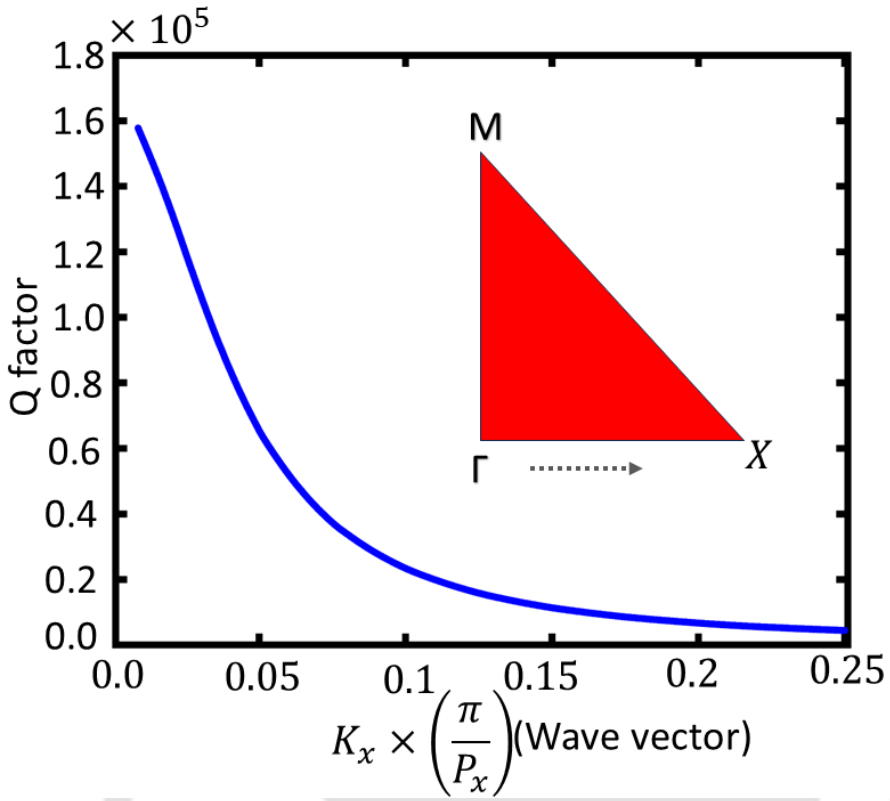

Figure 6.4: The calculated normalized wave vector versus Q factor plot using eigenmode solver. The inset shows the position of symmetry points of the first reduced Brillouin zone. The Q factor decays in the reciprocal space and attains a very high value at Γ point.

, where c is the speed of light in vacuum, n_s is the refractive index of the substrate material, and (i, j) is the order of the lattice mode. For our case this frequency turns out to be 0.717 THz. The predicted lattice mode frequency matches the observed quasi-BIC resonance mode. The otherwise dark lattice mode couples to the continuum (bright) as a result of the perturbation of interspacing between the SRRs, which doubles the lattice constant.

6.5 The role of coupling mechanism in BIC excitation

6.5.1 Analysis of the coupling using Gallinet and Martin's ab initio Fano theory

It is already evident from Fig6.2(b) that the sharp resonance response is associated with an asymmetric line shape, which bears a hallmark for its Fano nature. So, to validate

the Fano nature and to understand the underlying physics, we adopted Gallinet and Martin's ab initio theory of Fano resonance[109]. Fano-like resonances arise from the spectral and spatial overlap between a nonradiative (dark) mode and a continuum, leading to interference effects. According to ab initio theory, the spectral line shape of the asymmetric discrete lineshape can be obtained as:

$$I_d = \frac{(\Omega + q)^2 + b}{\Omega^2 + 1} \tag{6.1}$$

$$\Omega = \frac{\omega^2 - \omega_d^2}{2W_d\omega_d} \tag{6.2}$$

where, ω_d is the resonance frequency of the dark resonance mode, Wd gives an approximation of its spectral line width in frequency units for $W_d \ll \omega_d$, q is the asymmetry parameter, and b is the modulation damping parameter quantifying the intrinsic loss effect. The radiation continuum mode, which acts as a background of such Fano resonance mode, can be expressed as a Lorentzian pseudo symmetric line shape function

$$I_b = \frac{A^2}{\left(\frac{\omega^2 - \omega_b^2}{2W_b\omega_b}\right)^2 + 1} \tag{6.3}$$

here, A is the maximum amplitude at the resonance frequency, and W_b gives the spectral linewidth in terms of the frequency unit for $W_b \ll \omega_b$.

The measurable quantity or the resonance strength of the system collectively can be expressed as, $T = 1 - (I_a \times I_b)$, this expression can be used to fit the simulated transmission spectrum of the proposed metasurface design. Figure 6.5 depicts the simulated and analytically fitted plot asymmetry for asymmetry, $\delta = \frac{\Delta S}{S_0} = 0.84$. The blue curve indicates the result obtained using CST simulation method and the red curve shows the results obtained using the Fano theory. The details of the fitting and extracted parameters can be found in the Supplementary Materials. The consistency between the simulation and analytical result indicates that it is justifiable to attribute the role of bright (continuum) and dark(discrete) interference to generate the sharp resonance mode. The further decomposition of the bright and dark mode line shape can be seen in the **appendixA.3**.

6.5.2 The coupled harmonic oscillator model

To reveal the in-depth understanding of the coupling mechanism and its variation with geometrical parameter ΔS, we employed the coupled harmonic oscillator model to mimic

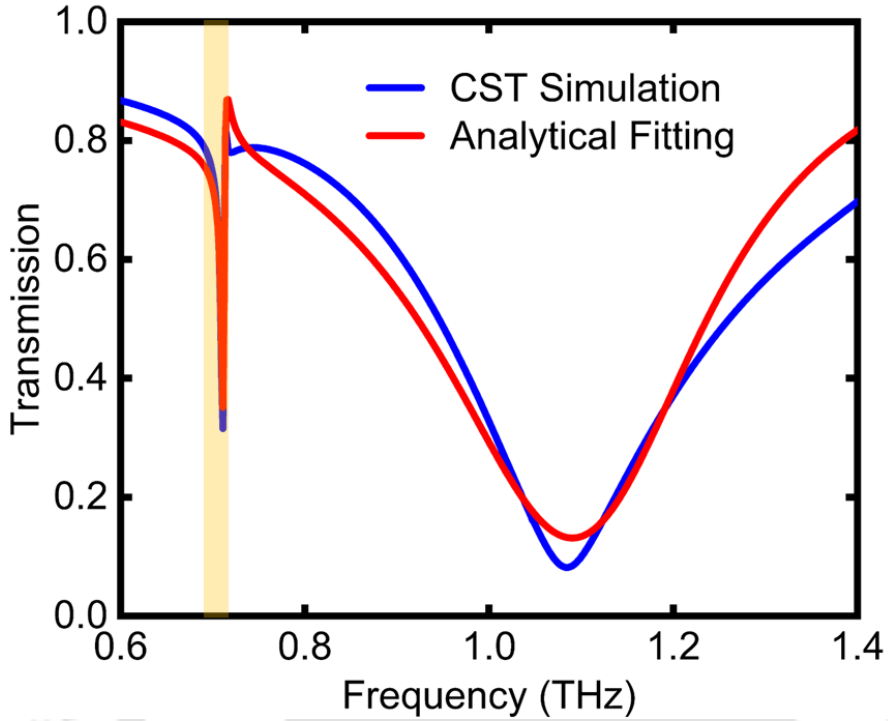

Figure 6.5: The simulated transmission amplitude (blue) and analytically fitted transmission using Fano theory for $\Delta S = 32\,\mu$m; asymmetry $\delta = \frac{\Delta S}{S_0} = 0.84$.)

the manifestation of quasi-BIC mode as Fano resonance in the transmission spectrum. The coupling between dark (nonradiative) and bright (radiative) modes in a system under the excitation of incident THz wave $E_0 e^{-i\omega t}$ can be expressed by the following equations:

$$\ddot{x}_b(t) + \gamma_b \dot{x}_b(t) + \omega_b^2 x_b(t) + K^2 x_d(t) = \frac{qE_0 e^{i\omega t}}{m}$$

$$\ddot{x}_d(t) + \gamma_d \dot{x}_d(t) + \omega_d^2 x_d(t) + K^2 x_b(t) = 0$$

Where, (x_b, x_d);$(\gamma_b, \gamma_d\ )$;(ω_b, ω_d) are the amplitude of the oscillation, decay rate, and resonance frequency of the bright (radiated) mode and dark mode. K represents the coupling strength of the dark mode to the bright mode. As a result of the coupling, the quasi-BIC mode appears embedded in the broad dipole resonance mode. q and m are the effective charge and mass of the radiative mode that indicates the effective coupling of the radiative mode to the incident THz radiation. The dark mode (the nonradiative mode) is completely decoupled from the free space radiation. The effective coupling strength can be extracted by fitting the transmission obtained by this model to the simulated result. By solving the above two coupled equations, the expression for susceptibility can

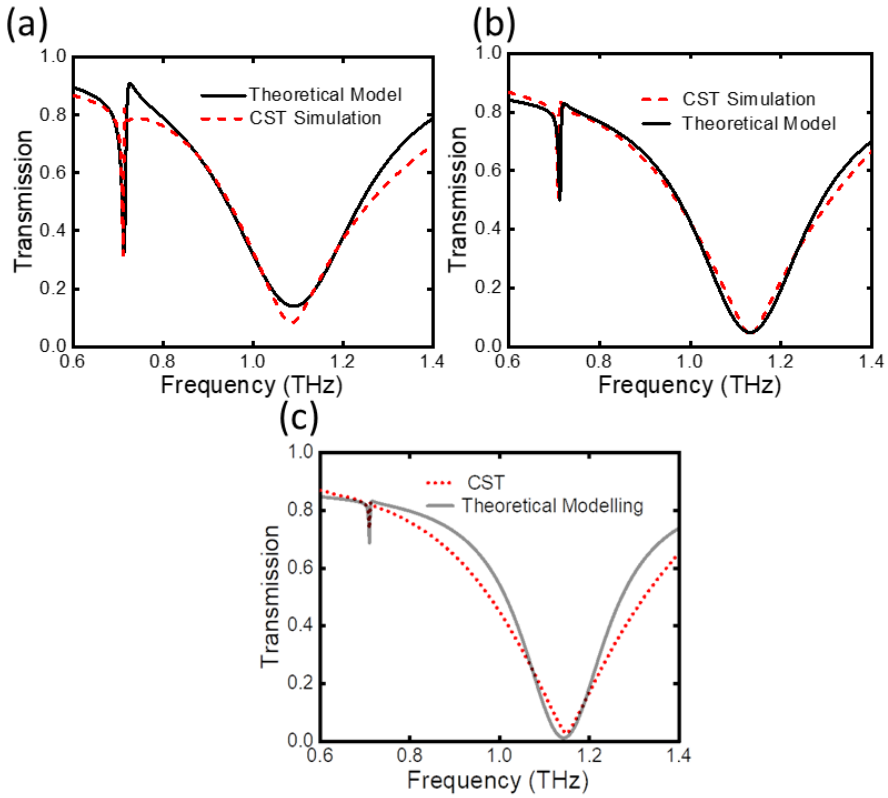

Figure 6.6: Transmission spectrum of the metasurface for different gap perturbation (a) $\Delta S = 32\mu m$, (b) $\Delta S = 16\mu m$, and (c) $\Delta S = 8\mu m$. (Black solid line: Simulation, red dashed line: coupled harmonic oscillator model.)

be written as:

$$\chi = M \frac{(\omega^2 - \omega_d^2 + i\omega\gamma_d)}{K^4 - (\omega^2 - \omega_d^2 + i\omega\gamma_d)(\omega^2 - \omega_b^2 + i\omega\gamma_b)}$$

where, M is the constant of proportionality. The analytical expression for the transmission can be obtained as $T = 1 - Im(\chi)$. Fig 6.6 (a), (b), and (c) show the evolution of the quasi-BIC resonance mode with the gap perturbation $\Delta S = 32, 16 and 8\mu m$, respectively. The transmission plot shows a good agreement with the simulated results. The extracted fitted parameters are tabulated in Table 6.1.

Table 6.1: Extracted parameters

ΔS	γ_b (rad/ps)	γ_d (rad/ps)	ω_b (rad/ps)	ω_d (rad/ps)	K (rad/ps)
8 μm	0.25	0.0024	1.16	0.714	0.23
16 μm	0.27	0.0036	1.14	0.715	0.29
32 μm	0.3	0.005	1.1	0.72	0.35

The coupling coefficient, as well as the decay rate γ_d, decreases as the gap pertur-

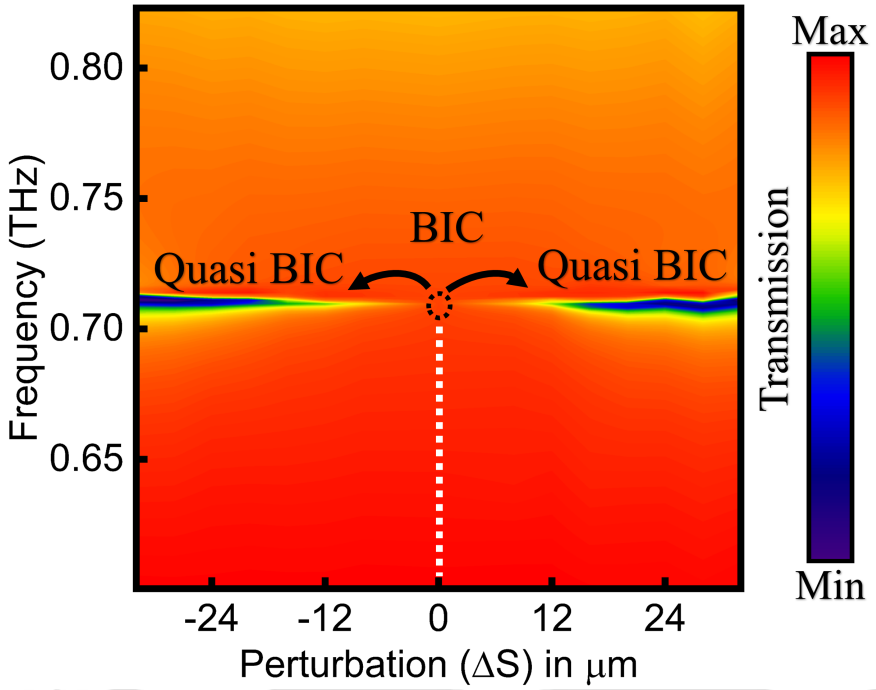

Figure 6.7: The appearance of Quasi BIC mode when the separation between the pair of SRR is changed. White dashed line indicates the position of ideal BIC mode.

bation decreases. This indicates that the gap perturbation introduces a leaky channel to couple with the free space radiation continuum. The intensity of the Fano resonance depends on the strength of the coupling coefficient and is related to the geometrical gap perturbation introduced in the metasurface.

6.6 Evolution of the quasi BIC mode and experimental characterization

To analyze the dependency of the sharp resonance mode on the perturbation, we simulated the transmission for different separation gap perturbations ΔS. Fig6.7 depicts the contour plot of transmission as a function of frequency for different perturbations (ΔS). The sharp resonance mode shows an almost stable spectral position under the perturbation and disappears for the intrinsic separation or unperturbed case $\Delta S = S_0 - S = 0$, marked by a black dashed circle in Fig 6.7. S_0 is the separation between two adjacent SRR when the lattice constant is unperturbed, and the unit cell consists of a single SRR. The ideal BIC mode evolves into quasi-BIC mode and manifests as a sharp asymmetric

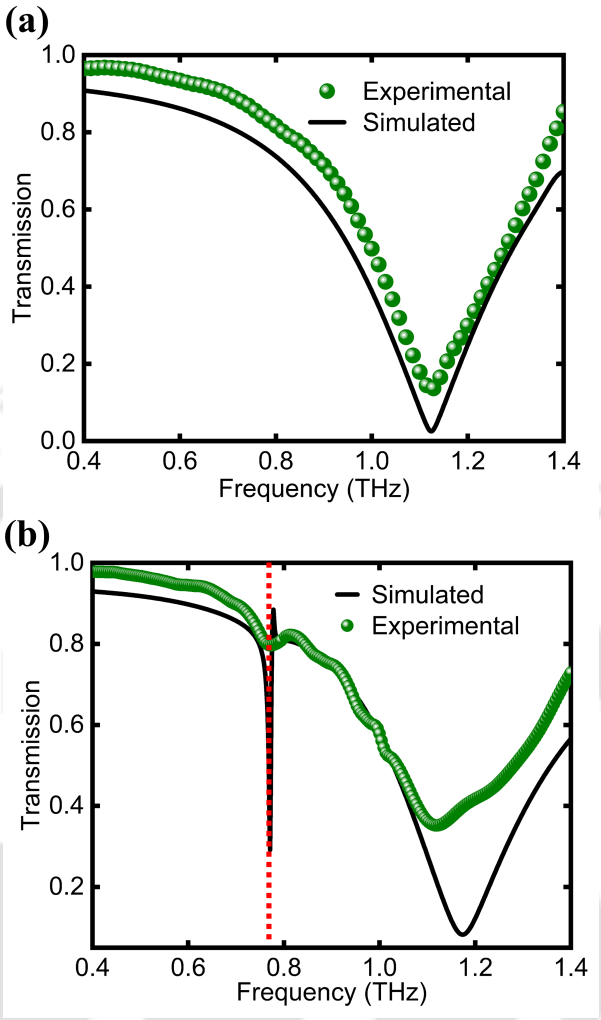

Figure 6.8: (a) Simulated and Experimentally measured transmission amplitude for the (a) unperturbed $\Delta S = 0$, and (b) perturbed metasurface with $\Delta S = 32\mu m$.

resonance as the interspacing between two SRR deviates from the unperturbed or intrinsic separation value $S_0 = 38\mu m$. The spectra are gradually broadened as $|\Delta S|$ increases, indicating the diverging nature of the Q factor. Figure 6.8(a) and (b) show the simulated (solid black line) as well as measured (green spheres) transmission amplitude for the metasurface design with unperturbed $\Delta S = 0$ and perturbed $|\Delta S| = 32\mu m$. Figure 6.8(a) and (b) show the simulated (solid black line) as well as measured (green spheres) transmission amplitude for the metasurface design with unperturbed $\Delta S = 0$ and perturbed $|\Delta S| = 32\mu m$. The measured spectra show a good matching with the simulated spectrum for the symmetric case. In the perturbed case (Fig 6.8(b)) the measured result shows a good signature of the existence of the quasi-BIC mode, however, there is a mismatch

in the resonance strength as well as linewidth of the sharp quasi-BIC mode due to the resolution limit of the THz time domain spectroscopy set-up.

6.7 Summary

This chapter presents the excitation of the sharp toroidal quasi BIC mode by perturbing the lattice constant. The magnetic field distribution and surface current profile show the toroidal behaviour of the excited mode. The eigen mode spectrum analysis shows the divergence of the Q factor at Γ point, which signifies the symmetry protected quasi BIC nature of this mode. For an in-depth understanding of the role of bright dark coupling mechanism the Gallinet and Martin's ab initio theory and the coupled harmonic oscillator model have been employed. Experimental results shows a signature response of the predicted quasi BIC mode. The measured transmission response shows a consistency with the simulated quasi BIC mode. This approach shows a spectrally stable quasi BIC mode over the induced asymmetry parameter. This work can lead to a significant improvements in device performance, including enhanced sensing capabilities, more efficient filters, and higher resolution terahertz imaging.

CHAPTER 7

SUMMARY AND FUTURE DIRECTION

Metamaterials, particularly metasurfaces, have become efficient platforms for manipulating and tailoring electromagnetic responses at sub-wavelength dimensions. The inherently sub-wavelength dimension of metasurfaces makes it promising for compact on-chip photonics applications. The first part of this thesis focused on demonstrating efficient narrow pass band filters and sensors in the near-infrared (NIR) range. By leveraging the high Q nature of the excited resonance, we achieved optimized designs with enhanced performance metrics suitable for filtering and sensing applications.

The latter part of the thesis presents a scientific exploration of new methods to excite high-Q quasi-bound states in the continuum (quasi-BIC) modes in terahertz (THz) metasurfaces. As terahertz technology advances, there is a growing demand for low-loss, high-Q metasurface-based devices. In line with this, our work significantly contributes to ongoing research by introducing efficient, low-radiative-loss metasurface designs in the terahertz domain. We explored the quasi-BIC mode excitation in the terahertz region using two approaches: selective symmetry breaking and lattice-induced band folding mechanism.

In Chapter 1, we provided a comprehensive explanation of the bound state in the continuum, including its different types and excitation in the metasurface. Additionally, the chapter gives an introduction to the concept of metamaterials and metasurfaces, covering the fundamental resonant behaviour of terahertz split ring resonator metasurface. The chapter also presents a literature survey on the excitation of the quasi BIC mode in

terahertz and near-infrared C band region primarily by symmetry breaking approach.

Chapter 2 provides a detailed discussion of simulation methodology and clean room fabrication process using photo-lithography. The characterization of the metasurface sample using terahertz time domain setup is discussed briefly.

In Chapter 3, we designed and analyzed an all-dielectric metasurface-based narrow bandpass filter operating in the near infrared communication band (1530–1565 nm). The filter exhibits an ultra-narrow full width at half maximum (FWHM) of 0.31 nm and a high Q-factor of approximately 5140 at the resonance wavelength of 1549.8 nm. The sharp resonance was excited exploiting the symmetry-breaking approach, and the electric field distribution resembled a coupled quadrupolar distribution. The dependency of the resonance mode on the asymmetry shows a quasi-BIC like behaviour. We employed the multipolar decomposition theory to further analyse the behaviour of the resonance mode. The metasurface based filter shows passive tunability in the entire C band region.

In chapter 4 we demonstrated a dual parametric sensing mechanism utilizing an asymmetric all-dielectric metasurface. The high Q-factor of 2.8×10^4, combined with Fano resonance behavior, makes this design highly suitable for efficient sensing application. The resonance wavelength shifted with changes in the refractive index of background medium and temperature, demonstrating its use as a refractive index and temperature sensor. The calculated sensitivity reached 140 nm/RIU with a Figure of Merit (FoM) of 5384 RIU^{-1}, while temperature sensitivity was found to be 72 pm/°C. This design holds promise for biomedical sensing and environmental monitoring.

In chapter 5 we discussed on the excitation of a high-quality factor quasi-BIC mode in a metallic ring-shaped metamolecule system operating in the terahertz frequency range. By selectively breaking the symmetry of the unit cell, we achieved a substantial enhancement in the Q-factor, increasing it from 25.8 to 107. This selective perturbation approach minimizes radiative losses more effectively than uniform symmetry breaking. Terahertz time-domain spectroscopy (THz-TDS) and near-field scanning terahertz microscopy (NSTM) confirmed the theoretical and simulation results. The higher Q-factors achieved through this method present exciting opportunities for terahertz sensing and nonlinear applications.

In Chapter 6, we explored the excitation of a sharp toroidal quasi-BIC mode by perturbing the lattice constant of the metasurface. The toroidal nature of the resonance mode is confirmed by magnetic field distributions and surface current profiles. The eigenmode spectrum analysis revealed a divergence of the Q-factor at the Γ point, which

predicts the quasi-BIC nature of the mode. Both Gallinet and Martin's ab initio theory and the coupled harmonic oscillator model were used to understand the role of the bright-dark coupling mechanism for the excitation of the quasi-BIC mode. The experimentally measured transmission spectrum shows a signature response to the predicted quasi-BIC mode.

7.1 Future scope

Recently, the excitation of high-quality factor quasi-BIC resonances in planar metasurfaces has emerged as a promising topic. The work done in this thesis offers the next ground for studies of quasi-BIC mode in a metasurface. In this thesis, we developed an optimized all-dielectric metasurface-based ultranarrow bandpass filter. This can be further explored experimentally by fabricating the device using clean room nanofabrication tools. The dynamic tunability of the proposed filter design can be explored by integrating phase-change materials such as germanium-antimony-telluride (GST) or liquid crystals.

In this study, the excitation of sharp quasi-BIC mode using a selective symmetry-breaking approach was reported. There is a scope to further optimize a design that shows a polarization and incidence angle-independent response to some extent. By incorporating active 2D materials such as vanadium dioxide (VO_2), the designs can be made actively tunable. The VO_2 shows a phase transition from insulating to metallic at a particular transition temperature; by leveraging these features, the metasurface response can be modulated to a great extent.

The investigation of lattice-induced toroidal quasi-BIC modes can be extended to explore multiple BIC modes and their dynamic tunability across the THz spectrum. In addition to this, further design optimization to incorporate polarization insensitivity would provide greater flexibility and enhance the potential of the design for practical application.

APPENDIX A

APPENDIX: SUPPLEMENTARY INFORMATION

A.1 Fano fitting

We have calculated the Q factor for the metasurface with different asymmetries as depicted in Figure S1. In this method, we have used the Fano fit formula:

$$T_{\text{Fano}} = \left| a_1 + ia_2 + \frac{b}{(\omega - \omega_0 + i\gamma)} \right|^2$$

where a_1, a_2, and b are real constant numbers, ω_0 is the resonant frequency, and γ is the overall decay rate of the resonance. The Q factor is calculated using the following formula from the extracted fitting parameters:

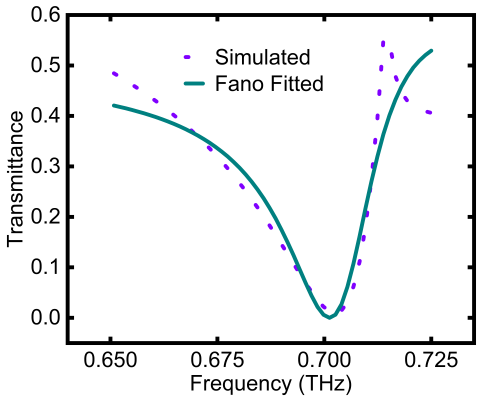

Figure A.1: The Fano fitted plot with the simulated data for the Q factor extraction.

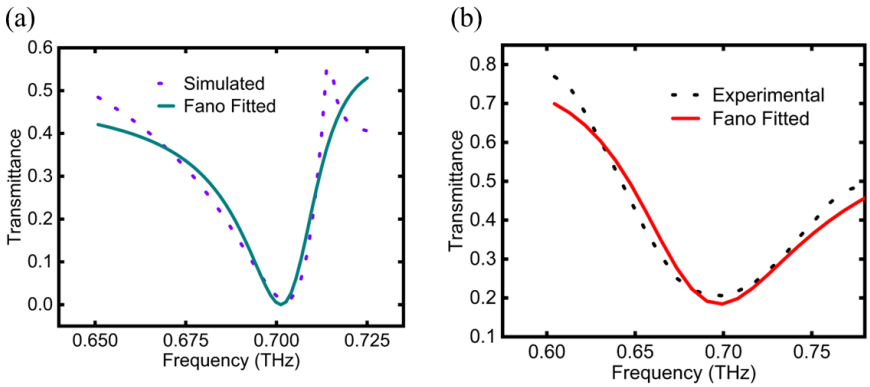

Figure A.2: The Fano fitting plot with the (a) simulated and (b) experimental transmittance spectrum, corresponding to the asymmetry of 29.4%.

$$Q = \frac{\omega_0}{2\gamma}$$

Figure S1 shows the fitted plot for the metasurface with $r_1 = 21\ \mu m$, $r_2 = 34\ \mu m$, $r_3 = 34\ \mu m$, and $r_4 = 47\ \mu m$. The extracted fitted parameters are: $\omega_0 = 0.68$ THz, $\gamma = 0.025$ THz, $a_1 = 0.2104$, $a_2 = 0.94$, and $b = 0.03$. The calculated Q factor for this resonance mode is found to be 13.6.

In the analysis of the resonance behavior of the metasurface, we observed some discrepancies between the simulated and experimental results. Figure S2(a) and S2(b) show the Fano fitting spectrum for the simulated and experimental data for the degree of asymmetry $\delta = 29.4\%$, respectively. The extracted fitted parameters are presented in Table S1. The experimentally calculated Q factor is found to be 5.96, whereas the simulated Q factor is 33.7. Despite the Q factor mismatch of the result, our work successfully demonstrates the theoretical approach to excite a quasi-BIC mode.

Table A.1: Extracted Fitting Parameters for Simulated and Experimental Data

Study Type	ω_0 (rad/s)	γ (rad/s)	a_1	a_2	b
Simulated	$2\pi \times 0.703 \times 10^{12}$	$2\pi \times 0.0104 \times 10^{12}$	0.36	0.76	-0.16
Experimental	$2\pi \times 0.68 \times 10^{12}$	$2\pi \times 0.057 \times 10^{12}$	-0.21	0.68	-0.05

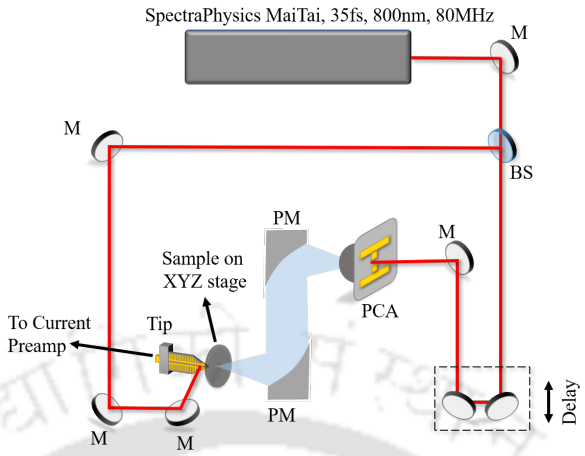

Figure A.3: Schematic representation of the nearfield scanning terahertz microscopy (NSTM) setup. It is composed of a beam splitter (BS) and mirrors (M) for splitting and guiding the beam for generation and detection of THz radiation, parabolic mirrors (PM) for focusing the THz beam, photoconductive antenna (PCA), and the THz microprobe for the generation and detection of THz pulses in the nearfield region.

A.2 Nearfield Scanning THz Microscopy (NSTM) setup

The working principle of the NSTM setup is analogous to that of a conventional THz time-domain spectroscopy (THz-TDS) system. A 35 fs optical pulse, centered at 800 nm, is generated using a Spectra-Physics MaiTai laser and split into two paths. One path is used to generate a single-cycle terahertz pulse via a photoconductive antenna (BATOP GmbH), while the other serves as a probe for detection. The generated terahertz beam is then focused onto the microprobe tip using off-axis parabolic mirrors.

For spatial mapping, the sample is mounted on an XYZ motorized stage, enabling precise scanning. The transient THz electric field distribution in the temporal domain is measured using a delay line. A polarization-sensitive micro-structured photoconductive antenna-based THz microprobe (Protemics GmbH) detects the near-field signal. The induced current in the microprobe, corresponding to the THz electric field, is amplified using a transimpedance amplifier and subsequently detected via a standard lock-in measurement technique (SR865).

A.3 Gallinet Martin's *ab initio* Fano theory

Galinet and Martin derived an analytical formula based on the interference of the bright and dark modes that overlap spectrally and spatially. Here, two pathways have been considered: direct excitation of the bright mode and the indirect excitation of the dark mode, which usually does not couple to the continuum. The Fano-like asymmetric lineshape and the bright mode's spectral profile can be calculated as:

$$I_d = \frac{(\Omega + q)^2 + b}{\Omega^2 + 1} \tag{S1}$$

where,

$$\Omega = \frac{\omega^2 - \omega_d^2}{2W_d\omega_d}$$

$$I_b = \frac{A^2}{\left(\frac{\omega^2-\omega_b^2}{2W_b\omega_b}\right)^2 + 1} \tag{S2}$$

The permittivity of metals includes an imaginary component that reflects intrinsic losses. In this scenario, the resonance frequency of the dark mode, represented as $\omega_d + i\gamma_d$, incorporates an imaginary part due to these losses. As a result of this, the phase difference between the direct and indirect interaction pathways does not result in totally destructive or constructive interference. The parameter b quantifies the impact of these intrinsic losses on the system. Additionally, the parameters q and b play crucial roles in determining the form of the asymmetric line shape function, influencing how the resonance features manifest in response spectra. If the asymmetric parameter $q = 0$, the resonance becomes symmetric with a minimum intensity. $I_d(\omega)_{\min} = b$. The analytically computed spectrum of the radiative mode (bright mode) is shown in Fig A.4(b), which approximately matches the spectral position of the broad dipole mode in the unperturbed case. The extracted fitting parameters are used to reconstruct the radiative mode spectrum. In Fig A.4(c), the asymmetric line shape function (discrete mode) is reconstructed using the fitting parameters. It should be noted that the asymmetric line shape function is recalculated using equation (S1) from the extracted parameters of the collective excitations of the two modes.

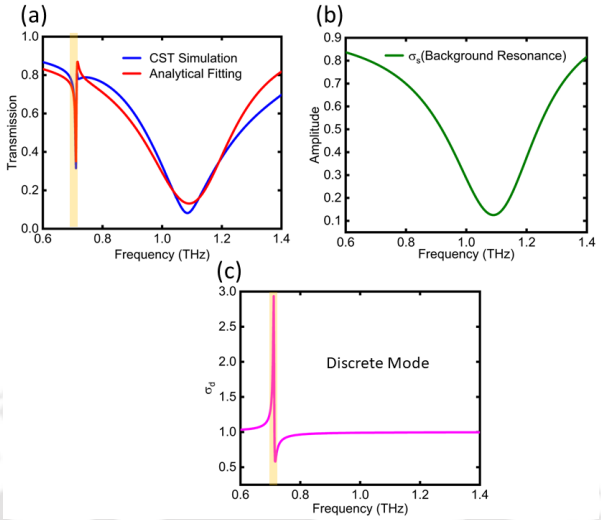

Figure A.4: (a) The analytical fitted spectrum for the collective effect of dark bright intereference (b) recalculated bright mode spectrum from the fitting parameters,(c) the decomposed asymmetric lineshape at the Fano frequency 0.713 THz.

Table A.2: Extracted fitting parameters for the radiative and discrete modes.

ω_d (THz)	W_d (THz)	ω_b (THz)	W_b (THz)	b	A	q
0.712	0.0018	1.09	0.18	1.68	0.93	-0.91

A.4 Structural details of the double split ring resonator design

In the perturbed case, the SRR resonators have been shifted from their respective unperturbed central position depending on the offset value D. Here, we have changed the interspacing separation between two SRRs, doubling the unit cell's lattice constant. The resonance mode shows almost constant frequency over the change of the interspacing distance. However, the linewidth of the resonance changes with the interspacing perturbation.

A.5 Brillouin zone folding

The calculated band diagram for the unit cell with lattice constant Λ (1×1) is shown in Fig. S3(a). We have used the CST eigenmode solver to model and simulate the dispersion plot. Fig. S3(b) shows the folding of the modes under the effect of lattice constant perturbation ($\Lambda_x = 2\Lambda, \Lambda_y = \Lambda$). The dashed line shows the folded modes. As a result of band folding,

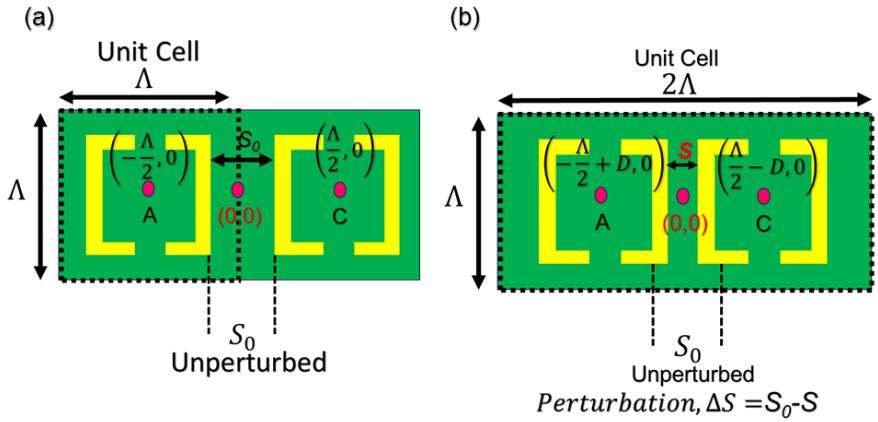

Figure A.5: Structural layout of the symmetric split ring resonator (SRR) metasurface. The image shows the arrangement of the SRR unit cell, illustrating the interspacing distance between adjacent SRRs, which is varied to induce the quasi-BIC mode. (a) the unperturbed case, (b) with interspacing perturbation, ΔS.

modes at the band edge become BIC at the Γ point (marked with a circle). The calculation of the near-field distribution of the z-component of the magnetic field at the Γ point corresponds to the mode closely resembling the H_z field distribution calculated using the frequency domain solver, as mentioned in the main manuscript. This observation validates our claim of the excitation of a quasi-BIC mode under the perturbation of the lattice constant.

A.6 Toroidal nature of the excited quasi BIC mode in the DSRR

To examine the nature of the sharp quasi-BIC mode, we have simulated the surface current profile at the resonance frequency 0.71 THz, as shown in FigA7 (a). The clockwise flow of current on the left SRR leads to a magnetic moment going inside the plane on the left side (indicated by the cross symbol), while the anticlockwise flow on the right SRR leads to a magnetic moment coming outside the plane on the right side of the resonator (indicated by the dot symbol). This end-to-end formation of magnetic moments leads to the excitation of a toroidal dipole moment along the y direction. Thus, there is a clear excitation of toroidal dipole moment in the metasurface at the resonant frequency of 0.71 THz. Fig S7 (b) depicts an artistic representation of the formation of the toroidal dipole due to the formation of the circulating magnetic field formed by the closed current

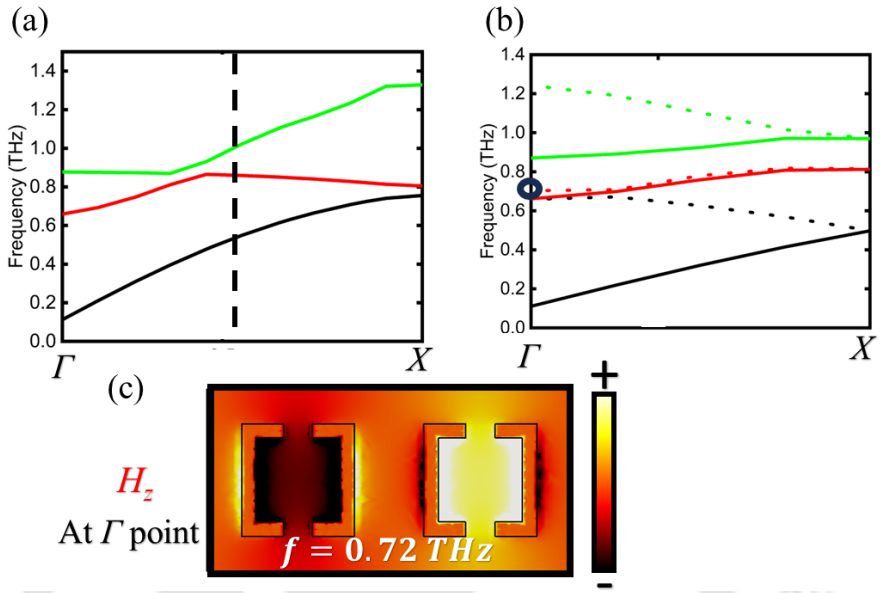

Figure A.6: (a) The dispersion plot for the unperturbed case, when the unit cell consists of a single unit cell, the dotted line shows the position of new X point that would be as a result of folding, (b) the folded modes under the effect of lattice constant perturbation, the folded modes are shown with dotted lines. The circular mark indicates the mode that becomes a BIC mode under the perturbation effect. (c) The Z component of the folded BIC mode calculated using the eigen mode solver.

carrying loop. The confined loops of oscillating magnetic fields that curl around the fictitious direction of the toroidal dipole vector show a hallmark of the presence of toroidal dipole mode.

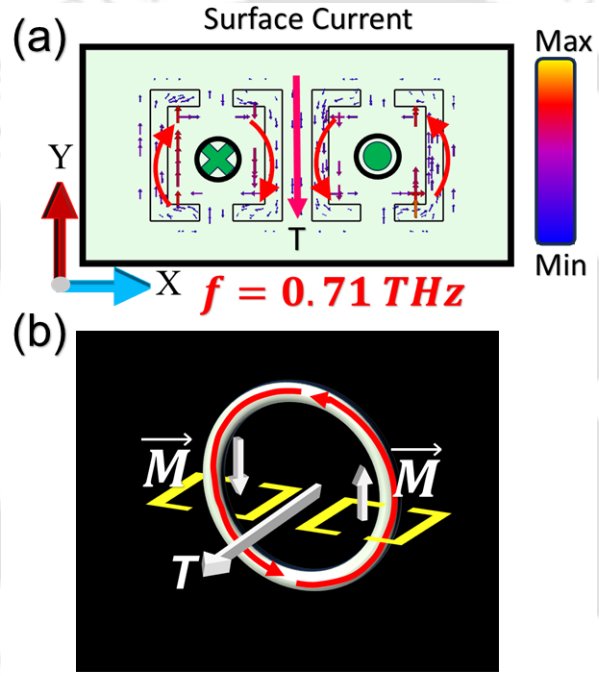

Figure A.7: (a) The simulated surface current profile at the sharp quasi-BIC resonance mode, (b) a pictorial representation of the formation of the toroidal moment because of the head-to-tail magnetic moment.

BIBLIOGRAPHY

[1] C. W. Hsu, B. Zhen, A. D. Stone, J. D. Joannopoulos, M. Soljačić: Bound States in the Continuum. *Nat. Rev. Mater.* 1, 1–13 (2016).

[2] K. L. Koshelev, Z. F. Sadrieva, A. A. Shcherbakov, Y. S. Kivshar, A. A. Bogdanov: Bound States in the Continuum in Photonic Structures. *Phys.-Usp* 93, 528–553 (2023).

[3] Gentry, Cale M., and Miloš A. Popović. "Dark state lasers." *Optics Letters* 39, no. 14 (2014): 4136-4139. Optica Publishing Group.

[4] Koshelev, Kirill, et al. "Asymmetric metasurfaces with high-Q resonances governed by bound states in the continuum." *Physical Review Letters* 121, no. 19 (2018): 193903.

[5] K. Koshelev, G. Favraud, A. Bogdanov, Y. Kivshar, A. Fratalocchi: Nonradiating Photonics with Resonant Dielectric Nanostructures. *Nanophotonics* 8, 725–745 (2019).

[6] Von Neumann, J., and E. Wigner. "On some peculiar discrete eigenvalues." *Phys. Z* 30 (1929): 465-467.

[7] Friedrich, H., and D. Wintgen. "Interfering resonances and bound states in the continuum." *Physical Review A*, 32.6 (1985): 3231.

[8] Scully, Marlan O., and M. Suhail Zubairy. *Quantum Optics*. Cambridge University Press, 1997.

[9] Kodigala, Ashok, et al. "Lasing action from photonic bound states in continuum." *Nature*, vol. 541, no. 7636, 2017, pp. 196-199.

[10] Hsu, Chia Wei, et al. "Observation of trapped light within the radiation continuum." *Nature*, 499.7457 (2013): 188-191.

[11] Hsu, Chia Wei, et al. "Bloch surface eigenstates within the radiation continuum." *Light: Science & Applications*, vol. 2.

[12] Muljarov, Egor A., and Wolfgang Langbein. "Exact mode volume and Purcell factor of open optical systems." *Physical Review B*, vol. 94, no. 23, 2016, pp. 235438.

[13] Chebykin, A. V., et al. "Enhancement of the Purcell factor in multiperiodic hyperboliclike metamaterials." *Physical Review A*, vol. 93, no. 3, 2016, pp. 033855.

[14] Bahk, Y.-M., Park, D. J., and Kim, D.-S. "Terahertz field confinement and enhancement in various sub-wavelength structures." *Journal of Applied Physics* 126.12 (2019): 124501.

[15] Karmakar, S., Banerjee, S., Kumar, D., Kamble, G., Varshney, R. K., and Roy Chowdhury, D. "Deep-Subwavelength coupling-induced Fano resonances in symmetric terahertz metamaterials." *physica status solidi (RRL)–Rapid Research Letters* 13

[16] Gupta, M., and Singh, R. "Terahertz sensing with optimized Q/V_{eff} metasurface cavities." *Advanced Optical Materials* 8.16 (2020): 1902025.

[17] Cai, W., Shalaev, V., and Paul, D. "Optical Metamaterials: Fundamentals and Applications." *Physics Today* 63 (2010): doi:10.1063/1.3490504.

[18] Veselago, V. G. "The electrodynamics of substances with simultaneously negative values of ϵ and μ." *Soviet Physics Uspekhi*, vol. 10, no. 4 (1968): 509–514.

[19] Smith, D. R., Padilla, W. J., Vier, D. C., Nemat-Nasser, S. C., and Schultz, S. "Composite Medium with Simultaneously Negative Permeability and Permittivity." *Physical Review Letters*, 84.18 (2000): 4184-4187.

[20] Padilla, W. J., Basov, D. N., and Smith, D. R. "Negative refractive index metamaterials." *Materials Today*, 9.7-8 (2006): 28-35.

[21] Kruk, S., and Kivshar, Y. "Functional meta-optics and nanophotonics governed by Mie resonances." *ACS Photonics*, 4.11 (2017): 2638–2649.

[22] Karepov, S., and Ellenbogen, T. "Metasurface-based contact lenses for color vision deficiency." *Optics Letters*, 45.2020 (2020): 1379–1382.

[23] Huang, L., Zhang, S., and Zentgraf, T. "Metasurface holography: from fundamentals to applications." *Nanophotonics*, 7.6 (2018): 1169–1190. DOI: 10.1515/nanoph-2017-0118.

[24] Zhang, X., Deng, R., Yang, F., Jiang, C., Xu, S., and Li, M. "Metasurface-based ultrathin beam splitter with variable split angle and power distribution." *ACS Photonics*, 5.8 (2018): 2997–3002. DOI: 10.1021/acsphotonics.8b00626.

[25] Zhang, X.-C., Xu, J., et al. *Introduction to THz Wave Photonics*. Vol. 29, Springer, 2010.

[26] Lee, Y.-S. *Principles of Terahertz Science and Technology*. Vol. 170, Springer Science & Business Media, 2009.

[27] Tonouchi, M. "Cutting-edge terahertz technology." *Nature Photonics*, vol. 1, no. 2 (2007): 97–105.

[28] Tonouchi, M. "Prospect of terahertz technology." In *Proceedings of the 2007 19th International Conference on Applied Electromagnetics and Communications*, IEEE, 2007, pp. 1–4.

[29] Li, S., Zhou, C., Liu, T., and Xiao, S. "Symmetry-protected bound states in the continuum supported by all-dielectric metasurfaces." *Physical Review A*, vol. 100, no. 6 (2019): 063803.

[30] Bogdanov, A. A., Koshelev, K. L., Kapitanova, P. V., Rybin, M. V., Gladyshev, S. A., Sadrieva, Z. F., Samusev, K. B., Kivshar, Y. S., and Limonov, M. F. "Bound states in the continuum and Fano resonances in the strong mode coupling regime." *Advanced Photonics*, vol. 1, no. 1 (2019): 016001.

[31] Cong, L., and Singh, R. "Symmetry-protected dual bound states in the continuum in metamaterials." *Advanced Optical Materials*, vol. 7, no. 13 (2019): 1900383.

[32] Tan, T. C. W., Plum, E., and Singh, R. "Lattice-enhanced Fano resonances from bound states in the continuum metasurfaces." *Advanced Optical Materials*, vol. 8, no. 6 (2020): 1901572.

[33] Fano, U. "Effects of configuration interaction on intensities and phase shifts." *Physical Review*, vol. 124, no. 6 (1961): 1866.

[34] Lim, W. X., and Singh, R. "Universal behaviour of high-Q Fano resonances in metamaterials: terahertz to near-infrared regime." *Nano Convergence*, vol. 5 (2018): 1–7.

[35] Miroshnichenko, A. E., Flach, S., and Kivshar, Y. S. "Fano resonances in nanoscale structures." *Reviews of Modern Physics*, vol. 82, no. 3 (2010): 2257–2298.

[36] Singh, R., Cao, W., Al-Naib, I., Cong, L., Withayachumnankul, W., and Zhang, W. "Ultrasensitive terahertz sensing with high-Q Fano resonances in metasurfaces." *Applied Physics Letters*, vol. 105, no. 17 (2014).

[37] Zheng, Z., Komar, A., Zangeneh Kamali, K., Noble, J., Whichello, L., Miroshnichenko, A. E., Rahmani, M., Neshev, D. N., and Xu, L. "Planar narrow bandpass filter based on Si resonant metasurface." *Journal of Applied Physics*, vol. 130, no. 5 (2021).

[38] Zhou, C., Qu, X., Xiao, S., and Fan, M. "Imaging through a Fano-resonant dielectric metasurface governed by quasi-bound states in the continuum." *Physical Review Applied*, vol. 14, no. 4 (2020): 044009.

[39] Schwarz, B. "Mapping the world in 3D." *Nature Photonics*, vol. 4, no. 7 (2010): 429–430.

[40] Jansen, C., Al-Naib, I. A. I., Born, N., and Koch, M. "Terahertz metasurfaces with high Q-factors." *Applied Physics Letters*, vol. 98, no. 5 (2011).

[41] Chen, T., Zhang, D., Huang, F., Li, Z., and Hu, F. "Design of a terahertz metamaterial sensor based on split ring resonator nested square ring resonator." *Materials Research Express*, vol. 7, no. 9 (2020): 095802.

[42] Xu, N., Singh, R., and Zhang, W. "High-Q lattice mode matched structural resonances in terahertz metasurfaces." *Applied Physics Letters*, vol. 109, no. 2 (2016).

[43] Wang, W., Srivastava, Y. K., Tan, T. C., Wang, Z., and Singh, R. "Brillouin zone folding driven bound states in the continuum." *Nature Communications*, vol. 14, no. 1 (2023): 2811.

[44] Taflove, A., and Brodwin, M. E. "Numerical solution of steady-state electromagnetic scattering problems using the time-dependent Maxwell's equations." *IEEE Transactions on Microwave Theory and Techniques*, vol. 23, pp. 623–630, Aug. 1975.

[45] Lee, Y.-S. *Principles of Terahertz Science and Technology*. Springer Science & Business Media, vol. 170, 2009.

[46] Rodriguez, G., and Taylor, A. J. "Screening of the bias field in terahertz generation from photoconductors." *Optics Letters*, vol. 21, no. 14, pp. 1046–1048, 1996.

[47] Singh, A., Pal, S., Surdi, H., Prabhu, S. S., Nanal, V., and Pillay, R. G. "Highly efficient and electrically robust carbon irradiated semi-insulating GaAs based photoconductive terahertz emitters." *Applied Physics Letters*, vol. 104, no. 6, 2014.

[48] Neu, J., and Schmuttenmaer, C. A. "Tutorial: An introduction to terahertz time domain spectroscopy (THz-TDS)." *Journal of Applied Physics*, vol. 124, no. 23, 2018.

[49] Jang, W.-Y., Ku, Z., Jeon, J., Kim, J. O., Lee, S. J., Park, J., Noyola, M. J., and Urbas, A. "Experimental demonstration of adaptive infrared multispectral imaging using plasmonic filter array." *Scientific Reports*, vol. 6, no. 1, p. 34876, 2016.

[50] Hsu, C. W., Zhen, B., Qiu, W., Shapira, O., DeLacy, B. G., Joannopoulos, J. D., and Soljačić, M. "Transparent displays enabled by resonant nanoparticle scattering." *Nature Communications*, vol. 5, no. 1, p. 3152, 2014.

[51] Yang, L., Yu, S., Li, H., and Zhao, T. "Multiple Fano resonances excitation on all-dielectric nanohole arrays metasurfaces." *Optics Express*, vol. 29, pp. 14905–14916, 2021.

[52] Fu, T., Liu, F., An, Y., Li, Q., Xiao, G.-L., Sun, T.-Y., and Li, H.-O. "Narrow-band asymmetric transmission based on the dark mode of Fano resonance on symmetric trimeric metasurfaces." *Optics Express*, vol. 28, pp. 30141–30149, 2020.

[53] Badri, S. H., Gilarlue, M. M., SaeidNahaei, S., and Kim, J. S. "High-Q Fano resonance in all-dielectric metasurfaces for molecular fingerprint detection." *Journal of the Optical Society of America B*, vol. 39, pp. 563–569, 2022.

[54] Zhen, B., Hsu, C. W., Lu, L., Stone, A. D., and Soljačić, M. "Topological nature of optical bound states in the continuum." *Physical Review Letters*, vol. 113, p. 257401, 2014.

[55] Fang, C., Yang, Q., Yuan, Q., Gan, X., Zhao, J., Shao, Y., Liu, Y., Han, G., and Hao, Y. "High-Q resonances governed by the quasi-bound states in the continuum in all-dielectric metasurfaces." *Opto-Electronic Advances*, vol. 4, p. 200030, 2021.

[56] Li, S., Zhou, C., Liu, T., and Xiao, S. "Symmetry-protected bound states in the continuum supported by all-dielectric metasurfaces." *Physical Review A*, vol. 100, p. 063803, 2019.

[57] Alaee, R., Rockstuhl, C., and Fernandez-Corbaton, I. "An electromagnetic multipole expansion beyond the long-wavelength approximation." *Optics Communications*, vol. 407, pp. 17–21, 2018.

[58] Hinamoto, T., and Fujii, M. "MENP: an open-source MATLAB implementation of multipole expansion for nanophotonics." *OSA Continuum*, vol. 4, pp. 1640–1648, 2021.

[59] Algorri, J., Zografopoulos, D., Ferraro, A., García-Cámara, B., Beccherelli, R., and Sánchez-Pena, J. "Ultrahigh-quality factor resonant dielectric metasurfaces based on hollow nanocuboids." *Optics Express*, vol. 27, pp. 6320–6330, 2019.

[60] Jeong, J., Goldflam, M. D., Campione, S., Briscoe, J. L., Vabishchevich, P. P., Nogan, J., Sinclair, M. B., Luk, T. S., and Brener, I. "High quality factor toroidal resonances in dielectric metasurfaces." *ACS Photonics*, vol. 7, pp. 1699–1707, 2020.

[61] Guo, L., Zhang, Z., Xie, Q., Li, W., Xia, F., Wang, M., Feng, H., You, C., and Yun, M. "Toroidal dipole bound states in the continuum in all-dielectric metasurface for high-performance refractive index and temperature sensing." *Applied Surface Science*, vol. 615, p. 156408, 2023.

[62] Gupta, M., Savinov, V., Xu, N., Cong, L., Dayal, G., Wang, S., Zhang, W., Zheludev, N. I., and Singh, R. "Sharp toroidal resonances in planar terahertz metasurfaces." *Advanced Materials*, vol. 28, no. 37, pp. 8206–8211, 2016.

[63] Bhattacharya, A., Devi, K. M., Nguyen, T., and Kumar, G. "Actively tunable toroidal excitations in graphene based terahertz metamaterials." *Optics Communications*, vol. 459, p. 124919, 2020.

[64] Nanz, S. *Toroidal Multipole Moments in Classical Electrodynamics: An Analysis of their Emergence and Physical Significance*; Springer Fachmedien Wiesbaden: Wiesbaden, 2016, p 5.

[65] Islam, M., Rao, S.J.M., Kumar, G., Pal, B.P., and Roy Chowdhury, D. "Role of resonance modes on terahertz metamaterials based thin film sensors." *Scientific Reports* 7, no. 1 (2017): 7355. Nature Publishing Group.

[66] Liang, C., Niu, G., Chen, X., Zhou, Z., Yi, Z., Ye, X., Duan, T., Yi, Y., and Xiao, S. "Tunable triple-band graphene refractive index sensor with good angle-polarization tolerance." *Optics Communications* 436 (2019): 57–62. Elsevier.

[67] Yu, S., Li, H., Wang, Y., Gao, Z., Zhao, T., and Yu, J. "Multiple Fano resonance excitation of all-dielectric nanoholes cuboid arrays in the near infrared region." *Results in Physics* 28 (2021): 104569. Elsevier.

[68] Liu, G.-D., Zhai, X., Wang, L.-L., Lin, Q., Xia, S.-X., Luo, X., and Zhao, C.-J. "A high-performance refractive index sensor based on Fano resonance in Si split-ring metasurface." *Plasmonics* 13 (2018): 15–19. Springer.

[69] Li, H., Yu, S., Yang, L., and Zhao, T. "High Q-factor multi-Fano resonances in all-dielectric double square hollow metamaterials." *Optics & Laser Technology* 140 (2021): 107072. Elsevier.

[70] Long, X., Zhang, M., Xie, Z., Tang, M., and Li, L. "Sharp Fano resonance induced by all-dielectric asymmetric metasurface." *Optics Communications* 459 (2020): 124942. Elsevier.

[71] Yang, Y., Kravchenko, I.I., Briggs, D.P., and Valentine, J. "All-dielectric metasurface analogue of electromagnetically induced transparency." *Nature Communications* 5, no. 1 (2014): 5753. Nature Publishing Group.

[72] Li, S., Zhou, C., Liu, T., and Xiao, S. "Symmetry-protected bound states in the continuum supported by all-dielectric metasurfaces." *Physical Review A* 100, no. 6 (2019): 063803. American Physical Society.

[73] Hu, J., Lang, T., and Shi, G.-h. "Simultaneous measurement of refractive index and temperature based on all-dielectric metasurface." *Optics Express* 25, no. 13 (2017): 15241–15251. Optica Publishing Group.

[74] Guo, L., Zhang, Z., Xie, Q., Li, W., Xia, F., Wang, M., Feng, H., You, C., and Yun, M. "Toroidal dipole bound states in the continuum in all-dielectric metasurface for high-performance refractive index and temperature sensing." *Applied Surface Science* 615 (2023): 156408. Elsevier.

[75] Yao, Q., Meng, H., Wang, W., Xue, H., Xiong, R., Huang, B., Tan, C., and Huang, X. "Simultaneous measurement of refractive index and temperature based on a core-offset Mach–Zehnder interferometer combined with a fiber Bragg grating." *Sensors and Actuators A* 209 (2014): 73–77. Elsevier.

[76] Liu, P., and Shi, Y. "Simultaneous measurement of refractive index and temperature using cascaded side-coupled photonic crystal nanobeam cavities." *Optics Express* 25, no. 23 (2017): 28398–28406. Optica Publishing Group.

[77] Nemova, G., and Kashyap, R. "Silica bottle resonator sensor for refractive index and temperature measurements." *Sensors* 16, no. 1 (2016): 87. MDPI.

[78] Limonov, M.F., Rybin, M.V., Poddubny, A.N., and Kivshar, Y.S. "Fano resonances in photonics." *Nature Photonics* 11, no. 9 (2017): 543–554. Nature Publishing Group.

[79] Li, H., Xing, J., Shi, Y., Yu, S., and Zhao, T. "Performance analysis and optimization of high Q-factor toroidal resonance refractive index sensor based on all-dielectric metasurface." *Optics & Laser Technology* 157 (2023): 108752. Elsevier.

[80] Gambino, F., Giaquinto, M., Ricciardi, A., and Cusano, A. "A review on dielectric resonant gratings: Mitigation of finite size and Gaussian beam size effects." *Results in Optics* 6 (2022): 100210. Elsevier.

[81] Bhowmik, T., and Sikdar, D. "Electrically tunable metasurface for dual-band spatial light modulation using the epsilon-near-zero effect." *Optics Letters* 47, no. 19 (2022): 4993–4996. Optica Publishing Group.

[82] Liu, Z., Xu, Y., Lin, Y., Xiang, J., Feng, T., Cao, Q., Li, J., Lan, S., and Liu, J. "High-Q quasibound states in the continuum for nonlinear metasurfaces." *Physical Review Letters* 123, no. 25 (2019): 253901. American Physical Society.

[83] Karmakar, S., Varshney, R.K., and Roy Chowdhury, D. "Theoretical investigation of active modulation and enhancement of Fano resonance in THz metamaterials." *OSA Continuum* 2, no. 3 (2019): 531–539. Optica Publishing Group.

[84] Wang, P., Gong, Z., Ye, K., Kumar, V., Zhu, K., Sha, L., Yan, J., Yin, J., Cheng, K., Wang, G., et al. "Wang et al." *Carbon Energy* 2, no. 4 (2020): 635–645. Wiley.

[85] Myers, T.L., Tonkyn, R.G., Danby, T.O., Taubman, M.S., Bernacki, B.E., Birnbaum, J.C., Sharpe, S.W., and Johnson, T.J. "Accurate measurement of the optical constants n and k for a series of 57 inorganic and organic liquids for optical modeling and detection." *Applied Spectroscopy* 72, no. 4 (2018): 535–550. Society for Applied Spectroscopy.

[86] Myers, T.L., Tonkyn, R.G., Danby, T.O., Taubman, M.S., Bernacki, B.E., Birnbaum, J.C., Sharpe, S.W., and Johnson, T.J. "Accurate measurement of the optical constants n and k for a series of 57 inorganic and organic liquids for optical modeling and detection." *Applied Spectroscopy* 72, no. 4 (2018): 535–550. Society for Applied Spectroscopy.

[87] Ali, S.M.U., Nur, O., Willander, M., and Danielsson, B. "A fast and sensitive potentiometric glucose microsensor based on glucose oxidase coated ZnO nanowires grown on a thin silver wire." *Sensors and Actuators B: Chemical* 145, no. 2 (2010): 869–874. Elsevier.

[88] Zakaria, R., Zainuddin, N.A.M., Raya, S.A., Alwi, S.A.K., Anwar, T., Sarlan, A., Ahmed, K., and Amiri, I.S. "Sensitivity comparison of refractive index transducer optical fiber based on surface plasmon resonance using Ag, Cu, and bimetallic Ag–Cu layer." *Micromachines* 11, no. 1 (2020): 77. MDPI.

[89] Shalabney, A., and Abdulhalim, I. "Figure-of-merit enhancement of surface plasmon resonance sensors in the spectral interrogation." *Optics Letters* 37 (2012): 1175–1177. Optica Publishing Group.

[90] Yuan, L., Qiu, C., Liao, Z., Gong, M., Long, Y., Yang, R., and Zhang, Z. "Nanoscale refractive index sensor with ultrahigh figure of merit based on toroidal dielectric metasurfaces." *Optics Communications* 528 (2023): 128988. Elsevier.

[91] Huang, L., Li, H., Yu, S., and Zhao, T. "Analogue of electromagnetically induced transparency inspired by bound states in the continuum and toroidal dipolar response in all-dielectric metasurfaces." *Photonics and Nanostructures: Fundamentals and Applications* 51 (2022): 101041. Elsevier.

[92] Zhou, Y., Guo, Z., Zhao, X., Wang, F., Yu, Z., Chen, Y., Liu, Z., Zhang, S., Sun, S., and Wu, X. "Dual-quasi bound states in the continuum enabled plasmonic metasurfaces." *Advanced Optical Materials* 10, no. 19 (2022): 2200965. Wiley.

[93] Shen, Z., and Du, M. "High-performance refractive index sensing system based on multiple Fano resonances in polarization-insensitive metasurface with nanorings." *Optics Express* 29, no. 18 (2021): 28287–28296. Optica Publishing Group.

[94] Fabitha, K., and Rao, R. "Biocompatible miniature temperature sensor based on whispering gallery modes of Sm^{3+} activated ZnO optical micro-resonators." *Applied Physics Letters* 118, no. 16 (2021): 161901. AIP Publishing.

[95] Della Corte, F.G., Cocorullo, G., Iodice, M., and Rendina, I. "Temperature dependence of the thermo-optic coefficient of InP, GaAs, and SiC from room temperature to 600 K at the wavelength of 1.5 μm." *Applied Physics Letters* 77, no. 11 (2000): 1614–1616. AIP Publishing.

[96] Zhao, Q., Behunin, R.O., Rakich, P.T., Chauhan, N., Isichenko, A., Wang, J., Hoyt, C., Fertig, C., Blumenthal, D.J., et al. "Low-loss low thermo-optic coefficient Ta_2O_5 on crystal quartz planar optical waveguides." *APL Photonics* 5, no. 11 (2020): 116101. AIP Publishing.

[97] Cong, L., Manjappa, M., Xu, N., Al-Naib, I., Zhang, W., and Singh, R. "Fano resonances in terahertz metasurfaces: a figure of merit optimization." *Advanced Optical Materials* 3, no. 12 (2015): 1537–1543. Wiley.

[98] Jansen, C., Al-Naib, I.A.I., Born, N., and Koch, M. "Terahertz metasurfaces with high Q-factors." *Applied Physics Letters* 98, no. 5 (2011): 051109. AIP Publishing.

[99] Chen, T., Zhang, D., Huang, F., Li, Z., and Hu, F. "Design of a terahertz metamaterial sensor based on split ring resonator nested square ring resonator." *Materials Research Express* 7, no. 9 (2020): 095802. IOP Publishing.

[100] Zhang, X., Shi, W., Gu, J., Cong, L., Chen, X., Wang, K., Xu, Q., Han, J., and Zhang, W. "Terahertz metasurface with multiple BICs/QBICs based on a split ring resonator." *Optics Express* 30, no. 18 (2022): 29088–29098. Optica Publishing Group.

[101] Aizpurua, J., Hanarp, P., Sutherland, D.S., Käll, M., Bryant, G.W., and García de Abajo, F.J. "Optical properties of gold nanorings." *Physical Review Letters* 90, no. 5 (2003): 057401. APS.

[102] Feng, G., Chen, Z., Liu, X., Wang, X., Liu, X., Sun, F., Yang, Y., Wang, Y., and Chen, S. "Fano resonance with high Q and figure of merit in terahertz band based on structural perturbation." *Journal of Applied Physics* 132, no. 23 (2022): 235101. AIP Publishing.

[103] Dana, B.D., Koya, A.N., Song, X., and Lin, J. "Enhanced Fano resonance in asymmetric nano dimer for sensing applications." *Physica B: Condensed Matter* 631 (2022): 413706. Elsevier.

[104] Basyooni, M.A., Ahmed, A.M., and Shaban, M. "Plasmonic hybridization between two metallic nanorods." *Optik* 172 (2018): 1069–1078. Elsevier.

[105] Yin, L.-Y., Wang, S.-B., Liang, X., Li, Z.-Y., and Wang, J.-F. "Double Fano resonances in nanoring cavity dimers: the effect of plasmon hybridization between dark subradiant modes." *AIP Advances* 4, no. 7 (2014): 077101. AIP Publishing.

[106] Liu, N., Kaiser, S., and Giessen, H. "Magnetoinductive and electroinductive coupling in plasmonic metamaterial molecules." *Advanced Materials* 20, no. 23 (2008): 4521–4525. Wiley.

[107] Mallick, S., Singh, R., Srivastava, Y.K., Manjappa, M., Bettiol, A.A., and Singh, N. "Accessing dual toroidal modes in terahertz plasmonic metasurfaces through polarization-sensitive resonance hybridization." *New Journal of Physics* 25, no. 5 (2023): 053016. IOP Publishing.

[108] Hsieh, L.-H. "Analysis, modeling and simulation of ring resonators and their applications to filters and oscillators." PhD diss., Texas A&M University, 2004.

[109] Gallinet, B., and Martin, O.J.F. "Influence of electromagnetic interactions on the line shape of plasmonic Fano resonances." *ACS Nano* 5, no. 11 (2011): 8999–9008. ACS Publications.

[110] Wang, X., Liu, Z., Chen, X., Huang, J., and Zhang, Y. "Fano resonance and sensing application based on terahertz asymmetric split-ring metasurfaces." *Journal of Alloys and Compounds* 976 (2024): 173130. Elsevier.

[111] N. Xu, R. Singh, W. Zhang: High-Q lattice mode matched structural resonances in terahertz metasurfaces. *Appl. Phys. Lett.* 109, (2016).

[112] V. A. Fedotov, M. Rose, S. L. Prosvirnin, N. Papasimakis, N. I. Zheludev: Sharp Trapped-Mode Resonances in Planar Metamaterials with a Broken Structural Symmetry. *Phys. Rev. Lett.* 99, 147401 (2007).

[113] R. Singh, I. A. I. Al-Naib, M. Koch, W. Zhang: Sharp Fano resonances in THz metamaterials. *Opt. Express* 19, 6312–6319 (2011).

[114] N. Xu, R. Singh, W. Zhang: High-Q lattice mode matched structural resonances in terahertz metasurfaces. *Appl. Phys. Lett.* 109, (2016).

[115] R. Singh, C. Rockstuhl, F. Lederer, W. Zhang: The impact of nearest neighbor interaction on the resonances in terahertz metamaterials. *Appl. Phys. Lett.* 94, (2009).

[116] T. C. Tan, E. Plum, R. Singh: Lattice-enhanced Fano resonances from bound states in the continuum metasurfaces. *Adv. Opt. Mater.* 8, 1901572 (2020).

[117] I. Al-Naib, R. Singh, C. Rockstuhl, F. Lederer, S. Delprat, D. Rocheleau, M. Chaker, T. Ozaki, R. Morandotti: Excitation of a high-Q subradiant resonance mode in mirrored single-gap asymmetric split ring resonator terahertz metamaterials. *Appl. Phys. Lett.* 101, (2012).